Neutron detectors based on boron nitride and its alloys

Adama Mballo

THÈSE

pour l'obtention du titre de

Docteur de l'Université de Lorraine

présenté par:

Adama MBALLO

préparée au sein du :

Laboratoire International de Recherche Georgia Tech-CNRS IRL 2958

Georgia Tech Lorraine et CNRS

Ecole Doctorale: Chimie-Mécanique-Matériaux-Physique

DÉTECTEURS DE NEUTRONS À BASE DE NITRURE DE BORE ET SES ALLIAGES

Thèse soutenue publiquement à Metz

devant le jury composé de:

Mme. Eva Monroy	Chercheur CEA INAC/SP2M, Grenoble	Rapporteur
M. Abdel Hadi Kassiba	Professeur Université du Maines, Le Mans	Rapporteur
M. Xiaohang Li	Professeur associé King Abdullah University	Examinateur
Mme. Ekaterina Chikoidze	Ingénieure de recherche GEMaC	Examinateur
M. Jean-Paul Salvestrini	Professeur Georgia Tech Lorraine	Examinateur
M. Suresh Sundaram	Professeur Georgia Tech Lorraine	Co-encadrant
M. Abdallah Ougazzaden	Professeur Georgia Institute of Technology	Directeur de thèse

DECEMBRE 2021

TABLE OF CONTENTS

LIST OF TABLES

LIST OF FIGURES

ACKNOWLEDGMENT

I would like to thank my advisors, Professor Abdallah Ougazzaden and Dr. Suresh Sundaram. Without their valuable advice, knowledge, expertise and guidance, this work would not have been possible. I am thankful for the opportunity of working under them, utilizing all the various facilities at the International Research Lab Georgia Tech-CNRS (IRL 2958). I am blessed to be a part of the epi-team over the past four years. Thanks goes out to the other members of my PhD committee: Dr Jean Paul Salvestrini, Dr. Eva Monroy, Dr. Abdel Hadi Kassiba, Dr. Ekaterina Chikoidze and Dr Xiaohang Li. The patience and the support of Dr. Jean Paul Salvestrini, Dr. Ali Ahaitouf and Dr. Paul Voss has been unwavering during the completion of this thesis. I would also like to thank the institutions and funding partners that made this work possible. Generous grants from the French National Research Agency (ANR) under the GANEX Laboratory of Excellence (Grant number ANR-11-LABX-0014) have helped make this work possible. Much of the work has been carried out using the equipment, personnel, and resources of the Georgia Tech-CNRS, IRL 2958.

I would like to extend my gratitude personally to the other PhD students and colleagues who have assisted in various ways in the making of this thesis. To Phuong Vuong, and Vishnu Ottapilakka, who assisted with MOVPE growth. To Soufiane Karrakchou, Yves Sama and Taha Ayari who assisted in device fabrication. To Yacine Halfaya who have trained me on the characterization tools.

Finally, I would like to thank my mom, dad and siblings for being with me at every stage of my life. My dad has always been a support in my study. Special thanks to my wife for the strong support during my PhD. My sweet love goes to my sons: Djibril, Muhammad, and Ibrahim.

GENERAL INTRODUCTION

Neutron detectors play a crucial role in various applications such as homeland security (airports, borders and ports) to control illegal activities involving nuclear materials, nuclear power plants for neutron radiation safety and monitoring, high energy physics and nuclear science. In addition, recent events such as the Fukushima explosion and the polonium poisoning have stimulated interest in the development of small, portable and low-cost solid-state neutron detectors (SSND). To achieve high efficiency in SSND factors such as neutron absorption and charge collection are critical.

The general objective of this work is to develop efficient solid-state thermal neutron detectors based on boron containing III-nitride materials such as boron nitride (BN) and boron-gallium nitride (BGaN). Boron in these materials is very important for the detection of thermal neutrons due to the high neutron capture cross section of the isotope boron-10 (3840 barns) and its low sensitivity to gamma radiation. However, the main challenge with boron containing III-N for neutron detection is the quality of the materials. For instance, growth of thick, high quality single crystalline boron-rich BGaN needed for neutron detectors is difficult due to strain-induced degradations such as phase separation and columnar 3D growth. Therefore, we developed an innovative approach consisting of BGaN/GaN superlattices (SLs) with a nominal boron content of 3% in the BGaN layer. These BGaN/GaN SLs materials were used to fabricate metal-semiconductor-metal (MSM) and p-i-n heterojunction devices, which showed significant neutron-induced signal. Even with this approach, it is found that there are several constraints on the boron content, the quality of the material, and the overall thickness, which are key factors for the realization of high-efficiency neutron detectors.

By using binary BN (100% boron) epitaxial layers, higher thermal neutron absorption and performance of neutron detectors are expected. Our group has reported for the first time large area 2D layered h-BN films with high crystalline quality on sapphire substrate by metal organic vapor phase epitaxy (MOVPE). These BN films were used to demonstrate high efficiency deep UV photodetectors. In this work, we have grown up to 2.5µm thick natural and ^{10}B enriched BN samples and used them to fabricate MSM based detectors. The advantages of MSM structures are the ability to achieve self-powered operation, similar to that demonstrated for UV photodetectors, and to benefit from internal gain in order to increase the neutron signal.

This work also aims to investigate the control of the electrical conductivity of h-BN by in-situ Mg doping for the future realization of p-n based BN neutron detectors. Since a high boron content is highly desirable for neutron detectors, we have further explored experimentally for the first time a new material: boron-rich BAlN alloys.

The manuscript is composed of 7 chapters:

Chapter 1 introduces neutron detectors, including the state of the art and the problems associated with the different technologies (gas-filled detectors, scintillator-based and semiconductor-based neutron detectors).

Chapter 2 presents the basic properties of III-nitride material. A brief introduction to the techniques and equipment used for growth and characterization is also included. **Chapter 3** is devoted to MOVPE growth studies of BGaN/GaN SLs and BN. Firstly, the growth results of BGaN/GaN superlattice structures with long period (consisting of 20 nm thick BGaN and 20 nm thick GaN repeated 11 times) are reported. Then, the growth of 2.5 µm thick BN and

^{10}B-enriched BN on sapphire is performed. The structural and morphological properties of the grown h- BN are discussed in detail.

Chapter 4 focuses on device processing and electrical characterization for neutron testing. MSM detectors based on Ti/Au and Ni/Au interdigitated structures were fabricated using a 2.5 µm thick BN layer with natural and enriched ^{10}B. Then, MSM and PIN devices were fabricated from BGaN/GaN SLs. The I-V characteristics of the MSM-based BN, MSM and PIN based BGaN/GaN SLs under dark conditions and UV lamps are presented. The excess carrier transport mechanism, photocurrent and internal gain mechanism of the photodetector are recalled.

Chapter 5 presents the experimental results and discussion of neutron detection using natural and ^{10}B enriched BN detectors. I-V characteristics and I-t measurements under neutron fluxes are shown. This chapter also describes the neutron response of the BGaN/GaN SLs MSM and PIN devices.

Chapter 6 presents first the studies on the incorporation of Mg into h-BN and the heterostructures of Mg-doped h-BN on Si doped AlGaN template for the future development of efficient neutron detectors. Second, a new boron-rich BAlN material is investigated. The structural and morphological properties of BAlN are presented.

Chapter 7 is divided into three sections. First, the conclusion part summarizes the results of this thesis. Second, the perspective section highlights the further possible research directions for III-N based neutron detectors. The third section lists the articles published during the thesis period.

CHAPTER 1: OVERVIEW OF NEUTRON DETECTORS

1. Basic operation of neutron detectors

Neutrons are neutral subatomic particles and therefore cannot be affected by an electromagnetic field or by direct interaction with electrons in matter. Hence, neutrons are detected indirectly by their interaction with materials and the production of charged particles. A nuclear reaction occurs when an incident neutron is absorbed by the nuclei of matter. The daughter particles of the nuclear reaction, such as protons, alpha particles, lithium particles, and fission fragments, have large kinetic energies. These charged particles penetrate matter and lose their kinetic energy to create a cloud of electron-hole pairs. The electron-hole pairs are then moved by an electric field to the electrodes and produce an electric signal or light. A typical neutron detector consists mainly of three components:

- **Neutron converter or reactive materials:** the incoming thermal neutrons are converted into charged particles.
- **Active medium:** these charged particles generate excited carriers that produced electrical signal or light by recombining.
- **Electronic part:** displays the generated electrical signal.

In addition to these three components, a moderator can be used to slow down the incoming fast neutron on the detector. High density polyethylene (HDPE) is the most used moderator. The thermal neutrons are defined as free neutrons that have a kinetic energy of about 0.025 eV [1]. The neutron converter is characterized by its high neutron capture cross section. There are few elements in the periodic table that high enough neutron capture cross section to be used for thermal neutron detection. Most of the elements have capture cross section less than a barn (1 barn=$10^{-24}$$cm^2$) [1].

Table 1.1 lists the elements used for neutron detection and indicates how much kinetic energy is released in the reaction.

Table 1.1 List of nuclear reactions and the amount of energy released during the reaction (Q-values) between some common nuclei with neutron [1-2].

Isotope	Nuclear reaction	Q value (MeV)
Helium	$^{1}_{0}\mathrm{n} + {}^{3}_{2}\mathrm{He} \rightarrow \begin{cases} {}^{2}_{1}\mathrm{D} + {}^{2}_{1}\mathrm{D} \\ 1 \\ {}^{3}_{1}\mathrm{T} + {}^{1}_{1}\mathrm{H} \end{cases}$	0.764
Boron-10	$^{1}_{0}\mathrm{n} + {}^{10}_{5}\mathrm{B} \rightarrow \begin{cases} {}^{7}_{3}\mathrm{Li}\ (0.840\ \mathrm{MeV}) + \alpha(1.470\ \mathrm{MeV}) \quad 94\% \\ {}^{7}_{3}\mathrm{Li}(1.015\ \mathrm{MeV}) + \alpha\ (1.777\ \mathrm{MeV}) \quad 6\% \end{cases}$	2.31 2.792
Lithium	$^{1}_{0}\mathrm{n} + {}^{6}_{3}\mathrm{Li} \rightarrow {}^{3}_{1}\mathrm{T}\ (2.73\ \mathrm{MeV}) + \alpha(2.05\ \mathrm{MeV})$	4.78
Germanium	$^{1}_{0}\mathrm{n} + {}^{70}_{32}\mathrm{Ge} \rightarrow {}^{67}_{30}\mathrm{Zn} + \alpha$	2.963
Gadolinium	$^{1}_{0}\mathrm{n} + {}^{155}_{64}\mathrm{Gd} \rightarrow {}^{152}_{62}\mathrm{Sm} + \alpha$	8.339

Various types of neutron detectors have been made, such as gas-proportional counters, scintillators, and semiconductor-based detectors.

2.1 Gas proportional counters

Gas-filled detectors were among the first technologies used to detect neutron irradiation. Due to its high thermal neutron capture cross section of 5330 barns, gas-filled Helieum-3 (^{3}He) tube detectors are commonly used [3]. The ^{3}He absorbs incoming thermal neutrons and produces proton

(^{1}H) and triton (^{1}H) ions with a kinetic energy of 765 keV (Q value). The neutron detector based on ^{3}He has high detection efficiency (~80 %) and negligible sensitivity to gamma ray. It was the material of choice for neutron detection in the early 1980s [3]. The ^{3}He gas detectors are widely deployed in radiation portal monitors (RPMs) which are used to detect neutron radiation from nuclear materials. The RPM screens the transport vehicles across borders as shown in Figure 1-1 [4]. However, the use of these gas proportional counters is complicated by the high operating voltage (1000 V) required, the large footprint of the device, and the high pressure. In addition to the high manufacturing and maintenance costs, the worldwide shortage of ^{3}He has created a tremendous interest in alternative neutron sensitive materials. These alternative materials must be sensitive to neutron radiation and insensitive to gamma-ray interference.

Figure 1-1: Current ^{3}He based radiation portal monitoring (RPM) systems deployed for detection of fissile materials.[4]

2.1 Scintillators

Scintillator-based neutron detectors could be an alternative solution to replace ^{3}He gas detectors. Scintillators consist of neutron sensitive materials and photodetectors. The incoming neutrons are absorbed in the converter materials (lithium-6 or boron-10) and produce excited charge carriers that emit light by recombination. Photodetectors are then used to detect this emitted light indicating neutron capture. Scintillators have the advantage of being inexpensive and efficient. The reported efficiencies varies from 50 to 78% depending on the scintillators types (plastic, liquid) [4]. However, scintillators have similar detection probabilities for neutron and gamma-ray, which limits their ability to achieve adequate neutron/gamma discrimination [3-4]. The change from gas to solid state media offers a significant advantage in terms of material density, resulting in a much smaller device, robust and deployable devices, fast response time and low cost, which is desirable for many applications.

2.1 Semiconductor based neutron detectors

Before going into detail about solid-state neutron detectors, let us give some useful definitions of the main parameters of neutron detection.

1.3.1 Key parameters

- **Neutron detection efficiency**

The conversion efficiency (η) of a neutron detector depends on many parameters such as the neutron capture cross section of the converter layer and its crystalline quality, the device types (MSM, PIN) and the manufacturing process. The efficiency can be determined by using a certified neutron detector with known detection efficiency. To estimate the measured efficiency, the two detectors are placed in the same position during neutron irradiation and the efficiency is calculated using the following formula. [5]:

$$\eta = \frac{n_i}{n_0}\eta_0 \quad (1)$$

Where η_0 and n_0 are the detection efficiency and the generated count rate per unit area of the certified detector respectively, n_i is the generated count rate per unit area of the measured detector efficiency.

- **Interaction probability or maximum detection efficiency**

To estimate the detection efficiency of an h-BN based detector, the interaction probability (P) can be used and expressed as follows [6]:

$$P = 1 - \exp(-t/\lambda) \quad (2)$$

Where t and λ are the thickness and thermal neutron absorption length of the converter layer respectively. For natural h-BN, λ is equal to 237 μm for ^{10}B enriched BN is 47 μm [6].

- **Sensitivity ($\Delta I/Id$)**

The sensitivity of the neutron detector is defined as the difference between the measured current during neutron irradiation and the dark current measured without neutron flux. It is expressed as:

$$\Delta \mathrm{I} = (I_{measured} - I_{dark})/Id \quad (3)$$

1.3.2 State-of-the-art of solid-state neutron detectors

The solid-state neutron detectors can be divided into two categories: i) indirect conversion neutron detectors and ii) direct conversion neutron detectors [1]. The indirect neutron detector consists of neutron absorbing materials (^{6}Li, ^{10}B, ^{157}Gd) and usually an active planar device structure (separate semiconductor detector). On the other hand, in the direct neutron detectors, neutron capture, charge carrier generation and charge collection take place in the same materials

(neutron absorbing layer), which offers tremendous advantages over the indirect conversion such as higher charge carrier collections and simple device structure.

a) Indirect conversion neutron detectors

Indirect neutron detectors based on semiconductors have been extensively studied with various designs. One design consists of electronic devices coated with a neutron reactive material. For example, this could be a silicon PN junction coated with a converter material [7] such as boron-10 (^{10}B), which is used for its large capture cross section for thermal neutrons (see Figure 1-2). In this case, the efficiency is limited to less than 5% [8] because the reaction product is absorbed in the converter material itself. If the boron layer is too thick, the generated charge particles (α and 7Li particles) will be absorbed before they reach the silicon-PN junction. This is a design challenge because the converter material must be sufficiently thick to capture most of the incident thermal neutrons. This problem results in a device with inefficient charge carrier production, which translates directly into low neutron detection performance.

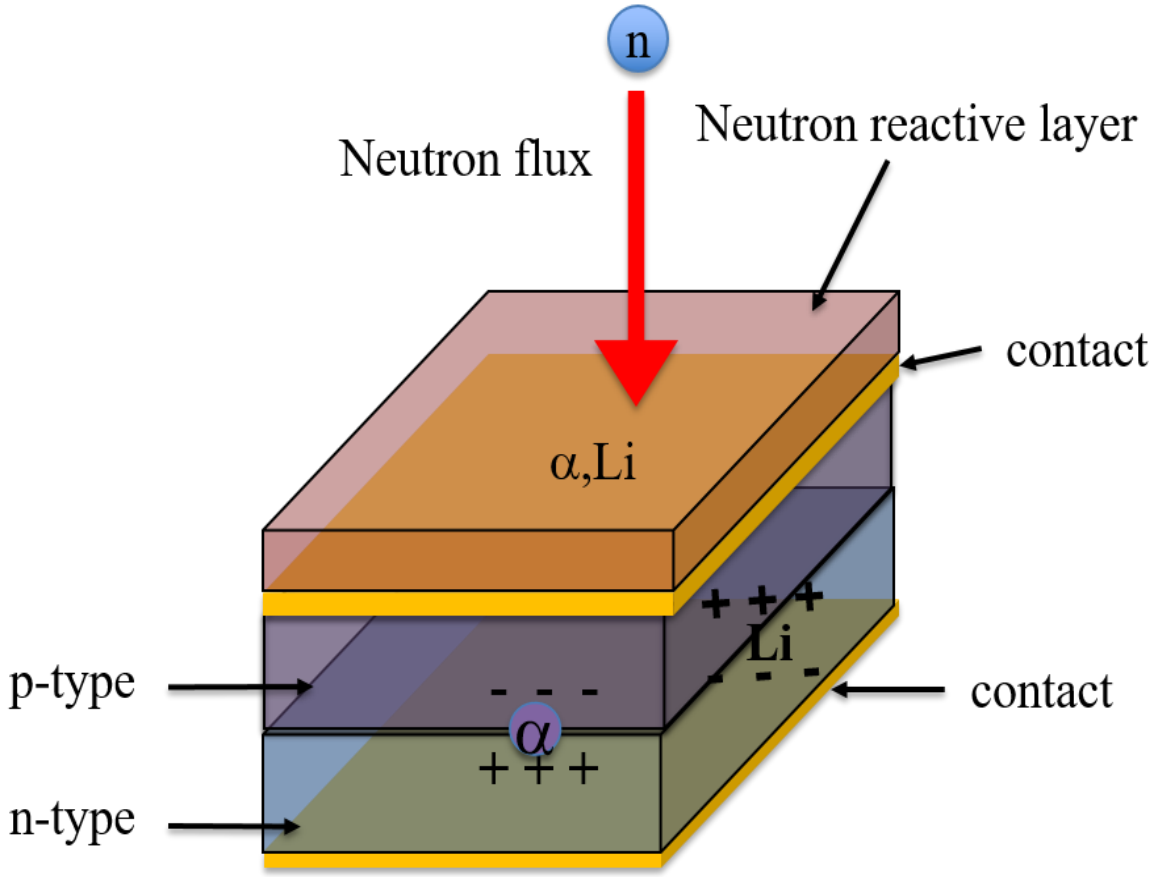

Figure 1-2: 2D Planar structure of B-10 layer on Si PN based detector.

Another design of a semiconductor-based neutron detector allows overcoming this limitation and consists of a semiconductor device (diode) partially made of neutron-reactive material. An example of this type of neutron detector is microstructured semiconductor devices with small channels etched into the surface of the semiconductor substrate backfilled with a neutron reactive material [9-10], as shown in Figure 1-3. Such devices, based on the silicon diode PIN, can have efficiencies as high as 48% [10], but suffer from low radiation hardness [11] and require a rather complicated fabrication process.

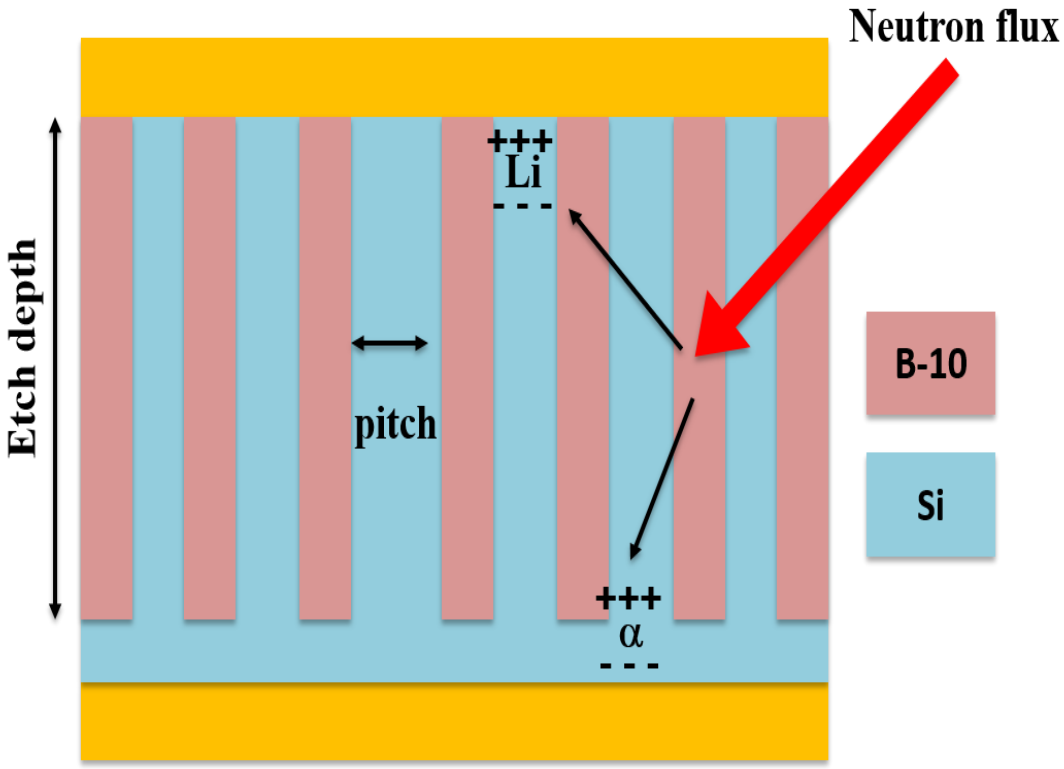

Figure 1-3: 3D design of Si pillar based detector [9].

b) Direct conversion neutron detectors based on III-N

III-N-based detectors have two very important advantages over Si-based detectors. First, the radiation hardness of GaN is about two orders of magnitude higher than Si [11]. Second, GaN has a wide band gap of 3.4 eV, which enables much more robust performance above room temperature compared to Si. Among the III-N, hexagonal boron nitride (h-BN) is a uniquely useful material for neutron detection due to its high thermal neutron capture cross section. In addition, h-BN has very low sensitivity to gamma rays due to its relatively low density (2.2 g cm-3), which makes it more attractive for thermal neutron detection than other semiconductor materials [12-14]. Other outstanding physical properties of h-BN include chemical inertness, high thermal conductivity, high mechanical strength, and large band gap (~6 eV), which make it one of the preferred materials for new applications, including deep UV (DUV) optoelectronics [11, 15].

Natural BN contains 20% ^{10}B and has an effective absorption length of 277 μm for thermal neutrons, which decreases significantly to 47 μm when the ^{10}B is enriched to 100% [16]. Moreover, in the neutron detectors based on BN, neutron capture, charge carrier generation and charge collection take place in the same layer, which makes them a good candidate for direct conversion of thermal neutrons.

Once a ^{10}B atom captures a neutron, it undergoes the following nuclear reactions:

$$^{10}_{5}B + {}^{1}_{0}n \rightarrow {}^{7}_{3}Li + {}^{4}_{2}\alpha\ (2.78MeV) \qquad (6\%), \text{ excited state} \qquad (1)$$

$$^{10}_{5}B + {}^{1}_{0}n \rightarrow {}^{7}_{3}Li^{*} + {}^{4}_{2}\alpha(2.3MeV) \qquad (94\%), \text{ ground state} \qquad (2)$$

The daughter particles of nuclear reaction equations 1&2, i.e. alpha and lithium particles, have large kinetic energies. The average energy of the daughter particles is 2.34 MeV. These charged particles penetrate the BN layers and lose their kinetic energy to create a cloud of electron-hole pairs, as shown in Figure 1-4. Subsequently, the electron-hole pairs are driven to the electrodes by an electric field to produce an electric signal.

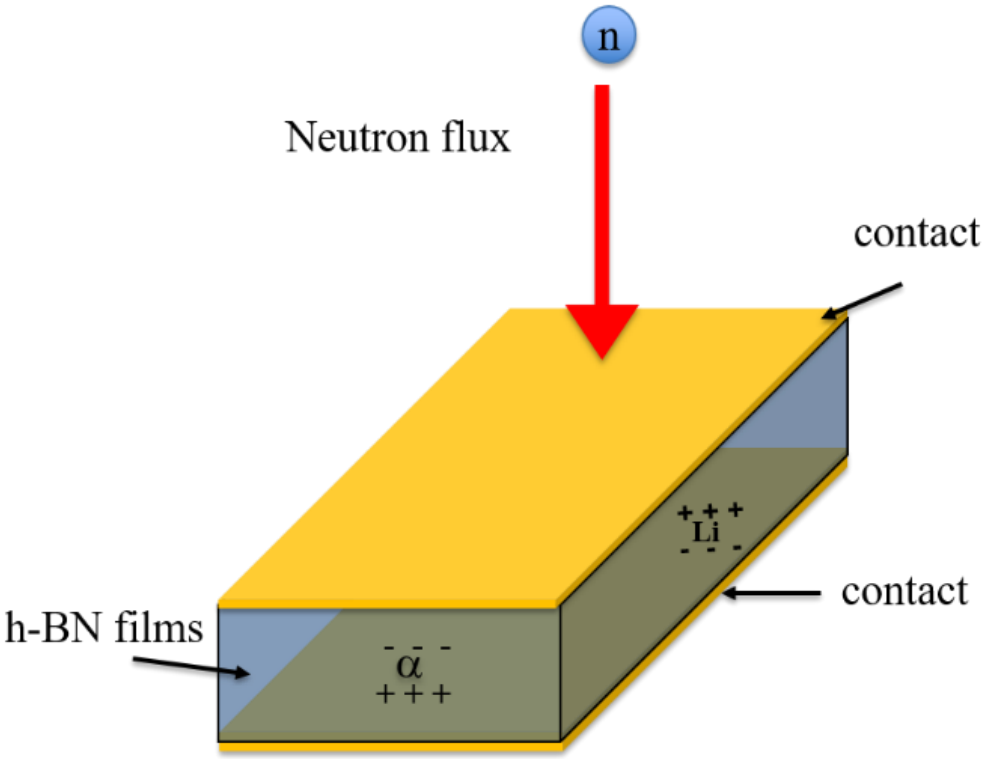

Figure 1-4: Schematic of h-BN neutron detector.

Various types of designs and device structures have been used to fabricate neutron detectors based on BN. McGregor et al [17] have demonstrated for the first time the feasibility of pyrolytic BN -based neutron detectors with efficiencies up to 7.2% at an electric field of 4 kV/cm. The scatter of efficiency values from one detector to another was attributed to the poor charge transport in the device. Later, Li et al [18] reported 1µm thick monocrystalline h-BN based interdigitated (5µm spacing) planar MSM devices. For this device, a very low dark current and neutron induced current (ΔI) of 0.085 pA were measured when operated at a voltage between 20V and 200V. The same type of device, but with a 0.3 µm thick BN, was then found to be sensitive to neutron flux and insensitive to gamma rays [19]. It also inhibited an enhanced ΔI of 25 pA when operated at 40 kV/cm. To further improve the neutron detection efficiency, Doan et al [6] fabricated the same type of MSM device but with ^{10}B enriched 2.7 µm thick BN. As a result, an

efficiency of 4% was obtained for this device when operated at a voltage higher than 20V. For planar neutron detectors, there are limitations on the collection efficiency when the BN thickness is increased. Maity et al [5] studied a vertical photoconductive structure based on 50 µm thick BN enriched with ^{10}B. A neutron detection efficiency of 58% was achieved when the device was operated with a surface area of 1x1 mm^2 at 5 kV/cm. With the same aim, Maity et al [20] considered a MSM structure based on 90 µm thick h-BN enriched with ^{10}B, where the electrical contacts were deposited on the vertical sides of the mesa obtained by etching. A neutron detection efficiency of more than 50% was obtained when the device was operated with a surface area of 28.8 mm2 at 4.17 kV/cm. Recently, Li et al. reported an improvement in the collection efficiency due to a reduced surface recombination field and an increased electron mobility lifetime product [21]. These promising results on neutron detectors based on BN have been reported by only one group, so many parameters need further optimizations.

2. Research problems

2.1 Boron-containing III-Nitride (BGaN, BAlN)

By using boron alloys such as BGaN, BAlN, it is possible to obtain robust devices that have both the conversion and neutron detection functions and thus do not require a neutron converter layer. Our group was among the pioneer in developing the diluted boron into GaN and AlN [22-28]. Record concentration of boron into GaN and AlN has been obtained 3.6% and 12% respectively. The boron content in these alloys is an important factor as they absorb thermal neutrons and produce daughter particles, which in turn produce electron-hole pairs by losing their energy. Atsumi et al. reported a BGaN-based thermal neutron detector in which 200 nm BGaN alloy with a B content of 1.2% was grown on a 1 µm thick GaN/sapphire layer using MOVPE [29]. The BGaN Schottky diode showed a very low signal for thermal neutrons. For sensitive neutron detectors based on boron alloys (BGaN, BAlN), a high boron content is crucial for

effective absorption of thermal neutrons. Unfortunately, as it has been reported by our group a thick BGaN layer with high B content leads to layer cracking due to the stress relaxation produced by the high B content [30-31].

To overcome the quality issue we have developed a new approach using superlattices (SLs) of BGaN and GaN semiconductors. In this case, a thin GaN layer is inserted between the BGaN layers to reduce the strain and hence the strain relaxation is avoided. Since the different layers are only a few nm to a few tens of nm thick, the boron content can be high enough and the final stack can reach a thickness of a few hundred nanometers, allowing for high neutron conversion efficiency.

2.2 Hexagonal boron nitride (h-BN) based neutron detectors

Highly efficient neutron detectors based on BN require very thick BN layers due to the large neutron absorption length of BN. It is 277 µm for natural BN and 47 µm for 100% enriched with ^{10}B BN [6]. These thick BN layers lead to two major challenges: (a) the growth of a very thick BN layer poses some technical challenges and is hardly conceivable for industrial applications, since the growth time for a few micrometers is almost a day. In terms of the device, only the charge carriers generated near the electrodes are collected to produce a neutron signal. (b) Above a film thickness of 1µm BN, poor crystalline quality is observed leading to low efficiency due to low carrier collection (defects/traps). Improving the crystalline quality of the thick BN layer is a major challenge. In this work, we have investigated an alternative solution, namely the use of MSM structures based on thin BN films, and explored the benefit of BN MSM detectors. With MSM structures, it is possible to achieve self-powered detectors operation with a gain mechanism which has not yet been studied for BN. In addition, we have investigated a direct comparison of natural and ^{10}B-enriched BN neutron detectors using the same growth conditions, film thicknesses, and electrical contact fabrication conditions.

Another alternative solution is the realization of p-n or p-i-n heterojunctions of BN for neutron detection. This will improve the charge carrier collection and the overall efficiency of the detector. Previously, it was reported that p-doping of h-BN can be achieved using Zn, Be and Mg as dopants [32-38]. Recently, conflicting experimental and theoretical studies on the p-conductivity of h-BN have been published. Experimental works report a good control of the p-type conductivity of h-BN by in situ doping with magnesium, with an activation energy of 30-300 meV [36, 37, 39]. On the other hand, density functional theory studies (DFT) predict that p-type h-BN using Mg is most likely not possible, since the formation of small hole polarons increases the Mg ionization energy to more than 1 eV [40]. In this work, I have dealt in detail with the incorporation of Mg in h-BN layers and the control of the conductivity of the Mg-doped h-BN layers.

CHAPTER 2: INTRODUCTION TO III-NITRIDE MATERIALS

The III-nitride materials are compound semiconductors based on the combination of group III elements (Ga, Al, In and B) with group V nitrogen atoms. They are widely used in modern electronic and optoelectronic applications. This is due to their exceptional electronic, physical and optical properties. In this chapter, we present the basic properties of the III-N materials and the tools that have been used to grow and characterize them.

1. III-Nitrides materials

The successful demonstration of light emitting diodes (LEDs) [1-4], laser diodes (LDs) [5], high electron mobility transistors [6-8], and photodetectors in the UV range [9-14] have led to nitrides being the focus of research and commercial interest over the last two decades. III-Nitrides are aluminum nitride (AlN), gallium nitride (GaN), indium nitride (InN), boron nitride (BN) and their alloys such as AlGaN, AlInN, InGaN, BGaN, BAlN, etc. The band gaps range from 0.7eV (InN) to 6.2eV (AlN) with emission spectra ranging from near infrared through the entire visible range to ultraviolet wavelengths [15]. Figure 2-1 shows the band gap energies as a function of the lattice parameters of the III-nitrides [16].

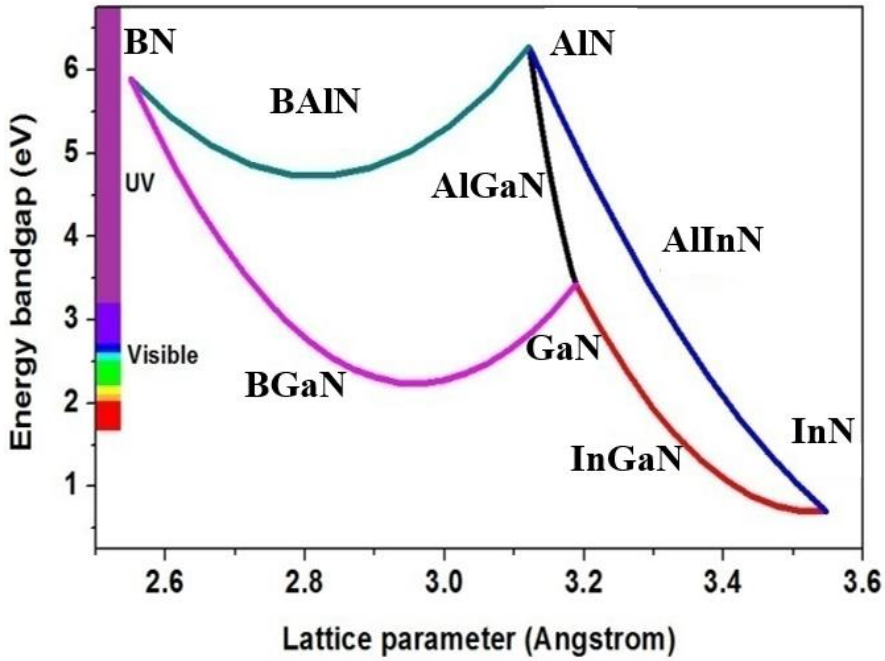

Figure 2-1: III-nitrides bandgap energies versus in-plane lattice parameter [16].

Compared to the conventional III-V semiconductors (phosphides, arsenides, etc.), III-nitrides (GaN, InN, AlN) were developed very late. This is due to the lack of a compatible substrate, high N-vapor pressure, and the challenge of achieving p-type doping. The III-nitrides are usually grown on commercially available, inexpensive and thermally stable sapphire substrates. The growth of the III-N materials on large lattice mismatch substrate leads to a high density of threading dislocations (TDDs) in the grown structure. Typically the TDDs for GaN grown on sapphire is in the order of 10^{8}-10^{10} cm^{-2} [17-21].

1.1 Fundamental properties of III-N materials

III-nitrides are most stable in the wurtzite crystal configuration under typical MOVPE growth conditions [15]. The wurtzite lattice consists of two intertwined hexagonal sub-lattices, one anion sub-lattice occupied by elemental nitrogen atoms and the other cation sub-lattice occupied by the elements of the III group (Ga, In, Al, B). Each sub-lattice is shifted along the c-axis by 3/8 of the cell height and each atom in the lattice is tetrahedrally coordinated, as shown in Figure 2-2.

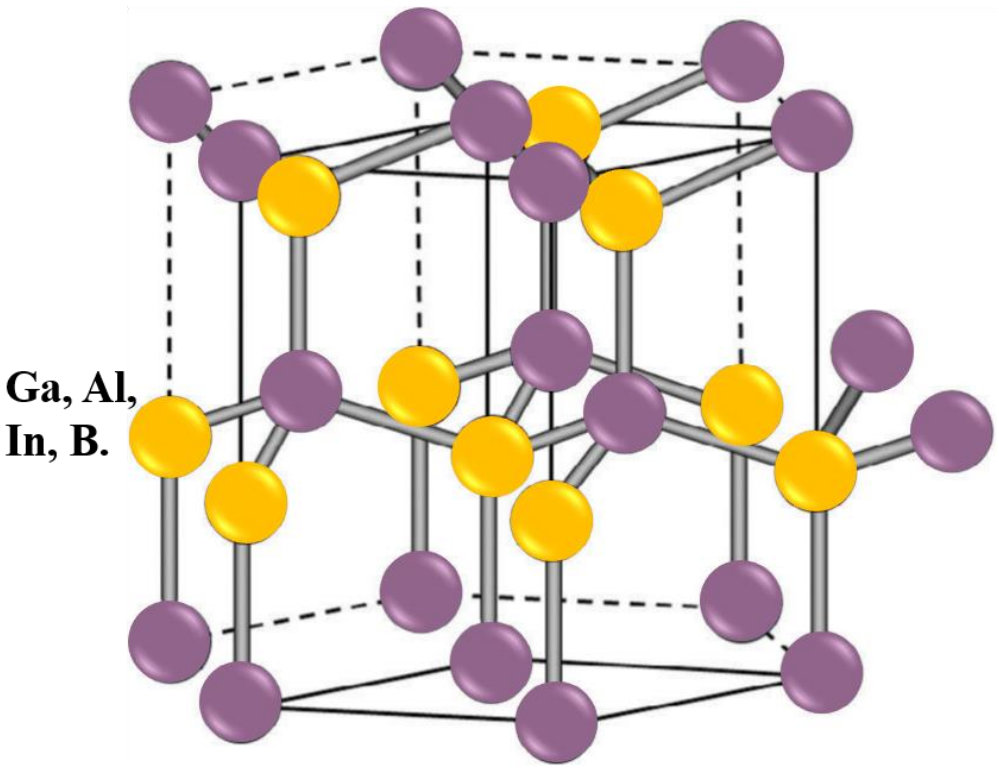

Figure 2-2: Wurtzite crystal structure of III nitrides [22].

Strong covalent bonds exist between the elements III and nitrogen [22] due to the large difference in electronegativity between III elements and nitrogen atoms, resulting in chemically and physically stable III-nitrides. The lattice parameters and thermal expansion coefficients of BN, AlN, GaN and InN are summarized in Table 2-1.

Table 2-1: Summary of structural parameters of III nitrides. Data from references [23].

Parameter (Unit)	**GaN**	**AlN**	**InN**	**BN**
$\boldsymbol{a(A)}$	3.189	3.112	3.545	2.55
$\boldsymbol{c(A)}$	5.185	4.982	5.703	4.17
$\boldsymbol{E_{g(eV)}}$	3.42	6.28	0.7	5.9
Thermal expansion $(\Delta a/a)$ $(\mathbf{10^{-6}K^{-1}})$	5.59	4.15	3.8	-2.7
Thermal expansion $(\Delta c/c)$ $(\mathbf{10^{-6}K^{-1}})$	3.17	5.27	2.9	38
Thermal conductivity ($W.cm^{-1}K^{-1}$)	1.3	2.85	0.45	6(||a), 0.3 ($\perp$a)

To calculate the lattice parameters, we consider the III-nitrides AN, BN and $A_xB_{1-x}N$, where x is the composition of the alloy. Then the lattice constant a^{ABN} of the ternary alloy is given by Vegard's law as follows [23]:

$$a^{ABN} = xa^{AN} + (1 - x)a^{BN} \quad (1)$$

Similarly, the lattice constant a^{ABCN} of the quaternary alloy $A_xB_yC_{1-x-y}N$ is given by:

$$a^{ABCN} = xa^{AN} + ya^{BN} + (1 - x - y)a^{CN} \quad (2)$$

The energy band gaps Eg of III-nitride alloys can also be calculated directly from their binary values as:

$$E_g(A_xB_{1-x}N) = E_g(AN) \times x + E_g(BN) \times (1 - x) - b \times x \times (1 - x) \quad (3)$$

Where b is the energy band gap bowing parameter. Table 2-2 summarizes some bowing values of III-nitrides.

Table 2-2: Bandgap bowing parameters of III-nitrides ternaries.

Alloys	BAlN	BGaN	AlGaN	AlInN	InGaN
Bowing (eV)	5.45 [24]	9.2 [25]	1 [26]	2.5 [26]	2 [26]

1.2 Hexagonal boron nitride (h-BN)

a) Structural properties of h-BN

Boron nitride belongs to the III-nitride materials that crystallize in different phases, such as the hexagonal (h-BN), cubic BN (c- BN), wurtzite BN (w- BN), and rhombohedral BN (r- BN) phases [27]. The hexagonal form is the most stable phase and crystallizes in a hexagonal layered structure similar to graphite and is referred to as "white graphite". The boron and nitrogen atoms are bound by strong covalent bonds within each layer of h-BN, while the stacking layers are held together by weak van der Waals forces, as shown in Figure 2-3. The length of the covalent B-N

bonds is 1.45 Å and the distance between the layers is 3.3 Å. Therefore, the two different types of bonds lead to a high degree of anisotropy in most properties of h-BN.

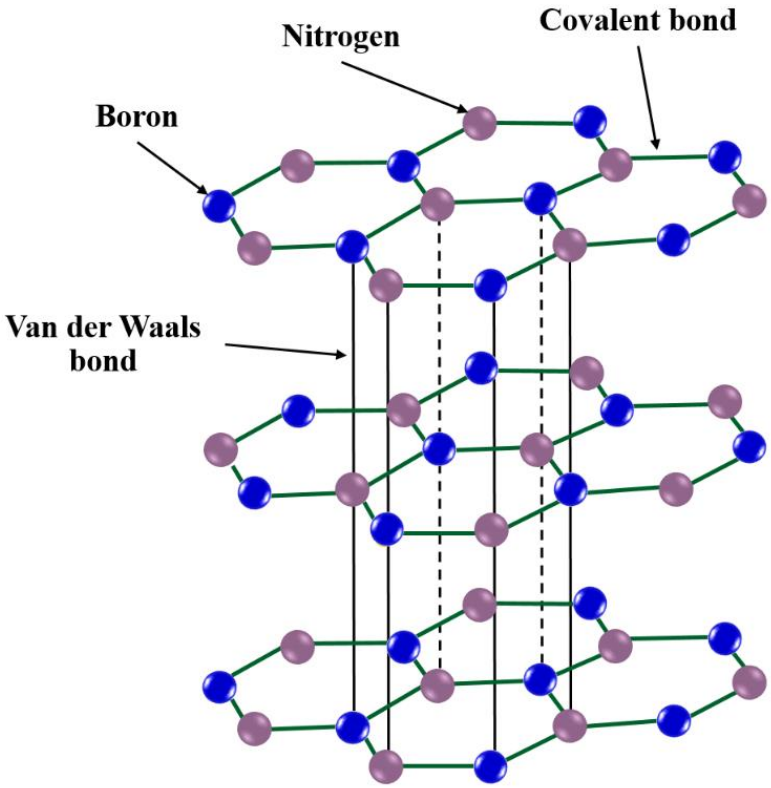

Figure 2-3: Crystalline structure of h-BN [27]

As for the stacking order, the h-BN layers are stacked in a AA' configuration with the boron atoms (B) overlying the nitrogen atoms (N) and vice versa, as shown in Figure 2-3. It is reported that BN has an indirect and wide band gap of about 5.95 eV [27-29]. However, a single atomic layer of h-BN has a direct gap of 6.1 eV [27, 30]. Hexagonal BN films have a variety of attractive properties, including high temperature stability, low dielectric constant, high thermal conductivity, large band gap, high mechanical strength, chemical inertness, and large thermal cross section. It is stable in air up to 1000 ^{o}C [27], under vacuum up to 1400 ^{o}C, and in an inert atmosphere it can be used up to 2800^{o}C, which makes it a potential material for antioxidant coatings [31]. The layered structure of h-BN combined with its close in-plane lattice match with graphene makes it an ideal

template and dielectric layer for graphene electronics [32-33]. Some of the basic parameters of h-BN are listed in Table 2-3.

Table 2-3: Basic parameters of h-BN [34]

Basic parameters	values
Lattice constant (a)	2.5 Å
Lattice constant (c)	6.66 Å
Electron affinity	-4.5 eV
Thermal conductivity ($k_{\|\|}$)	0.3 $W.cm^{-1}.{}^{o}C^{-1}$

b) Growth of h-BN

The growth of high quality h-BN is hampered by the lack of inexpensive lattice-matched substrates, the high growth temperature, and the parasitic reaction in the gas phase between the precursors (NH3 and TEB). In 1986, Nakamura et al. predicted that a temperature of 1500 ^{o}C should be reached for the growth of h-BN on sapphire [35]. This study was confirmed by Chubarov et al. who reported an improvement in crystalline quality and a decrease in impurity concentration (carbon and oxygen) at high growth temperature [36]. This leads to a sophisticated growth system that can support growth at high temperatures. Different methods have been used to grow h-BN. The high pressure high temperature method HPHT has been used for the synthesis of bulk crystals of h-BN [37-39]. The major limitation of HPHT method is its scalability, so it cannot be used for large-scale device applications. Therefore, other techniques such as chemical vapor deposition (CVD), molecular beam epitaxy (MBE), and metal organic vapor phase epitaxy (MOVPE) have been explored to grow h-BN in large area. Large-area single-layer thick films of h-BN were obtained by CVD method on transition metal templates [40]. From few layers to 100 µm thick h-BN films were performed by metal organic vapor phase epitaxy (MOVPE) using ammonia (NH_3) and triethylboron as N and B precursors, respectively. Kobayashi et al [41-44] first reported the

epitaxial growth of h-BN films on Ni, graphitized 6H-SiC and sapphire (Al_2O_3) by MOVPE. Recently, our group reported for the first time 2D layered thin h-BN films with different thicknesses up to 60 nm on large-scale (2 inch) wafers [45]. Later, Li et al. from our group reported the growth of BN films with thickness up to 2.5 um, which were used to demonstrate efficient deep UV detectors [46]. These results show that good quality h-BN can be grown at a temperature below 1500 ^{o}C, which allow us to investigate BN materials as neutron detectors.

1.3 BGaN, BAlN alloys

BGaN alloys are a very interesting material due to their wide band gap and lattice matching with the 6H-SiC substrate [47-49]. BGaN alloys with high crystalline quality were successfully grown by MOVPE on GaN template substrates in Pr. Abdallah's group. Boron was incorporated up to 3.6% in the GaN material. These significant advances in the growth of BGaN films have led to various applications, especially Bragg reflectors, high electron mobility transistors, and gas sensors [50-52]. In BAlN alloys we have two types. The first is Al-rich BAlN, which consists of alloying born into AlN. This material has been widely studied in our group and boron content up to 12% has been obtained [53-55]. The second alloy is the boron-rich BAlN, which consists of alloying Al into BN. The growth of boron-rich BAlN alloys has not yet been studied in the literature. The growth of boron-rich BAlN alloys and the understanding of their basic structural and optical properties are of great importance for the realization of neutron detectors.

2. Experimental tools

2.1 Metal Organic Vapor Phase Epitaxy (MOVPE)

Metal organic vapor phase epitaxy (MOVPE) was first described by Manasevit [56] in 1968 using organometallic compounds. The MOVPE system is used to grow high quality materials with excellent uniformity of film thickness in large scale production, with near atomically abrupt

interfaces. The versatility and the easy scale up (multi-wafers systems) of MOVPE are the main advantage over other growth techniques (MBE, VPE) for the growth of all III /V and II /VI semiconductors and alloys [57]. A typical MOVPE system consists of the following components:

- Gas mixing cabinet for supplying precursors into the reactor chamber.
- Reactor chamber where the deposition of materials takes place.
- Exhaust system (main pump, scrubber, particle filter, etc)
- Control system such as automatic (2/3/5 way) valves, mass flow controllers (MFCs), pressure controller.

The general schematic of the MOVPE system is shown in Figure 2-4 [58]:

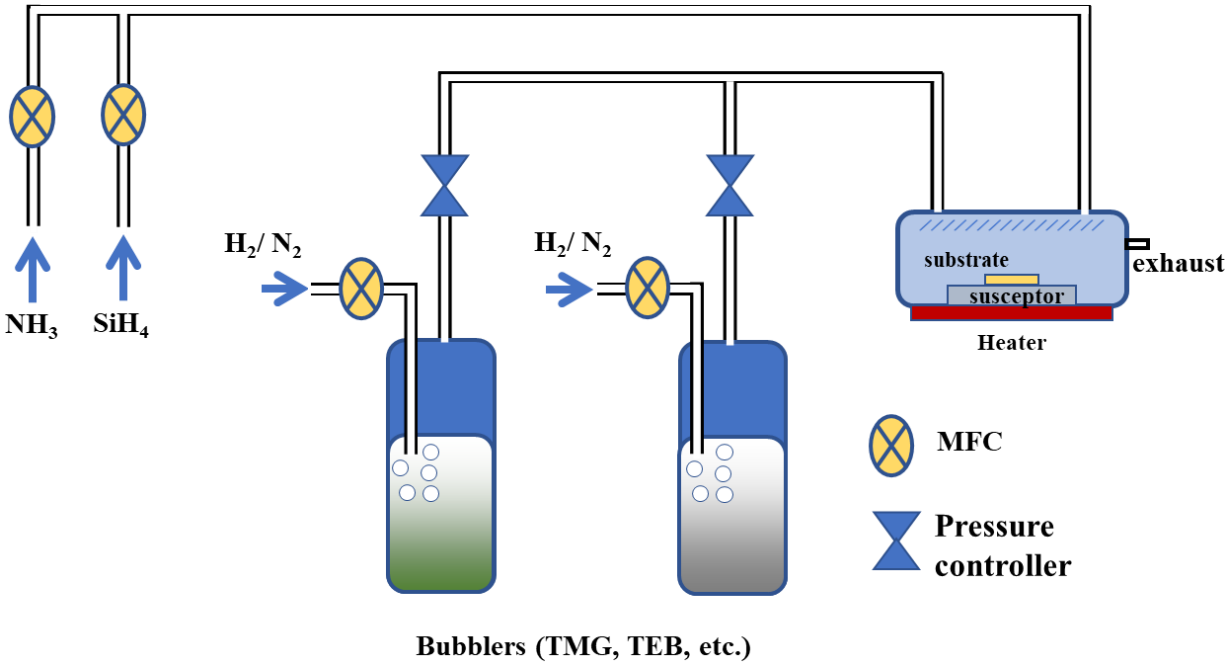

Figure 2-4: Schematic of MOVPE reactor system [58].

The growth process in MOVPE is governed by the convection of the metal organic vapor species over a heated zone [57]. For III-nitride growth, ammonia (NH3), trimethylgallium (TMG), thriethylgallium (TEG), trimethylaluminum (TMAl), triethylborane (TEB), and trimethyindium

(TMIn) are commonly used as precursors. In addition to the precursors, carrier gasses such as hydrogen (H_2) and nitrogen (N_2) are used to improve mixing and control laminar flow in the chamber. The precursors are stored in stainless steel bubbles that are maintained at a constant temperature. The carrier gas flows into the bubblers, is saturated with the vapor of the source molecules, and is carried out into the growth chamber (reactor). The scheme of epitaxial growth of III-nitride is shown in Figure 2-5.

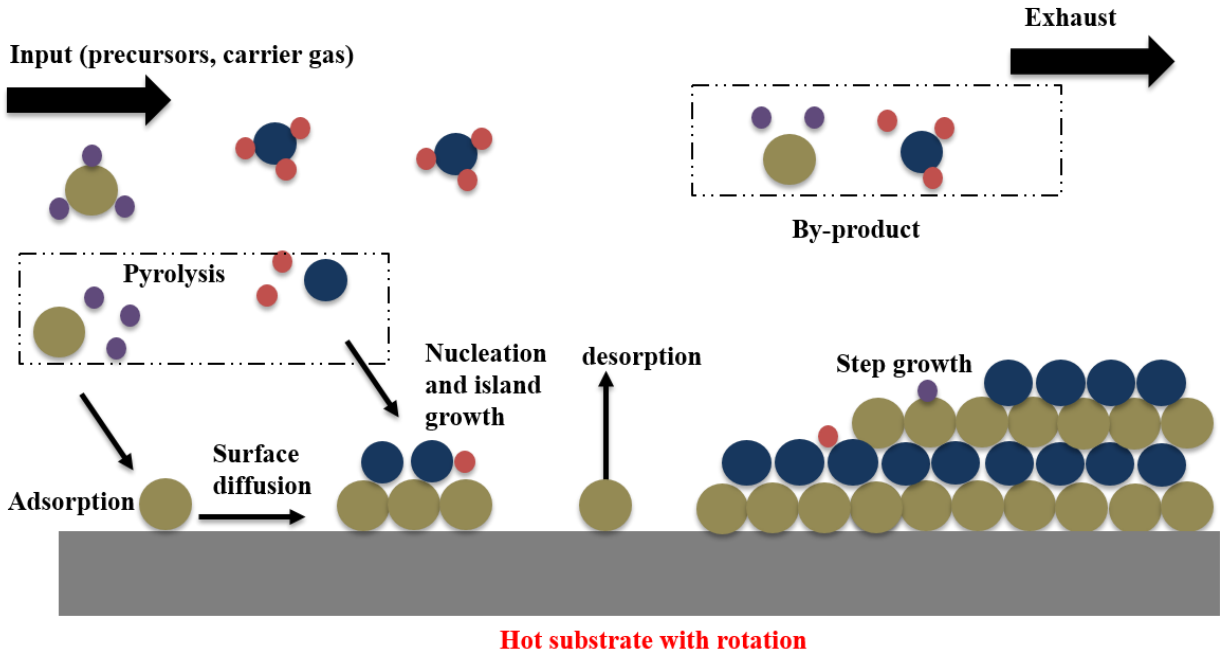

Figure 2-5: Schematic of III-nitride epitaxial growth [57]

The substrate is on a heated susceptor in the reactor chamber, where the organometallic precursors and ammonia are mixed and decomposed into species (pyrolysis). The resulting species diffuse through the boundary layer to the surface and attach to the substrate by adsorption. The species may desorb at this moment or react with other surface species. To form a new layer, the species

can diffuse on the surface and nucleate at thermodynamically favorable sites to form islands, resulting in growth of the material.

The reaction equation for the growth of gallium nitride (GaN) is described as follows.

$$Ga\,(CH_3)_3 + NH_3 \rightarrow GaN + 3CH_4\uparrow$$

The byproducts formed diffuse into the carrier gas and flow into the reactor exhaust. MOVPE growth is a complex process involving thermodynamics, kinetics, hydrodynamics and mass transfer. The theoretical details can be found in [57,58]. To control the growth rate and quality of epitaxial layers, several basic interdependent growth parameters can be set. These parameters are the growth temperature, the reactor pressure, the ratio of the ammonia flow rate to the total flow rate of the III element precursors (V/III ratio), the concentration of a precursor in the total precursors for III elements (III/III), and the carrier gas. The optimal V/III ratio is very important for the quality of epitaxial layers. If the V/ III ratio is too low, the supply of nitrogen atoms would be inefficient, and nitrogen vacancies and automatic background doping would increase. However, if the V/III ratio is too high, parasitic reactions will be enhanced and the surface mobility of adsorbed atoms will be hindered. For the composition of ternary or quaternary alloys, the ratio III /III is the parameter that needs to be adjusted. It should be noted that for the same gas phase concentration (III/III), the composition can also be shifted by other parameters such as temperature, pressure or the change of the strain state (pulling effect of the composition).

The growth rate depends on the reactor temperature and three growth regimes can be distinguished [57,58]. At low temperature, the growth rate is limited by the chemical reaction rate (decomposition or desorption at the surface), which can be expressed by the Arrhenius law as follows:

$$R = Ae^{(-E_a/kT)} \quad (1)$$

where A is the pre-exponential factor, R is the chemical reaction rate, Ea is the activation energy, k is the Boltzmann constant, and T is the temperature in K. In this regime, the growth rate increase with increasing temperature.

In the intermediate temperature range (800 to 1200 ºC for the growth of GaN from TMG and NH3), the growth rate is dependent on precursor supply and almost independent of temperature, where most of the MOVPE growth occurs. This regime is referred to as "mass transport limited".

At higher temperatures (above 1200 ºC), the growth rate is limited by thermodynamic factors such as desorption and dissociation of the crystals with increasing temperature. The three regimes are summarized in Figure 2-6.

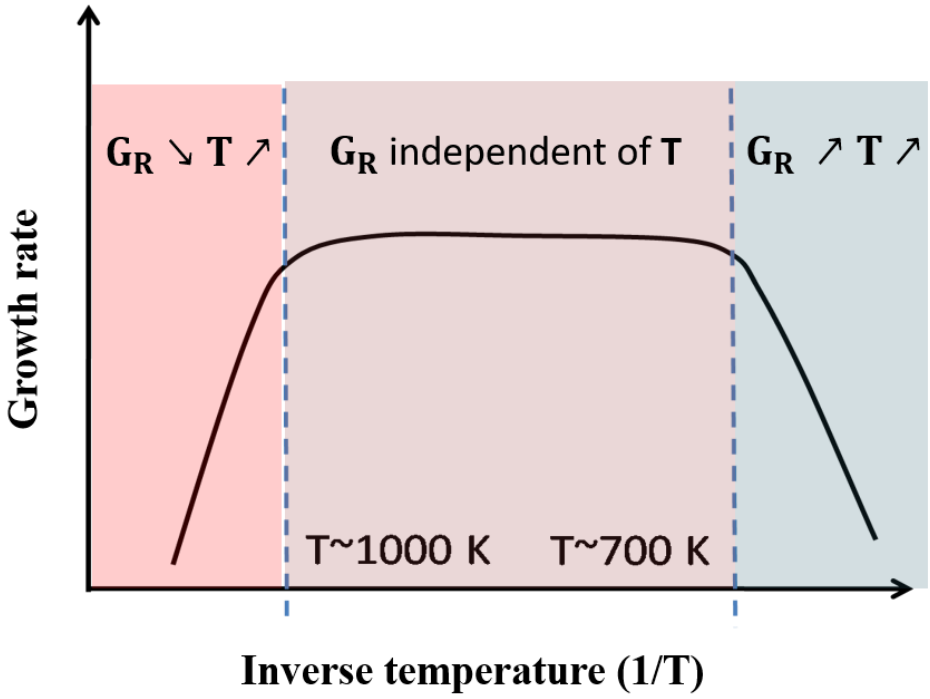

Figure 16: Growth rate as a function of inverse temperature [58].

In this work, we have used two MOVPE reactors, the homemade T-shaped reactor for the growth of BGaN/GaN SLs and the CCS-Aixtron reactor for the growth of the h-BN layers, BAlN alloys and the p-GaN on the BGaN/GaN SLs.

a) T-shape reactor

The metal organic vapor phase epitaxy (MOVPE) system was designed and installed by Prof. Abdallah Ougazzaden [59], as shown in Figure 2-7. This system consists of four basic elements: a gas handling system, a reactor chamber, a heating system, and an exhaust gas pumping system. The temperature can be as high as 1040 ^{o}C and the pressure in the reactor can be regulated from 80 to atmospheric pressure. H2 or N2 can be used as the carrier gas. The cold wall system is used so that the substrate is much hotter than the other zones. During growth, the substrate is rotated at 60 rpm to improve the homogeneity of the layers and maintain laminar flow on the sample surface.

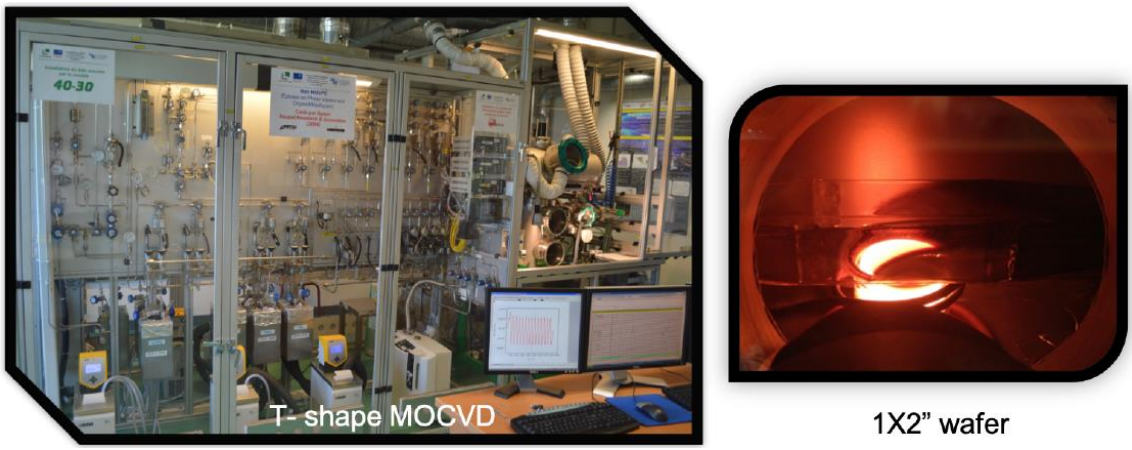

Figure 2-7: MOVPE gas panel and T-shape growth chamber

b) Close coupled showerhead (CCS) reactor

An Aixtron 3×2 inch Close Coupled Showerhead (CCS) MOVPE system was installed in CNRS-IRL 2958 laboratory as shown in Figure 2-8. Compared with the T-shaped reactor, a higher

surface temperature of the substrates can be achieved. It can reach up to 1300 ºC, which enables us to grow h-BN.

Figure 2-8: Aixtron 3x2 inch, close coupled showerhead (CCS) MOVPE system.

2.2 Characterization tools

In this work, we have used different types of characterization techniques to evaluate the properties and quality of the grown materials.

a) X-ray diffraction

X-ray diffraction is a nondestructive characterization method that can be used to determine the composition, thickness, lattice parameters, strain, and dislocation density of III-nitride epitaxial films. The wavelength of the incident X-rays is in the range of crystal lattice parameters. The incident X-rays are reflected from a number of crystal planes. The interference of the scattered rays will be alternately constructive or destructive. The constructive interference, known as diffraction peaks, can be determined using Bragg's law:

$$n\lambda = 2d \sin \theta.$$

Where n is the diffraction order, λ is the wavelength of the X-rays, θ is the angle between the diffraction planes and the incident X-ray beam, and d is the distance between the diffraction planes (Figures2-9b).

In this work, HRXRD measurements were performed in a Panalytical X'pert Pro MRD system using Cu Kα radiation (Cu Kα1: 1.5405 Å), as shown in Figure 2-9a. The height of the X-ray beam from the hybrid monochromator is 1.2 mm and the resolution ~ 12 arcsec. The FWHM value was determined for all samples by fitting the (002) peak of the h-BN.

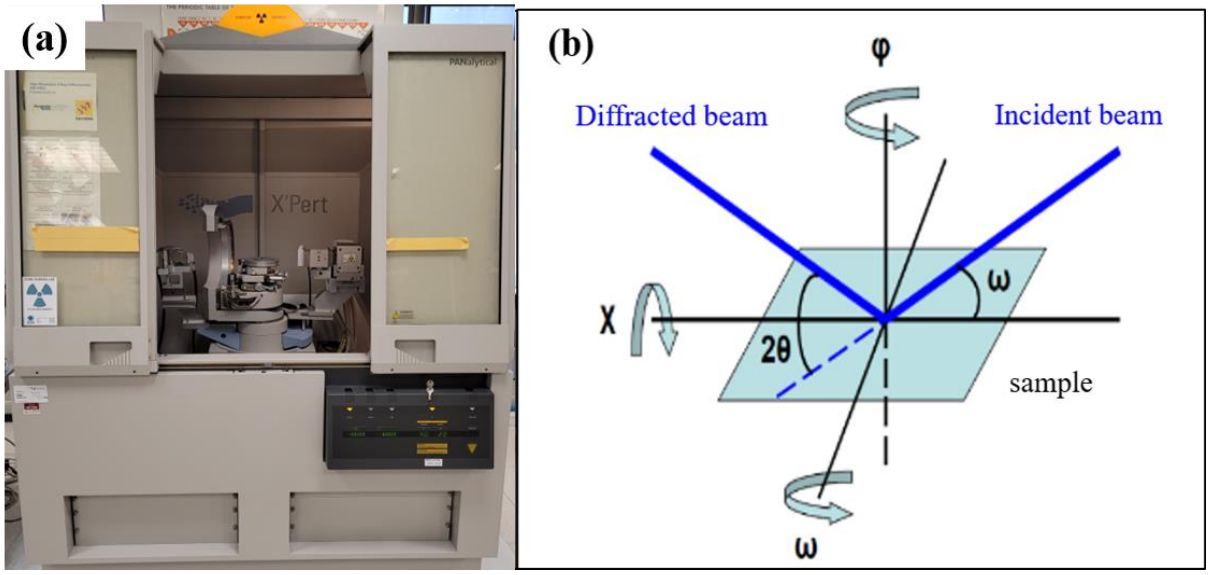

Figure 2-9: High-resolution X-ray diffraction system.

b) Scanning electron microscope (SEM)

A scanning electron microscope reproduces images of the surface morphology of the sample by scanning it with a focused beam of high-energy electrons [60]. The interaction between the electrons and the atoms in the sample produces signals of secondary electrons. The surface morphology of the sample can be determined by collecting the secondary electrons with a special

detector. In this work, the Zeiss supraTM 55VP was used to create the SEM images (see Figure 2-10).

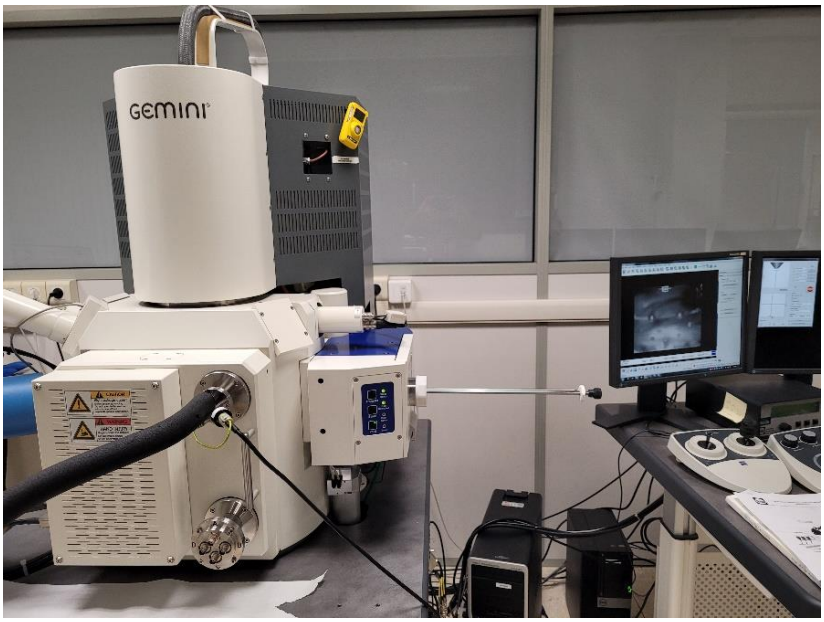

Figure 2-10: SEM system used for morphological characterization

c) Atomic force microscopy (AFM)

AFM microscopes are used to measure surfaces morphology at the nanoscale. It is also a nondestructive technique. The AFM system has a cantilever with an extremely sharp tip, usually made of Si3N4 or Si. The basic function of AFM is to scan surfaces with a tip in the nanometer range. It consists of moving the tip closer to the sample surface. The interaction forces between the tip and the sample cause the cantilever to bend, which is detected by a laser diode and a photodetector [61]. The movement of the probe over the sample surface is controlled by a feedback loop and a piezoelectronic scanner that moves moving the sample under the tip. There are AFM modes, tapping mode, contact mode and non-contact mode. The main difference of theses modes is the interaction force between the tip and the surface. In tapping mode, the contact is limited and protect the surface from damage. More details can be found in [62]. The AFM images in this work were acquired with the Veeco 3100 Dimension Atomic Force Microscope.

d) Secondary ion mass spectrometry (SIMS)

Secondary ion mass spectroscopy is a technique for determining the composition of solid surfaces or thin films by sputtering the surface of the sample with a focused primary ion beam and collecting and analyzing the ejected secondary ions. The mass-to-charge ratios of these secondary ions are measured with a mass spectrometer to determine the elemental, isotopic, or molecular composition [63]. SIMS is also used to detect low concentrations of atoms such as impurities or dopants.

In this work, SIMS was used to determine the boron content in the boron containing III-nitrides such as BGaN/GaN SLs and BAlN samples. To estimate the Mg concentration in the h-BN SIMS analyzes were used. For this purpose, calibration was first performed using Mg implantation in h-BN before analyzing the Mg-doped h-BN samples. The SIMS measurements in this work were performed by an external company Probion Analysis [64].

e) Scanning transmission electron microscope (STEM)

The scanning transmission electron microscope was used to determine the crystallographic properties of the grown BN samples. STEM is a type of transmission electron microscope (TEM) that has very thin specimen in order of 0.05 to 0.2 nm size. The electron beam is transmitted through the specimen. From the interaction between the electron and specimen, an image is formed [65,66]. To prepare the samples for STEM characterization, 100 nm of carbon was deposited to protect the surface. Then, all thin foils were prepared using focused ion beam (FIB) thinning and ionmilling by Dr. David Troadec at Institut d'Electronique de Microelectronique et de Nanotechnologie (IEMN, Lille, France). The carbon coating and HAADF-STEM characterization in this work were performed by Dr. Gilles Partriarche at the Centre de Nanosciences et de

Nanotechnologies (C2N). The equipment used for HAADF- STEM is an aberration corrected JEOL 2200FS electron transmission microscope.

2.3 Electrical characterization tools (probe station, Hall effect measurement)

a) Probe station

For electrical characterization, such as I-V characteristics at various temperatures, real-time measurements, C-V measurements, were made using the probe station shown in Figure 2-11. This equipment can be used under vacuum to avoid any oxidation during measurements at low and high temperatures.

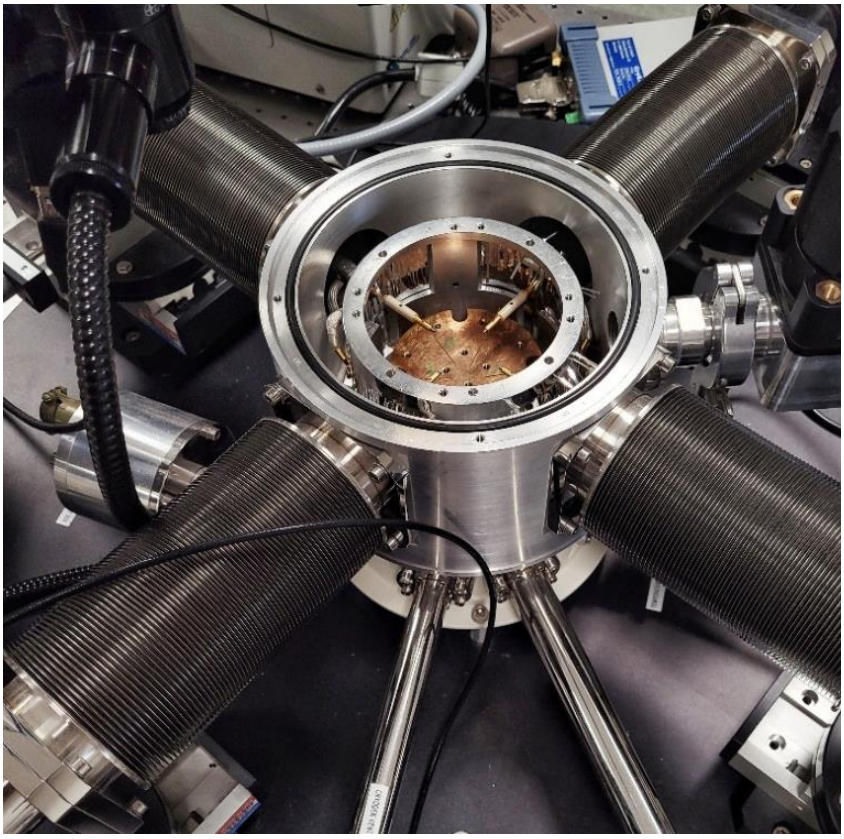

Figure 2-11: Photograph of the probe station used for electrical characterization

b) Hall effect measurement

To determine the nature of conductivity of Mg-doped samples, electrical measurements such as Hall measurement and Van der Pauw resistivity measurement were used. In the resistivity

measurement, a current is applied using four small contacts around the circumference of a flat, arbitrarily shaped and uniformly thick sample and then the voltage is measured. The carrier mobility was determined by measuring the Hall voltage (VH), resistivity and thickness of the sample. To measure the Hall voltage, a magnetic field is applied perpendicular to the sample in both directions (top and bottom) and a current is passed through the sample. This method helps us to determine properties such as conductivity type, carrier mobility and carrier concentration of Mg-doped h-BN.

CHAPTER 3: MOVPE GROWTH OF B-CONTAINING III-NITRIDE MATERIALS

This chapter discusses MOVPE growth studies of boron-containing III-N. The boron content in these alloys is an important parameter for neutron detector applications. Previously, our group developed BAlN/AlN and BGaN/GaN superlattice structures with nominal boron contents of about 12% in BAlN and 3.6% in BGaN [1-2]. These superlattice structures were used to demonstrate UV VCSELs and gas sensors, respectively. In the continuity of these studies, we have explored BGaN/GaN superlattices for neutron detection. The boron composition should be as high as possible to achieve effective absorption of thermal neutrons. We experimentally studied the growth of boron-rich BAlN. Then we performed the growth of 2.5 µm thick natural and enriched ^{10}B BN on sapphire.

1. BGaN growth

1.1 BGaN/GaN superlattices

We have developed BGaN/GaN superlattice structures with a nominal boron content of about 3% in BGaN. The BGaN/GaN SLs structures were grown using MOVPE in a T-shaped reactor at 1000 °C (presented in chapter 2). The growth was carried out under 100% nitrogen as carrier gas and TMG, TEB and NH3 as source of gallium, boron and nitrogen, respectively. A n-type doped GaN Standard Template (STN) was used for this study. Details of the growth conditions, boron incorporation and morphology of the films are described in previous work [3,4]. The BGaN/GaN superlattice structures consisting of 20 nm thick BGaN and 20 nm thick GaN repeated 11 times were grown and shown in Figure 3-1a.

The grown samples were optically transparent with no particles/defects on the surface, as shown in Figure 3-1b. The grown SLs sample exhibited a granular morphology (Figure 3-1c), but was smooth enough to fabricate devices compared to bulk BGaN.

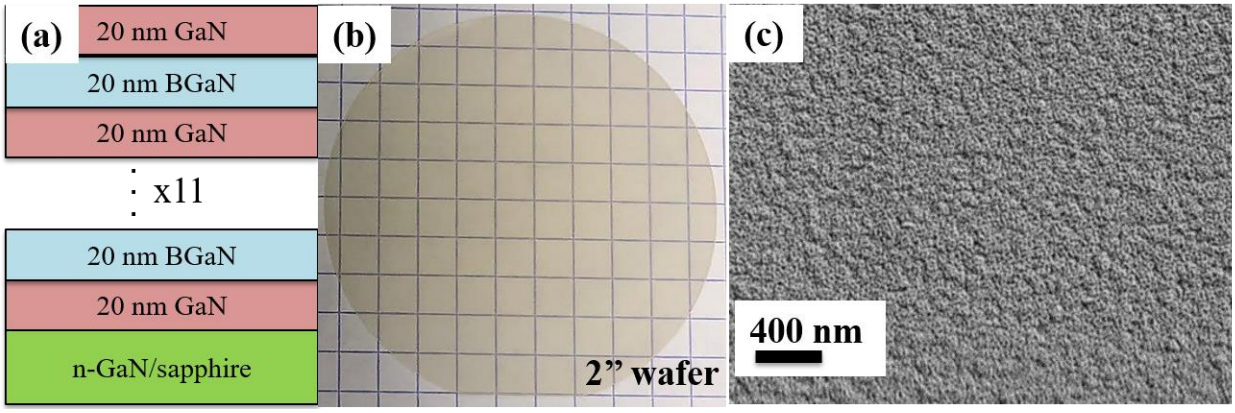

Figure 3-1: (a) Designed BGaN/GaN superlattice structure (b) Photograph of the as grown sample and (c) SEM images of BGaN/GaN superlattice structure.

The structural properties of the SLs structure on STN were analyzed by high resolution X-ray diffraction (HRXRD) using the 2θ-ω configuration. The scans are shown in Figure 3-2 with the simulation to estimate the boron content and thickness of the BGaN/GaN period. One can observe the intense GaN peak and the satellite peaks corresponding to the BGaN superlattices indicating good periodicity. In the HRXRD scan, the satellite peaks are not well pronounced, which could be related to the boron accumulation at the surface of the BGaN layer leading to rougher interfaces. From the simulation, the total thickness of the BGaN/GaN layer is 38 ± 2 nm with a boron content of 2.8%, which is later compared with the analytical data from SIMS.

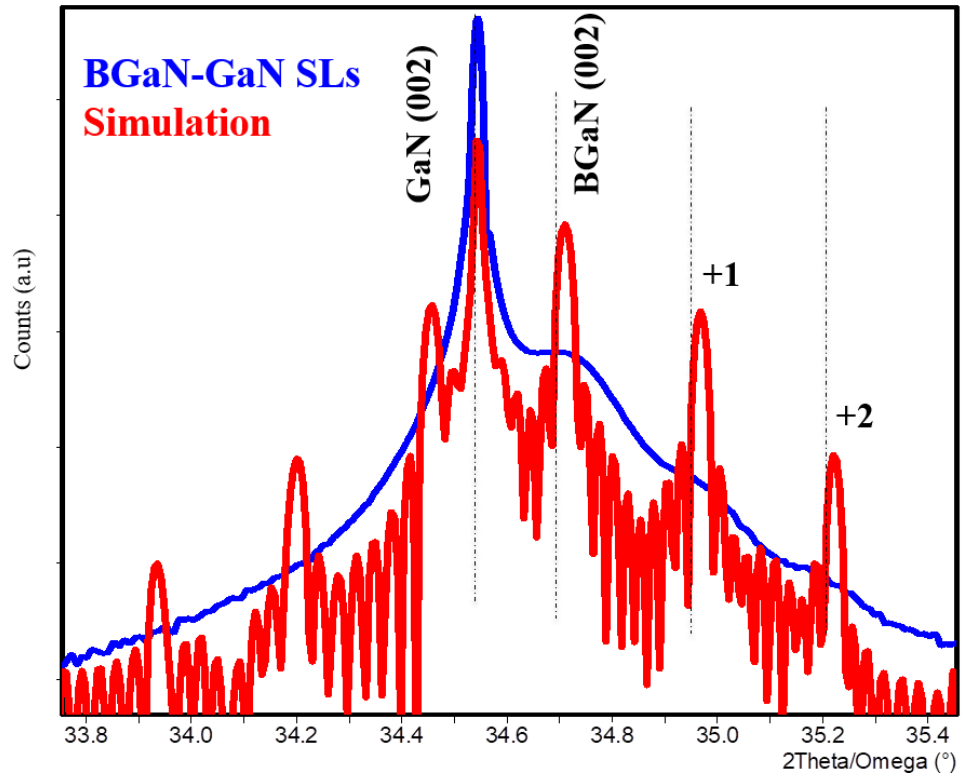

Figure 3-2. HRXRD 2θ-ω scans of the as-grown BGaN/GaN long period superlattice structure on STN templates.

We used BGaN/GaN SLs with 20 nm BGaN to regrow p-GaN to form PIN device structures.

1.2 PIN structures of p-GaN/BGaN/GaN SLs/n-GaN

P-GaN regrowth on the BGaN/GaN SLs using MOVPE in an Aixtron close coupled showerhead (CCS) 3 × 2″ reactor. The 300 nm GaN layers were grown at 1220 °C in hydrogen ambient at 85 mbar. Biscyclopentadienyl-magnesium (Cp2Mg) was used as the source of Mg doping. Mg activation was performed at 1010 °C during 20 min. The morphology was characterized by SEM shown in Figure 3-3b. SEM image reveals smooth surface without any particles/defects on the surface. We can observe in Figure 3-3c, the diffraction peak of the p-GaN layer in addition to the GaN and BGaN related peaks discussed in last section. These results confirm the successful growth of the full PIN structure.

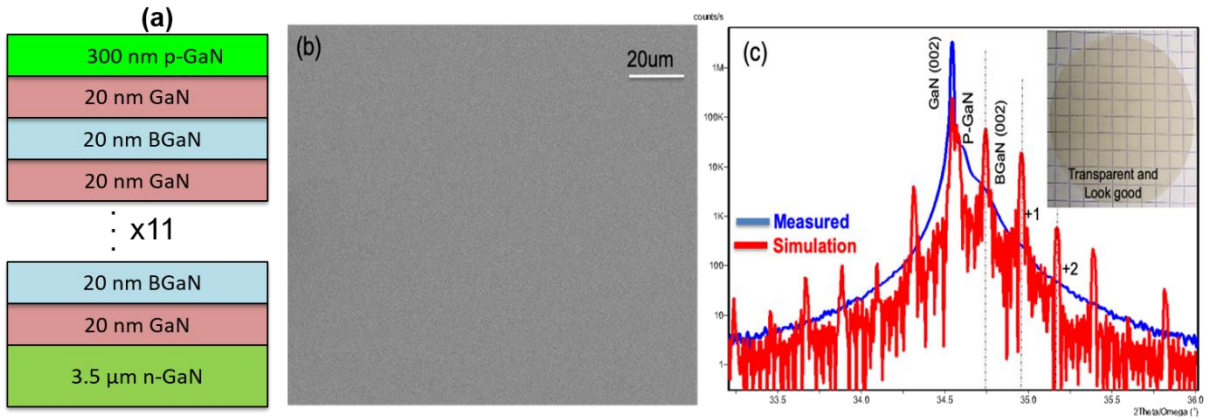

Figure 3-3: (a) Final device BGaN/GaN SLs based PIN device structure (b) SEM images of BGaN/GaN SLs based PIN device structure and (c) XRD of the PIN with the photograph of the as-grown sample in the inset.

The boron concentration in the BGaN layers was evaluated by SIMS profile. In Figure 3-4a shows the boron and gallium concentration as function of the layer depth. It can be observed that B profile varies anti-phase with Ga, which indicates that boron atoms substitute gallium atoms on the III sites of the lattice to form a ternary alloy. 11-period BGaN/GaN structure exhibits good uniformity. On the PIN structure (Figure 3-4b) the average magnesium (Mg) concentration in the p-GaN is $3x10^{19}$ atoms/cm^3 and the Si concentration is $2x10^{18}$ atoms/cm^3. In the active region (BGaN/GaN SLs), the dopant concentration (Mg, Si) is below the detection limit of the SIMS. However, Si spike is observed at the interface between p-GaN and BGaN/GaN SLs. This is due to surface contamination before the regrowth of p-GaN. The boron content is 2.8 % with 37 ± 3 nm total thickness of BGaN/GaN layer, which are in good agreement with the XRD data.

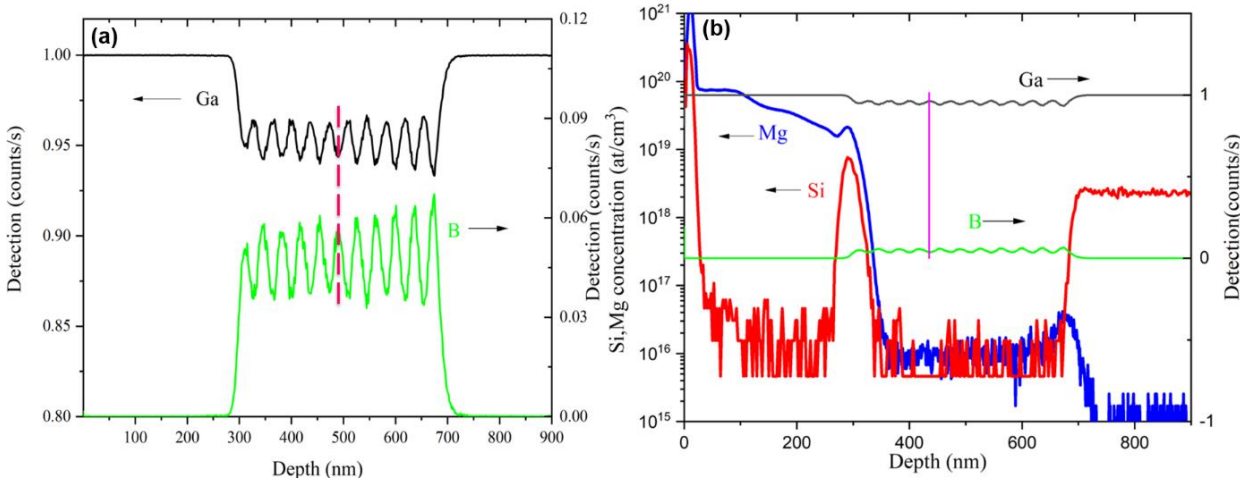

Figure 3-4: (a) B profile varies anti-phase with Ga, (b) SIMS data of PIN BGaN/GaN SLs

The grown BGaN/GaN SLs and the PIN BGaN/GaN SLs will be used to fabricate MSM and PIN devices for UV and neutron detection.

2. Growth of thick natural BN

Previously, our group conducted in-depth studies on the growth of 1 to 2.5 µm thick BN films at wafer scale. These BN films of 2.5 µm were used to demonstrate the prototype UV photodetector [5]. It was reported that the BN films showed strong absorption below 215 nm and small absorption peaks at 288 nm and 299 nm from native defects. The photodetector showed low dark current values and photoconductivity of about 100 ± 20% under deep UV illumination at 205 nm. Based on these interesting results, we have explored the same thickness of BN films for thermal neutron detection.

In the present work, we have grown a series of samples with 2.5 µm thick BN on sapphire substrates by metal organic vapor phase epitaxy (MOVPE) in a 3×2" Aixtron system (CCS) reactor, based on our previous work [5]. Triethylboron (TEB) and ammonia (NH3) were used as precursors for boron and nitrogen. Growths were performed at 1280 °C in a hydrogen environment at 90 mbar. The TEB flow rate was 60 µmol/min. To grow thick BN films, a higher growth rate is

required. We used a low V/ III ratio of 52 to shorten the growth time. The growth rate estimated from in situ reflectance was up to 450 nm/h.

The growth of the BN layers was initiated with a TEB pre-flow of a few seconds. Structural characterization of the 2.5 µm thick BN layers was assessed by HRXRD 2θ - ω scan as shown in Figure 3-5a, in which a peak at 25.8° is associated with the (0002) planes of the BN. The surface morphology of the 2.5 µm thick BN layers is shown in Figure 3-5b. The image from SEM shows a granular morphology and no wrinkles on the surface. The sample was optically transparent (inset of Figure 3-5b).

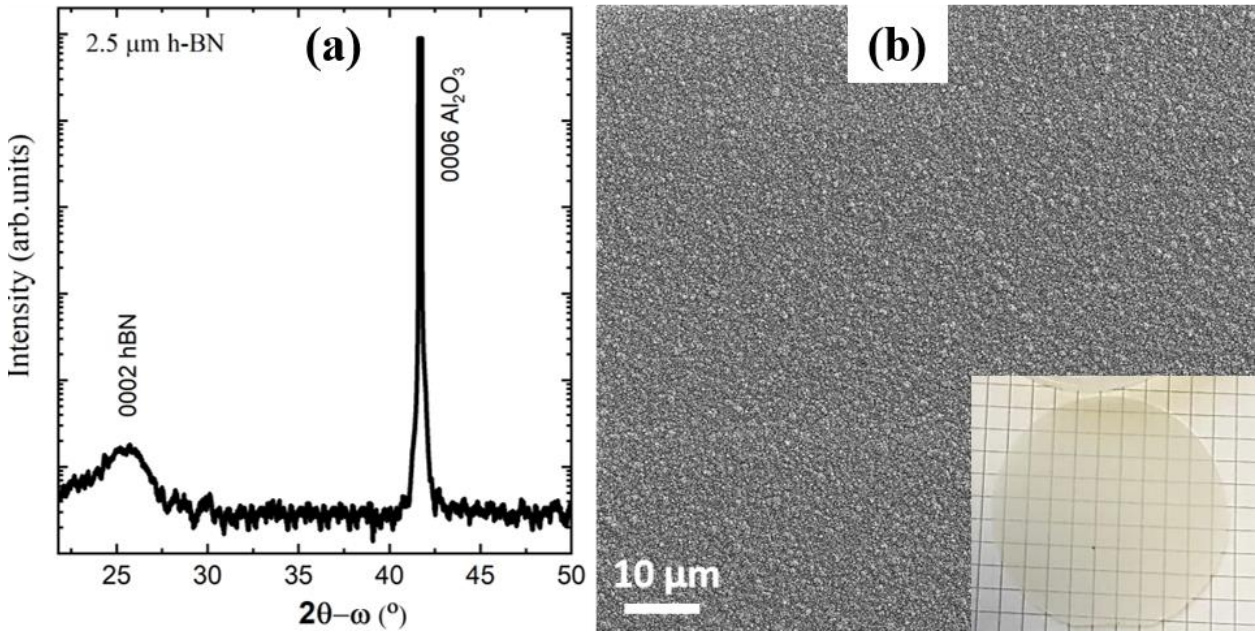

Figure 3-5: (a) and (b): High-resolution X-ray diffraction (HRXRD) 2θ-ω scan and SEM image of 2.5 µm thick BN layers, respectively. The inset shows photograph of the 2 inch produced layer.

The AFM characterization in Figure 3-6 shows the detailed morphology of the 2.5 µm thick BN sample. As can be seen in the figure SEM, the AFM measurement also reveals a granular morphology.

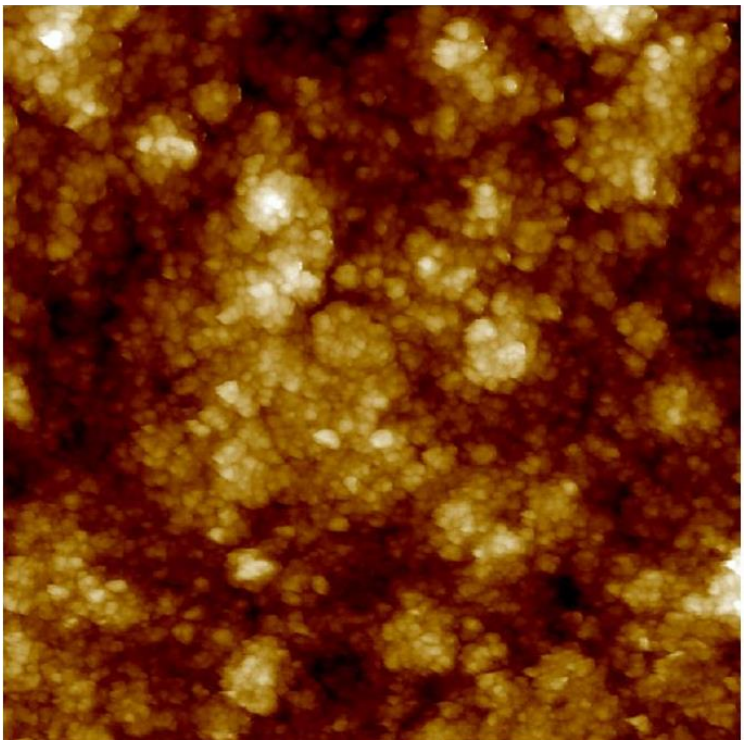

Figure 3-6: AFM image of the 2.5 µm thick h-BN layers (5x5µm scan area).

To elucidate the crystallographic properties of the grown thick BN, cross-sectional images were taken using scanning transmission electron microscope (STEM), which are shown in Figure 3-7. Under the conditions of high growth rate (450 nm/h), two-dimensional BN layers with thickness of 5~6 nm were formed at the interface between film and substrate. In the following 10~15 nm, stacking faults caused disorder of crystallographic planes, which hindered the growth of the uniform c-oriented film lattice. The fast Fourier pattern of the c-oriented region near the substrate (2D layered structure region) can be clearly identified as a hexagonal structure, as shown in the inset of Figure 3-7c. The following layer on the top part is turbostratic, where the BN layer plates are enclosed in short domains and irregularly oriented, losing their long-range order. This also explains the broadness of the sp2- BN peak in the XRD pattern in Figure 3-5a. The grains exhibit a nanofiber feature [6], as shown by the examples indicated by the white lines in Figure 3-7b. These "fibers" range in length from a few nanometers to tens of nanometers.

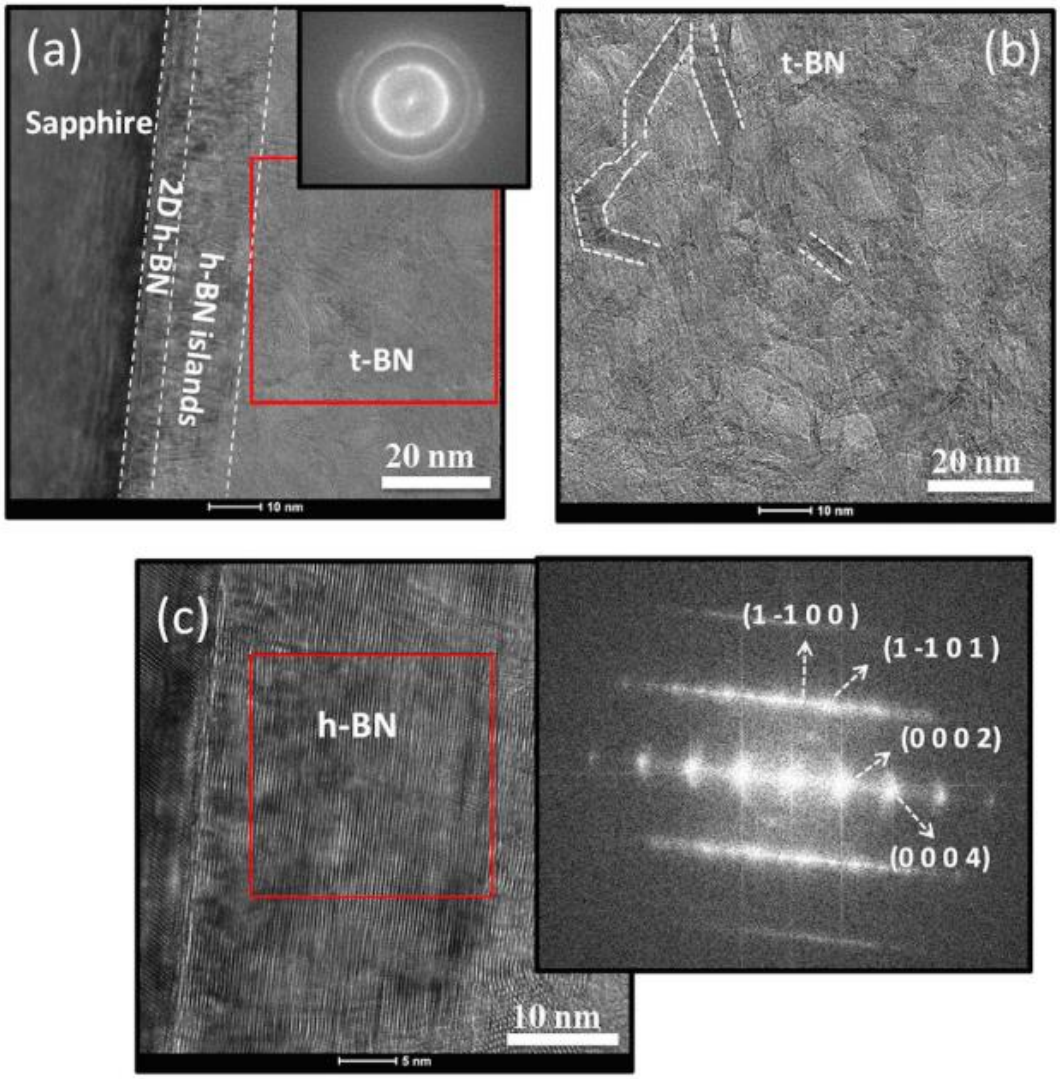

Figure 3-7: (a) STEM image of thick BN grown on sapphire substrate, which was taken along zone axis of <11-20>. Inset is the Fourier transform (FT) pattern for the selected area. (b) Higher magnification of the t-BN part showing randomly oriented BN nanofibers. (c) The initial layer near the substrate surface with the FT pattern in the inset confirming the hexagonal phase [5].

3. Growth of thick ^{10}B enriched BN films

Under the same growth conditions as those used to grow natural BN, we grew ^{10}B enriched BN layers by using TEB enriched in 97% of the isotope ^{10}B instead of TEB (20% of ^{10}B). Figure 3-8 shows the HRXRD scans of the ^{10}B enriched BN layers compared to the natural BN. It can be

observed that there is almost no difference in peak position and intensity. This shows that BN, grown with enriched ^{10}B in TEB precursor has no effect on the growth rate and material quality. Similar results were obtained with both precursors.

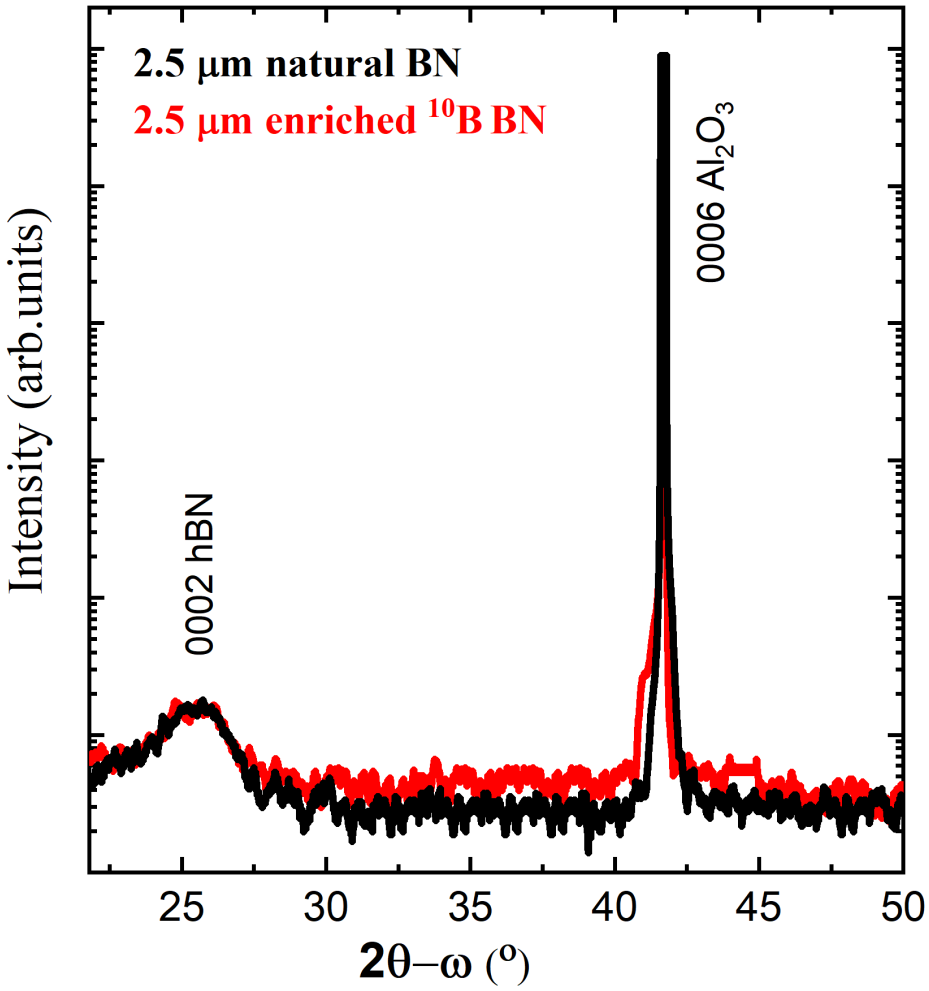

Figure 3-8: HRXRD 2θ-ω scan of 2.5 µm thick natural and ^{10}B enriched BN layers.

To confirm the concentration of the ^{10}B isotope, an SIMS analysis of the grown samples was performed (see Figure 3-9). The ratio $^{10}B/^{11}B$ is 36 which correspond 97 % of ^{10}B in the BN confirming the successful growth of ^{10}B enriched BN layers.

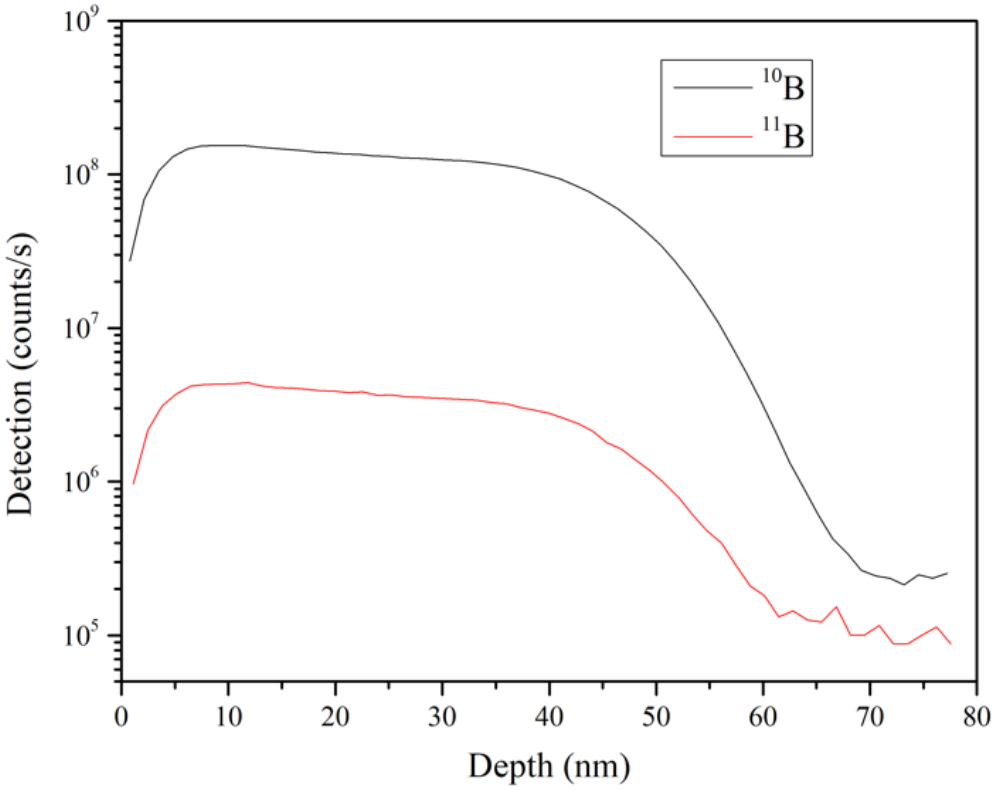

Figure 3-9: SIMS profile of the ^{10}B and ^{11}B detection in the ^{10}B enriched BN layers.

In summary, we have demonstrated wafer-scale growth of boron-containing III -N materials using MOVPE growth systems on a 2-inch sapphire substrate. BGaN/GaN SLs with 2.8% boron and 440 nm total thickness were grown. SIMS data showed antiphase variation between boron and gallium profiles, indicating the formation of a ternary BGaN alloy. We used two precursors (TEB and enriched ^{10}B TEB) to grow 2.5 µm thick natural and ^{10}B enriched BN films. SIMS analysis confirmed the presence of 97% ^{10}B in the BN films. The enriched precursor did not affect the morphological and structural quality of the ^{10}B enriched BN films.

The BGaN/GaN SLs, the natural BN and the ^{10}B enriched BN samples were used to fabricate neutron detection devices.

CHAPTER 4: DEVICE FABRICATIONS AND ELECTRICAL CHARACTERIZATION

This chapter focuses on the processing and electrical characterization of the BN and BGaN/GaN SLs based detectors. First, metal-semiconductor-metal (MSM) detectors based on Ti/Au and Ni/Au interdigitated structures are fabricated using a 2.5 µm thick BN layer with natural and enriched ^{10}B. These devices are tested in the dark and under UV light. Subsequently, MSM and PIN devices made of BGaN/GaN SLs are processed and electrically characterized. At the end of the chapter, the excess carrier transport mechanism, photocurrent and internal gain mechanism of the photodetector are explained.

1. Metal-semiconductor-metal devices of BN

1.1 Device processing

The BN samples are very fragile, so processing the devices is challenging. We first processed the BN samples using standard photolithography. For this process, liquid solvents such as acetone and isopropanol were used for cleaning, resulting in self-delamination of the BN samples, as shown in Figure 4-1. To solve this problem, we design a hard mask for contact deposition without the use of a liquid.

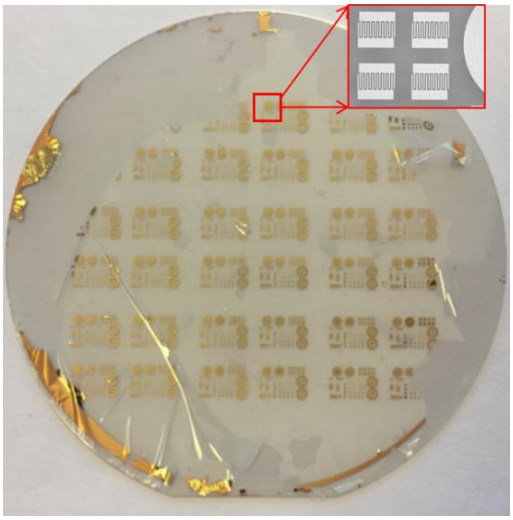

Figure 4-1: Photograph of BN wafer after processing using standard photolithography.

In the literature, different metal contacts such as Ni/Au, Ti/Au are used to form ohmic or Schottky contacts depending on the fabrication process [1]. The electrical contacts consist of interdigital fingers with a width of 200 µm and spacing of 200 µm and were fabricated with either Ni/ Au-Ni /Au bilayer (30 nm/100 nm) or Ti/ Au-Ti /Au bilayer (30 nm/100 nm) deposited by thermal evaporation over a hard mask. The samples were not annealed after deposition of the contacts. To prevent delamination of the h-BN samples during device fabrication, liquid cleaning was avoided. The surface area of the detectors is 1x1 cm2. Figure 4-2(a) shows a picture of the fabricated MSM devices.

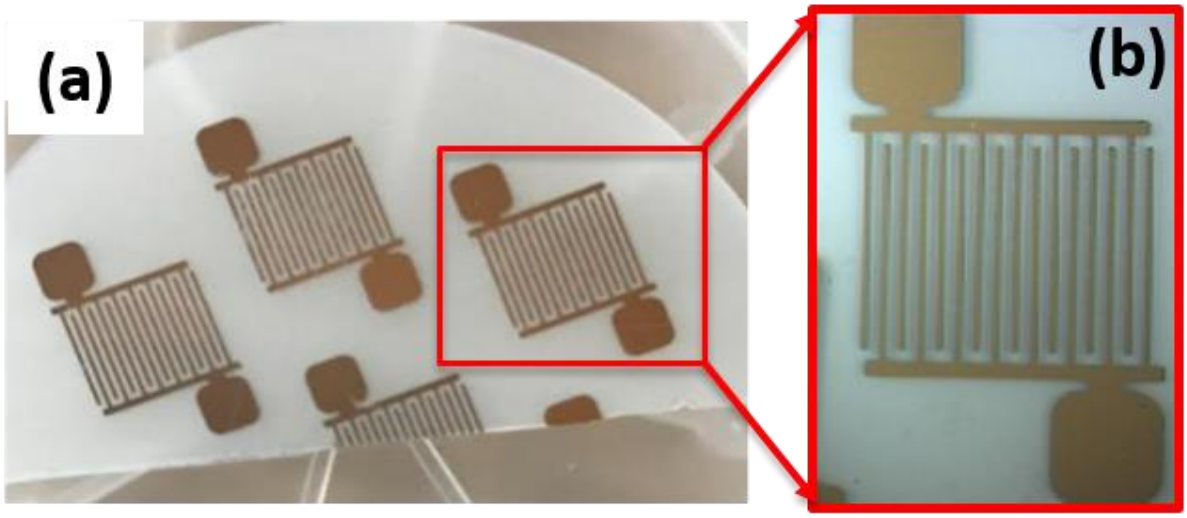

Figure 4-2: (a) Photograph of the MSM h-BN devices, (b) zoom of the MSM device.

1.2 Dark current characteristic

Figure 4-3 shows the I-V characteristics of the two MSM (Ni/ Au-Ni /Au) and (Ti/ Au-Ti /Au) devices for an applied voltage in the range of -200 V to 200 V, recorded in the dark. Since the work function of Ti is lower than that of Ni, the Schottky barrier height (SBH) formed at the Ti/h-BN interface is higher than that formed with Ni. Therefore, as expected, the current flowing in the

MSM with Ti contact is lower than the current flowing in the MSM with Ni contact. In fact, the current measured at +/- 200 V in the MSM with Ni contact is about 12 pA, which is five times higher than the current measured in the MSM with Ti contact under the same conditions. Even more interesting is that despite the same metallic nature of the two contacts, both I-V curves show a slightly asymmetric behavior with respect to the applied voltage, as can be seen in Figure 4-3. This asymmetric behavior most likely stems from a different density of filled carrier traps at the interface of the h-BN with the two contacts [2], resulting in a different SBH at the two contacts.

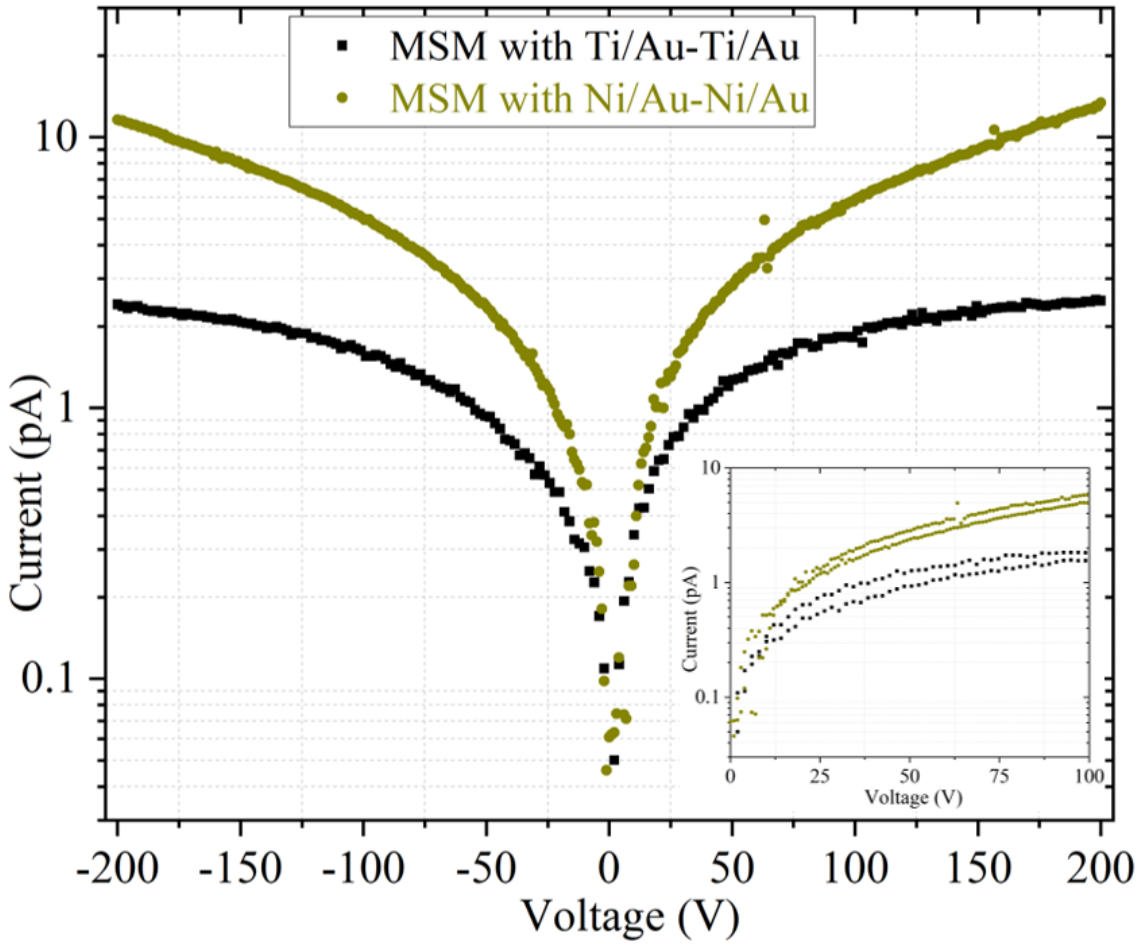

Figure 4-3: Dark current of the 2.5-µm thick natural h-BN MSM detectors with two different Schottky contacts (Ni/Au-Ni/Au and Ti/Au-Ti/Au). Inset shows the corresponding I-|V| curves to highlight the asymmetric behavior.

1.3 Response of the MSM h-BN devices under UV light

Prior to the neutron test, the key parameter mobility-lifetime product (μτ) was determined from the measured photocurrent under a UV lamp (λ=390-440nm) with a power density of 140 mW/cm^2 and a light spot area of 1 cm^2 covering the entire MSM h-BN detector (1 cm^2 area). This parameter is indicative of the electronic quality and effectiveness of the device used for neutron detection [3]. For detector applications, it is important to separate out the free electrons and holes produced by the radiation (UV illumination or nuclear reaction) in time. To ensure that most of the generated charge carriers are collected, the recombination time (τ) must be larger than the transit time (t). This means that the product is $\mu\tau \geq L^2/V$ ($t=L^2/\mu V$), where V is the bias voltage and L is the distance between the two electrodes (inset in Figure 5-4). The μτ product is affected by the crystalline quality of the grown materials (density of impurities/defects) and the device fabrication processes. To determine the product of mobility and lifetime, the MSM BN device was irradiated with a UV lamp. The photogenerated current was fitted using the well-known equations of Many [4] to determine the value of μτ (see Figure 4-4).

$$I_{ph} = I_o \frac{\mu\tau V}{L^2}\left[1 - \frac{\mu\tau V}{L^2}\left(1 - exp\left(-\frac{L^2}{\mu\tau V}\right)\right)\right] \quad (1)$$

Where I_{ph} is the photogenerated current and I_o is a constant term that includes the reflection coefficient at the interface, the excitation flux, and geometric considerations. The fitted value of μτ is 3.85×10^{-5} cm^2/V. This value is an order of magnitude higher than the reported value of the μτ-product (5.4×10^{-6} cm^2/V for 4.5 μm thick BN) [5]. This value of the μτ-product is well above the minimum values for a good detector reported in reference [3], indicating that our BN MSM devices are good enough to be used for thermal neutron detection.

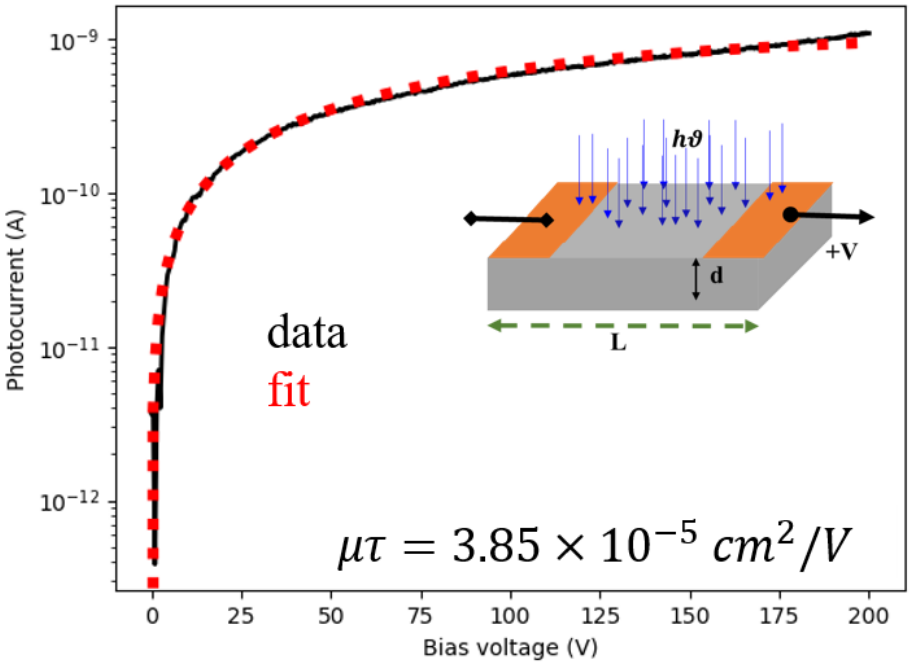

Figure 4-4: Photocurrent-voltage characteristics of MSM h-BN device measured under UV radiation.

2. MSM device of BGaN/GaN SLs

2.1 Device fabrication

Metal-semiconductor-metal (MSM) devices were fabricated on the grown structures mentioned in Chapter 3. The BGaN/GaN SLs structures need to be fully processed to fabricate lateral and vertical prototypes. First, lateral MSM devices were fabricated on BGaN/GaN superlattice structures with platinum (Pt) metal contacts, as shown in Figure 4-5. We investigated two metal contacts: Pt and gold (Au). The Pt metal contact was chosen because of its higher sensitivity. The steps of the process:

(i) Cleaning of the wafer with acetone and isopropanol, followed by a dilute hydrochloric acid solution to remove organic residues and oxides.

(ii) The sample was patterned using standard photolithography.

(iii) The 2-inch wafer was cut into two pieces.

(iv) On one half of the wafer, 100 nm Pt was deposited by sputtering.

(v) The metal was lifted off in a heated dimethyl sulfoxide (DMSO) solution, which was stirred for about 1 hour.

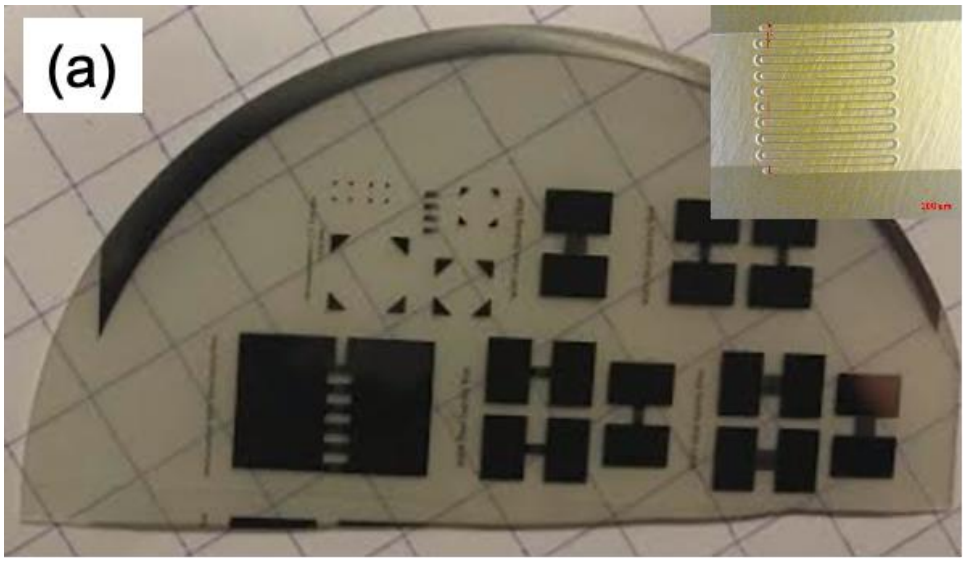

Figure 4-5: Final double Schottky MSM device prototype fabricated on BGaN/GaN SLs structure with Pt as metal contact.

2.2 Response to UV light

Although the surface of the superlattice samples is rough, stable metal contact patterns were obtained without any degradation/detachment. The electrical properties of these devices were investigated using a probe station in the dark and under UV illumination. Figure 4-6 shows the I-V characteristics under UV light compared to the I-V characteristics in the dark. The measurements show a double Schottky behavior, confirming the formation of the MSM devices. The dark current of the MSM BGaN/GaN with Pt contact is 1.40 µA at a bias voltage of 10 V. Under a UV lamp, the photocurrent is ~100 µA at 10 V, which is two orders of magnitude higher than the dark current and shows high sensitivity to UV light. This excellent photoreaction indicates that this device configuration can be good UV photodetectors and neutron detectors.

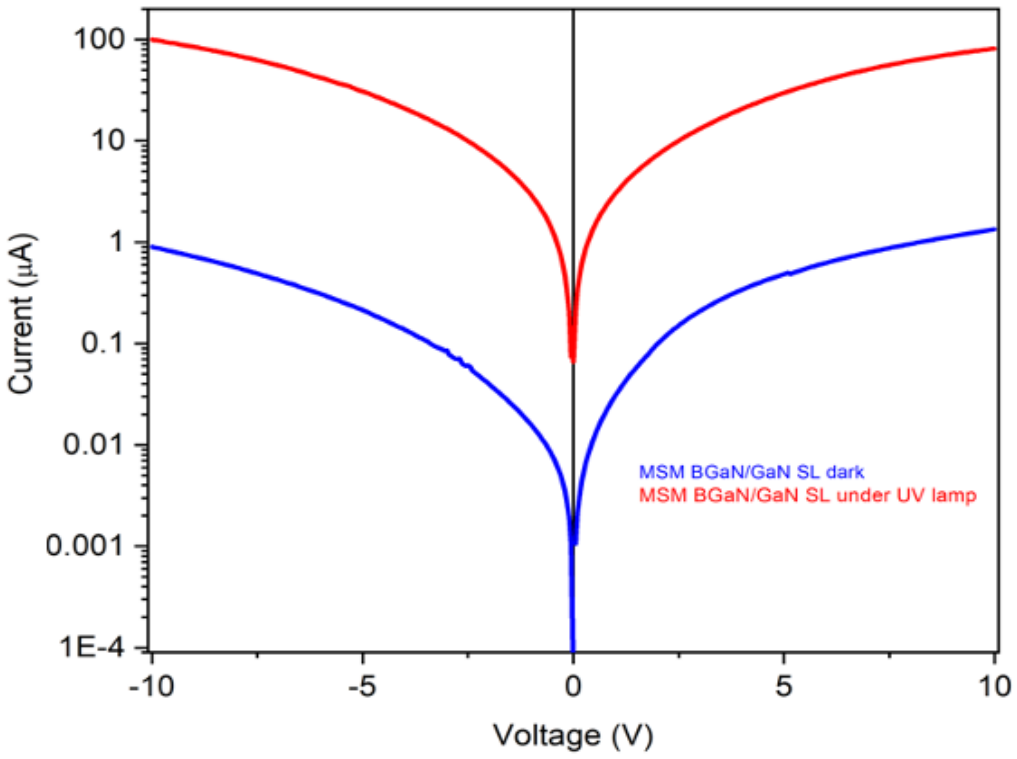

Figure 4-6: I-V characteristics of BGaN/GaN double Schottky MSM device prototype under dark and UV light irradiation.

3. PIN junction of BGaN/GaN SLs

3.1 Device fabrication

A standard photolithography-based process was used to fabricate the PIN BGaN/GaN SLs device. First, mesa etch isolation was achieved by inductively coupled plasma with $BCl_3/Cl_2/Ar$ chemistry. Standard stacks of Ti/Al/Ni/Au and Ni/Au were used for the n-contact and p-contact, respectively. All metal layers were deposited by thermal evaporation. The n-contact was annealed at 850 °C for 30 s under N_2. The p-contact was annealed at 600 °C for 60s under an O_2/N_2 atmosphere, as shown in Figure 4-7.

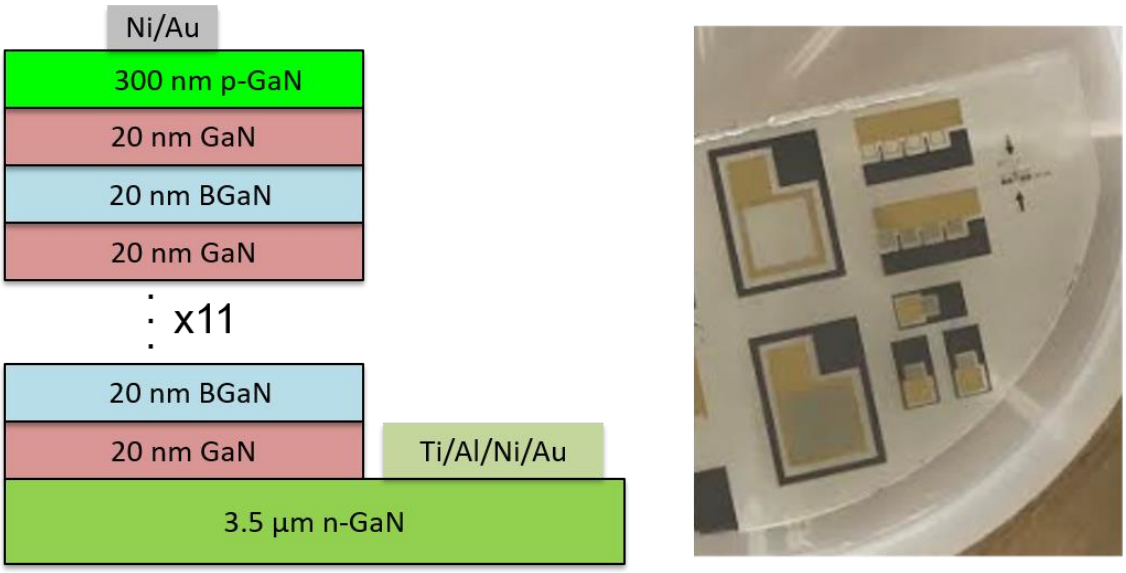

Figure 4-7: PIN device structure after process.

3.2 Dark characteristics

Figure 5-8 shows the measurements of the electrical current-voltage (I-V) characteristics in the dark to evaluate the electrical properties of the fabricated PIN structure of BGaN/GaN SL devices. Remarkably, the current of the device was 4 orders of magnitude higher at forward bias than at reverse bias, which is a typical rectifying I-V curve. At reverse bias, the leakage current is about 2 µA at -2 V, but it was not saturated as would be expected for an ideal diode, and it continued to increase with reverse voltage. This suggests that there are leakage current paths related to the deep defect levels in the depletion layer [6].

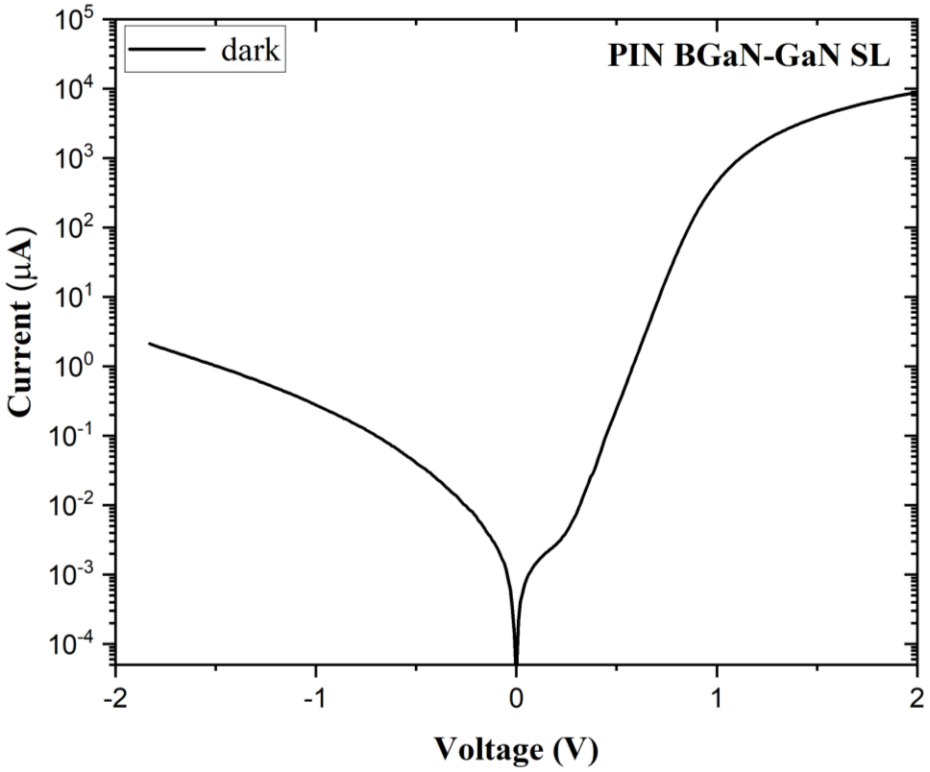

Figure 4-8: I-V characteristics of BGaN/GaN SLs PIN structure under dark.

4. Transport mechanism of charge carriers

In a solid-state neutron detector, a nuclear reaction is produced when an incoming neutron is absorbed by the nuclei of matter. The daughter particles of the nuclear reaction penetrate the matter and lose their kinetic energy to produce a cloud of electron-hole pairs. Subsequently, the electron-hole pairs are driven to the electrodes by an electric field to produce an electric signal. This behavior also occurs in photodetectors, where charge carriers are generated by the absorption of an excited photon. The collection of charge carriers follows the same principles in the two types of devices - neutron detectors and photodetectors. We would like to recall here some basic principles of photoconductors in order to prepare the analysis of the response of neutron detectors, their I-V characteristics and eventual gain mechanism.

4.1 Current generation in photoconductors (PC)

When a photon with an energy $h\nu \geq E_g$ is absorbed by a semiconductor, an electron-hole pair is created, as shown in Figure 4-9. The electron-hole pairs produced contribute to an increase in conductivity that can be detected in an external circuit. The electron-hole pairs can recombine or be trapped within the semiconductor. Detailed information on recombination and traps can be found elsewhere [7].

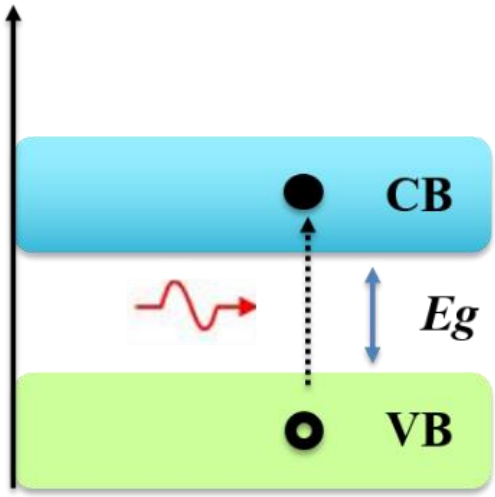

Figure 4-9: Electron-hole pair generation.

The current density can be determined from the electric charge of the charge carriers (q), the electric field (E), the electron mobility (μ_e), the hole mobility (μ_h), the density of electrons in the conduction band (Δn) and the density of holes in the valence band (Δp). The current density is given as follows [8]:

$$J = q(\mu_e \Delta n + \mu_h \Delta p) \times E \tag{2}$$

Where q is the electron charge, μ_e (μ_h) is the electron (hole) mobility, Δn (Δp) is the excess carrier concentration, and E is the applied electric field. By solving the continuity equation, we can determine the excess carrier distribution, photocurrent and the photo-gain. The continuity equation

is very helpful in understanding the physics that governs the generation-recombination process in photoconductors. The continuity equation for electrons under stationary conditions is given by [9]:

$$D_n \frac{\partial^2 \Delta n}{\partial x^2} + \mu_n E \frac{\partial \Delta n}{\partial x} + \mu_n \Delta n \frac{\partial E}{\partial x} - \frac{\Delta n}{\tau_n} + g_n = 0. \quad (3)$$

Where D_n (cm^2s^{-1}), τ_n (s), and g_n ($cm^{-3}s^{-1}$) are the diffusion constant, electron lifetime and generation rate respectively.

In this study, we assume that the electric field is uniform. Therefore, the resulting expression of the continuity equation reduces to:

$$D_n \frac{\partial^2 \Delta n}{\partial x^2} + \mu_n E \frac{\partial \Delta n}{\partial x} - \frac{\Delta n}{\tau_n} + g_n = 0. \quad (4)$$

To determine the distribution of excess carrier density, we need to solve equation 4.

a) General case (nonuniform illumination)

In this section, the illumination of the semiconductor slab is not uniform (Figure 5-10), resulting in a gradient of excess charge carriers.

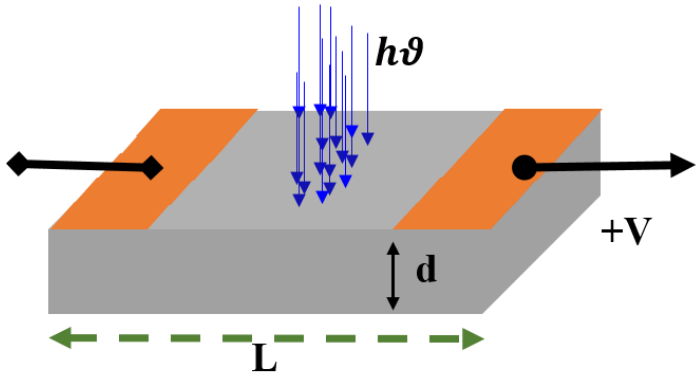

Figure 5-10: Simple photoconductor structure under nonuniform illumination.

Therefore, the variation of carrier concentration with respect to the x-axis is not zero and the equation for excess carrier continuity (4) is:

$$g - \frac{\Delta n}{\tau_n} - \mu_n E \frac{d\Delta n}{dx} = 0 \tag{5}$$

Where g is the generation rate per volume and per second, which is expressed as [9]

$$g = \eta \frac{1}{S \times L} \frac{P}{h\nu} \text{ and } \eta = (1 - R)(1 - e^{-\alpha d}) \tag{6}$$

Where η is the quantum efficiency, S is the area, L is the distance between two electrons, R is the reflection coefficient and α is the absorption coefficient and P is optical power.

After calculation, the solution of equation 5 is given by:

$$\Delta n(x) = \tau_n g \left[1 - \exp\left(-\frac{x}{\mu_n E \tau_n}\right)\right] \tag{7}$$

The induced photocurrent for the electrons is expressed as:

$$I_{phn} = S \times q\mu_n E \times \frac{1}{L} \int_0^L \Delta n \, dx \tag{8}$$

After integration and terms arrangements of equation 8, we obtain:

$$I_{phn} = \eta \frac{P}{h\nu} q\tau_n \frac{\mu_n V}{L^2} \left[1 - \tau_n \frac{\mu_n V}{L^2} \left(1 - \exp\left(-\frac{L^2}{\mu_n \tau_n V}\right)\right)\right] \tag{9}$$

Idem for the holes:

$$I_{phh} = \eta \frac{P}{h\nu} q\tau_h \frac{\mu_h V}{L^2} \left[1 - \tau_h \frac{\mu_h V}{L^2} \left(1 - \exp\left(-\frac{L^2}{\mu_h \tau_h V}\right)\right)\right] \tag{10}$$

Then, the total photocurrent generated in the semiconductor under non-uniform illumination is given by:

$$I_{ph} = I_{phn} + I_{phh}$$

$$I_{ph} = \eta \frac{P}{h\nu} q \left[\frac{\mu_n \tau_n}{L^2} + \frac{\mu_h \tau_h}{L^2}\right] V - \eta \frac{P}{h\nu} q[(\mu_n \tau_n)^2 + (\mu_h \tau_h)^2] \frac{V^2}{L^4} +$$
$$\eta \frac{P}{h\nu} q \left[(\mu_n \tau_n)^2 \left(\exp\left(-\frac{L^2}{\mu_n \tau_n V}\right)\right) + (\mu_h \tau_h)^2 \left(\exp\left(-\frac{L^2}{\mu_h \tau_h V}\right)\right)\right] \frac{V^2}{L^4} \quad (11)$$

Plotting equation 11 in Figure 4-11, we observe that the total photocurrent saturated at certain value, which corresponds to the maximum current generated without any gain in the device (G=1).

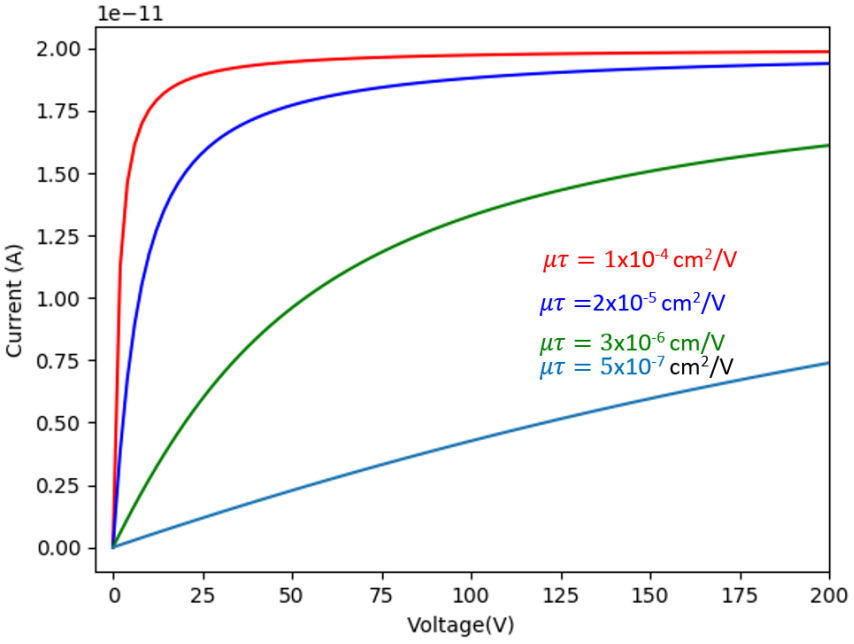

Figure 4-11: Photocurrent of the photoconductor under non-uniform illumination respect to bias voltage.

b) Particular case (uniform illumination)

With uniform illumination, the excess carrier is uniformly distributed and implies that the first and second parts of Equation 3 are zero. Therefore, equation 11 becomes:

$$I_{ph} = I_{phn} + I_{phh} = \eta \frac{P}{h\nu} q \tau_n \mu_n (1 + \frac{\mu_p}{\mu_n}) \frac{V}{L^2} \quad (12)$$

This current has a linear behavior with respect to the bias voltage. The photoconductive gain for both holes and electrons is defined as:

$$G = \frac{\tau_n}{t}\left(1 + \frac{\mu_p}{\mu_n}\right) \tag{13}$$

From this relationship (Equation 13), it follows that a high gain can be obtained with shorter transit time and longer lifetime (τ_n). The physical explanation for the gain is that the shorter transit time allows the photogenerated carriers to circulate several times in the circuit before recombining. This results in many times more photoexcited charge carriers being generated to ensure charge neutrality [9].

Let us assume that the product of mobility and lifetime of electrons and holes are the same. In Figure 4-12, we plotted the photocurrent as a function of bias voltage with different mobility-lifetime products (from 5×10^{-7} to 1×10^{-4} cm^2/V). This plot confirms the linear behavior of the photocurrent produced under uniform illumination and uniform distribution of excess carriers.

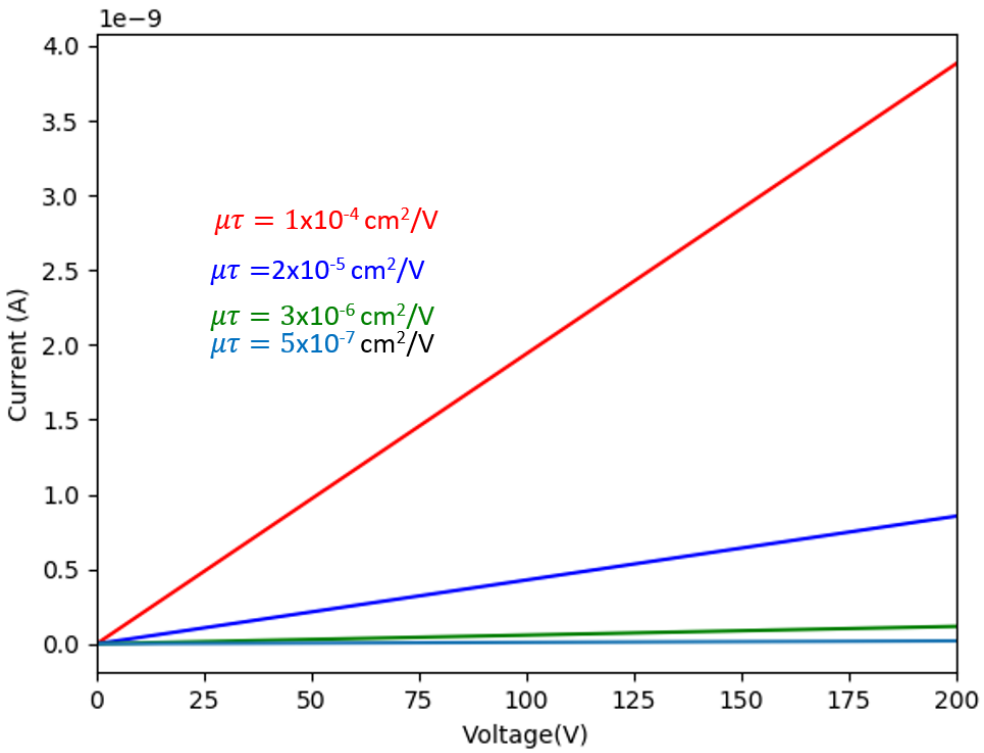

Figure 4-12: Photocurrent of the photoconductor under uniform illumination respect to bias voltage.

4.2 Photoconductor with Schottky contacts

Two different types of contacts are required for the Schottky diode, for example, a resistive contact and a Schottky contact. However, identical Schottky contacts are required for the double Schottky to form an MSM Schottky detector. Under illumination, the Schottky diode generates current at 0 V bias due to the internal electric field. The photogenerated charge carriers are free to move toward the electrode of the ohmic contact (no barrier height) and are collected to produce a net current at zero bias voltage.

In MSM (double Schottky) devices, there are two situations: (a) symmetrical Schottky contacts, no difference in Schottky barrier height (SBH) of the two electrodes, and (b) asymmetrical Schottky contacts.

a) Symmetric Schottky contacts at zero bias

The Symmetric Schottky contacts consist of two electrodes with metals M1/M1. In the case of interdigitated design, the distance between the fingers should be equal. As shown in Figure 4-13 for an n-type semiconductor, no photocurrent is generated when illuminated with a zero bias voltage [10-11]. This is due to the absence of an electric field and results in spontaneous recombination of the generated charge carriers.

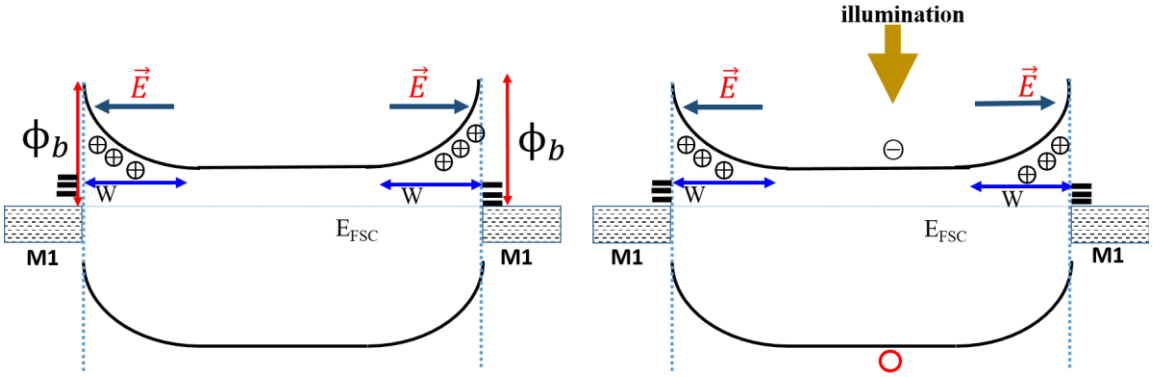

Figure 4-13: Symmetric double Schottky contacts under illumination at zero bias.

b) Asymmetric Schottky contacts at zero bias

Different technologies have been used to realize asymmetric Schottky contacts such as MSM with two different metals M1/M2, two identical metal contacts with special treatment (UV irradiation, thermal annealing, etc.), or different finger widths [12-16]. Regardless of where the asymmetry of barrier height in MSM devices comes from, an electric field is automatically generated. Under illumination, electron-hole pairs are created in the semiconductor and are immediately separated by the residual electric field, resulting in current flow (see Figure 4-14). This results in a net photocurrent generation in the asymmetric MSM device at zero bias voltage, as reported in UV MSM photodetectors [12-16].

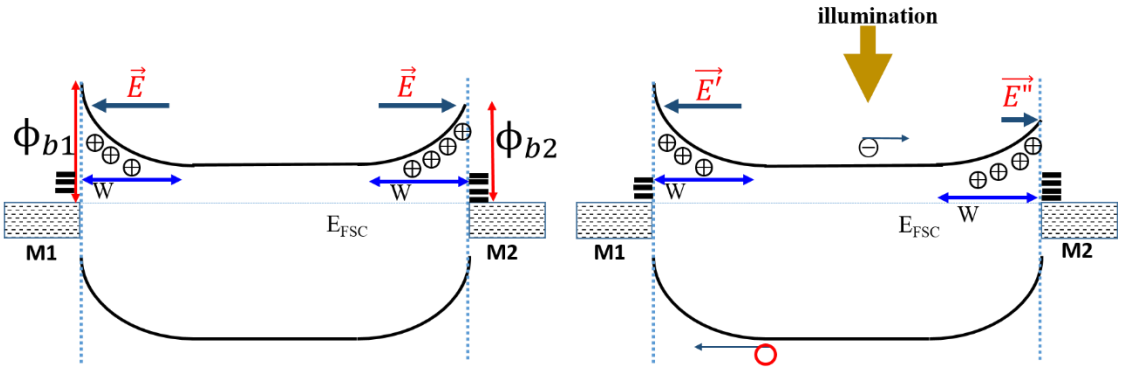

Figure 4-14: Asymmetric Schottky contacts, where the residual electric field is not zero.

c) MSM under bias voltage

Under forward bias voltage, the Schottky barrier decreases and an electric field between the Schottky contacts allows the photogenerated charge carriers to collect to produce a net photocurrent. The dark current in thermionic emission is given by:

$$I_d = A^* T^2 \exp\left(-\frac{q\phi_b}{kT}\right)\left[\exp\frac{qV}{nkT} - 1\right] \quad (14)$$

where A* is the theoretical Richardson constant, T is the temperature, n is the ideality factor, q the electron charge, kT is the thermal energy, and ϕ_b is the Schottky barrier height. In an illuminated Schottky detector, there are two mechanisms that contribute to the photo-response. The charge carriers generated by the illumination and the trapping of minority carriers at the semiconductor-metal interface. The trapping of carriers in the interface states leads to a decrease in the barrier height by a $\Delta\phi_b$. The second mechanism is responsible for the high enhancement of the current observed in the experimental results [17].

In summary, we processed and tested the MSM-based BN devices, the MSM-based BGaN/GaN SLs devices, and the PIN p-GaN/BGaN/GaN/n-GaN devices under the UV lamp. For the BN devices, the MSM with Ti/Au showed lower dark current than the MSM with Ni/Au

contacts. Both MSMs on BN were found to exhibit asymmetric behavior, which was attributed to a different density of filled carrier traps at the interface of the h- BN with the two contacts. The PIN BGaN/GaN SLs exhibited a diode-like I-V characteristic. We recalled the different properties of photoconductors with different configurations (ohmic, MSM-double Schottky) to analyze the neutron detection results.

CHAPTER 5: BORON BASED III-N NEUTRON DETECTION

In this chapter we report the results of neutron tests with the BN and BGaN/GaN-based detectors. We have investigated the neutron sensitivity using two different metal contacts (Ti/Au and Ni/Au) and have chosen the appropriate configuration for the comparison between MSM based on natural and ^{10}B enriched BN detectors. The real-time measurements under neutron irradiation on MSM and PIN BGaN/GaN are presented.

1. Neutron source and prototype neutron detection

Neutron irradiation of the devices was performed at Centre Etudes Nucléaires de Bordeaux-Gradignan (CENBG). The neutron source used for this study consists of a LiF/Cu target irradiated with a proton beam producing neutrons with an energy of 500 keV. Thermal neutrons were obtained using a 5 cm thick high-density polyethylene (HDPE) slab inserted between the detector and the target. As shown in Figure 5-1, the HDPE plate was placed at a distance of 1 cm from the target and the tested devices. The maximum resulting thermal neutron flux was $3x10^4$ $n/cm^2/s$ with neutron energy below 1 eV. The current-voltage (I-V) values of the various devices were recorded at room temperature before, during and after neutron irradiation using a Keithley 2636B source-measure unit.

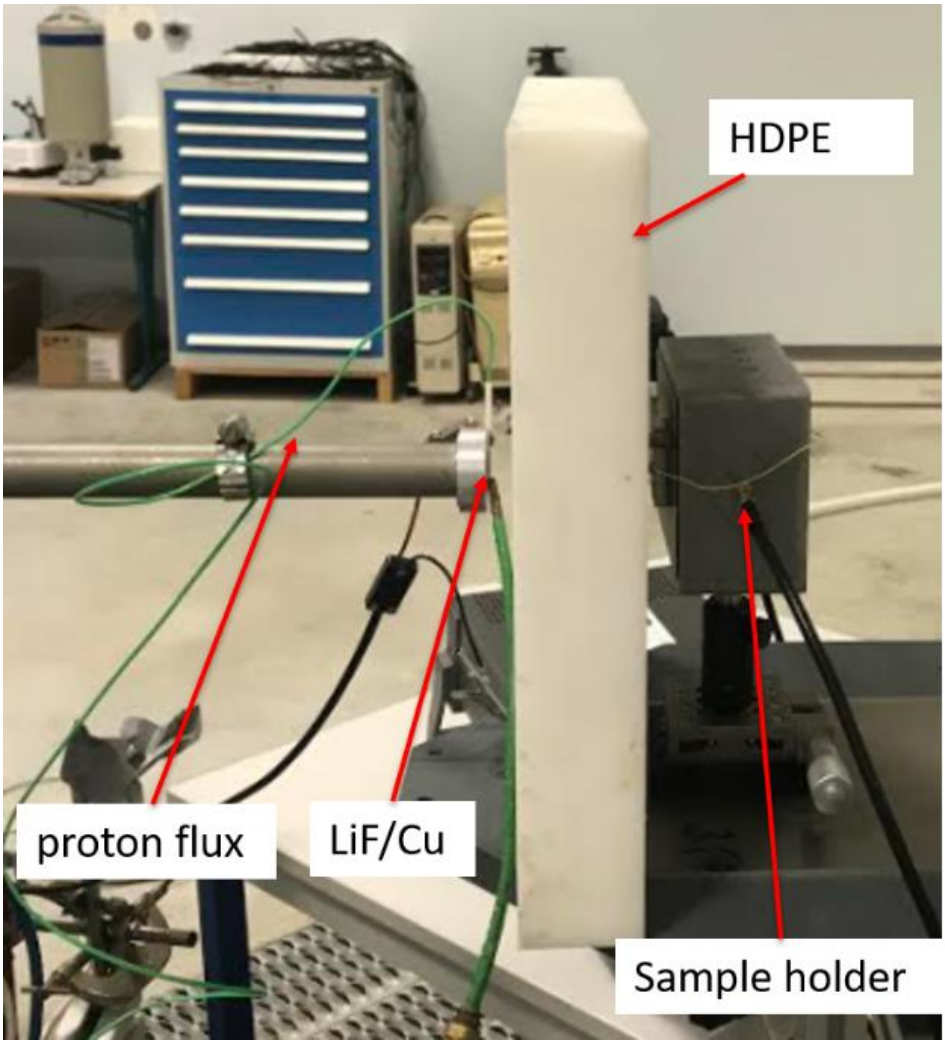

Figure 5-1: The experimental setup for neutron detection. The HDPE slab is placed in front of the LiF/Cu target and the distance from the LiF/Cu target to the MSM h-BN detector is 7 cm.

2. Neutron testing with MSM h-BN

2.1 Sensitivity (ΔI) of the MSM devices based on natural h-BN

Figure 5-2a shows the sensitivity (ΔI) of both MSM (Ni/ Au-Ni /Au) and (Ti/ Au-Ti /Au) devices for an applied voltage ranging from 0 V to 200 V. The two types of detectors were then subjected to a neutron flux of 3x104 n/cm2/s. An increase in current ΔI was observed.

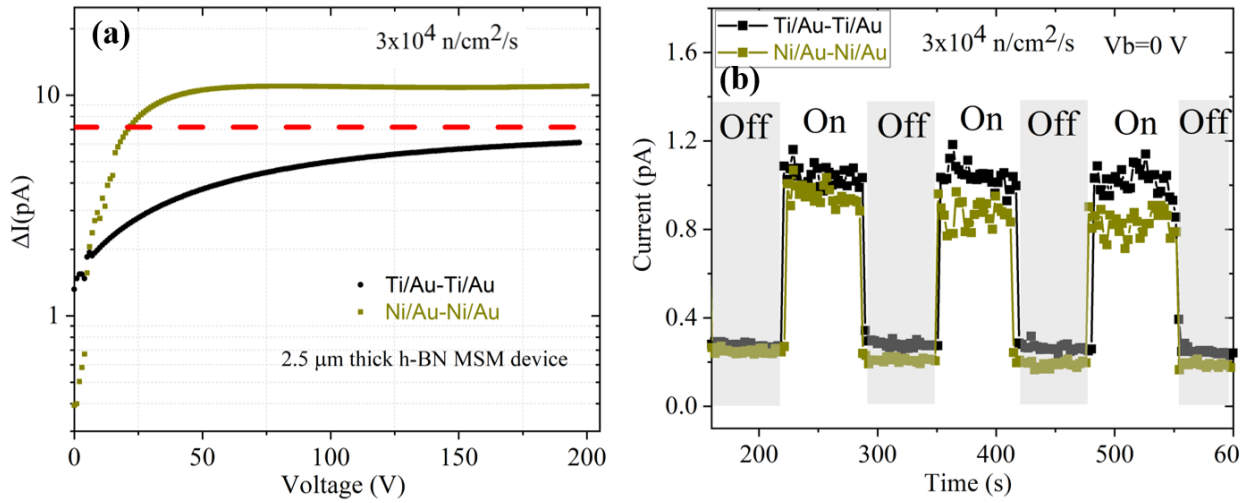

Figure 5-2: (a) Neutron induced current of natural h-BN MSM with Ti/Au-Ti/Au and Ni/Au-Ni/Au contacts when submitted to a neutron flux of $3x10^4$ n/cm^2/s. (b) Corresponding recording of the current variation at zero-bias for both devices.

Since the two MSM devices have asymmetric SBH, a nonzero ΔI is observed when the devices are not biased. These ΔI values at zero bias are likely overestimated due to the noisy signals and low currents. To confirm and refine the value of the unbiased ΔI, we recorded the current variation at zero bias for both devices subjected to a periodic neutron flux of $3x10^4$ n/cm^2/s, as shown in Figure 6-2b. A clear current variation is obtained with a ΔI of 0.7 pA and a sensitivity of 233%, which is similar for both detectors.

As the applied voltage is increased, both ΔI increase, reaching saturation at voltages above 50 V. At a bias voltage of 200 V (Figure 5-2a), the ΔI of the MSM detector with Ni contact is about twice that of the MSM detector with Ti contact. To estimate the magnitude of the photocurrent generated when a constant thermal neutron flux irradiates a 2.5-µm BN layer with 20% of the isotope ^{10}B. Following the same procedure as described in [1], the effective absorbed neutron flux (N_{abs}) can be determined as follows:

$$N_{abs} = \frac{t}{\lambda} \times N \quad (1)$$

Here, the thermal neutron flux (N) is 3×10^4 n/cm^2/s, t is the film thickness, and λ is the neutron absorption length. The average energy of the daughter particles calculated from the nuclear reaction between ^{10}B and the captured neutron is 2.34 MeV, which corresponds to 1.3×10^5 electron-hole pairs ($N(e^-)$) generated by a captured neutron. Therefore, the rate of free electrons produced is:

$$n = N_{abs} \times N(e^-). \quad (2)$$

After calculation and considering both electron and hole conduction, the theoretical value ΔI is estimated to be 7 pA (red dotted line in Figure 5-2a). Above 25 V, the ΔI of MSM detectors with Ni is higher than the theoretical value (gain >1). For MSM detectors with Ti, the ΔI is very close to this value at 200 V (gain <1). This could be explained by a gain mechanism due to the trapping of neutron-generated charge carriers at the metal-semiconductor interfaces [2-3], which decreases the SBH and allows more current to flow. This increase in current flow can be expressed as follows:

$$\Delta I^G = I_d \exp\left(\frac{\Delta\phi}{kT}\right) - 1 \quad (3)$$

Where I_d is the dark current, $\Delta\phi$ is the Schottky decrease due to generated carriers trapping, k is the Boltzmann constant and T is the absolute temperature.

According to Equation 3, the higher the dark current (I_d) and SBH decrease ($\Delta\phi$), the higher the internal gain. If we assume a similar $\Delta\phi$ for both MSM detectors, then the device with the larger dark current should have the largest ΔI, which is the case. However, a high gain is accompanied by a large Id, which decreases the sensitivity ($\Delta I/I_d$) of the detector. In our case, the MSM detector with Ni contact has a larger dark current and thus ΔI and weaker sensitivity than the MSM detector

with Ti contact. For the rest of the study, we then considered only the high-sensitivity MSM detector with Ti contact.

2.2 Comparison between natural and ^{10}B enriched BN based MSM with Ti/Au contacts

For this comparison, we used two MSM devices with Ti/Au metal contacts for both natural and ^{10}B-enriched BN films. Figures 5-3a and b show the change in neutron-induced current at zero voltage as a function of time for devices exposed to 1.5x10^4 n/cm^2/s (flux 1) and 3x10^4 n/cm^2/s (flux 2). We observed a clear response for both natural and ^{10}B-enriched BN MSM devices at zero bias voltage. Higher neutron current of the ^{10}B-enriched MSM device is obtained for both thermal neutron fluxes.

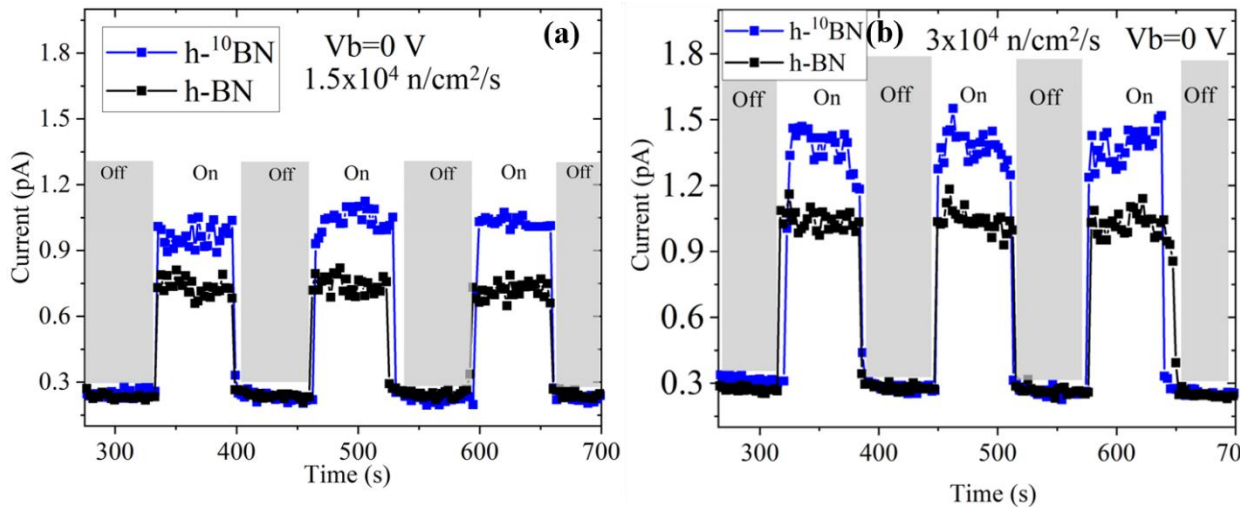

Figure 5-3. (a), (b) real time neutron response of the natural h-BN and ^{10}B-enriched h-BN MSM with Ti/Au-Ti/Au contacts at zero volt with flux 1 and flux 2 respectively.

The sensitivities of the natural and ^{10}B enriched BN detectors at 0V are 233% and 367%, respectively. These sensitivities cannot be directly compared with the literature because there is no value for BN at zero volts and the sensitivities reported in this material were obtained with different thicknesses at applied voltage. For example, Li et al [1] reported a current variation of

0.087 pA for a 1µm thick BN neutron detector operating under an electric field of over 4×104V/cm, which corresponds to a sensitivity of 170%. The neutron-induced current at zero volts in the MSM based on natural and ^{10}B enriched ^{10}B BN was compared. The neutron-induced current of ^{10}B enriched BN MSM is about 1.4 times higher than that of natural BN MSM at 0 volts (Figure 5-3). This difference is due to the increased ^{10}B atoms in the enriched BN material, resulting in a higher global thermal neutron capture cross section. In this case, more neutrons are absorbed, resulting in a larger excess free carrier density and consequently a higher current.

The same detectors (natural and ^{10}B enriched BN MSM with Ti/Au) were also studied under bias voltages of 100 and 200 V. The results obtained are shown in Figure 5-4, where the dark current of the two devices is almost the same. This means that the effect of the gain mechanism under neutron irradiation is the same. It can be observed that the response of the ^{10}B enriched BN MSM detector is systematically higher than that of the natural BN for all applied voltages and at different thermal neutron fluxes.

Comparing the ^{10}B effect, we find according to Figure 5-3 that the ratio of the neutron-induced current in ^{10}B to 11B films is between 3.2 and 4.5, which is very close to the theoretically expected value of 5 [1] . When the neutron sensitivity is calculated from Figure 5-4 for flux 2 and under 200 V bias, it reaches 316% and 1192% for natural and ^{10}B enriched h-BN detectors, respectively. Since the gain mechanism is present in both devices, we can conclude that this difference is due to the ^{10}B enriched BN films. In Figure 5-4, we see that the current induced by flux 2 is between 1.78 and 2.38 ± 0.5 times that induced by flux 1, showing good linearity of the detectors. These values are indicative of a remarkable response of the detectors to thermal neutrons.

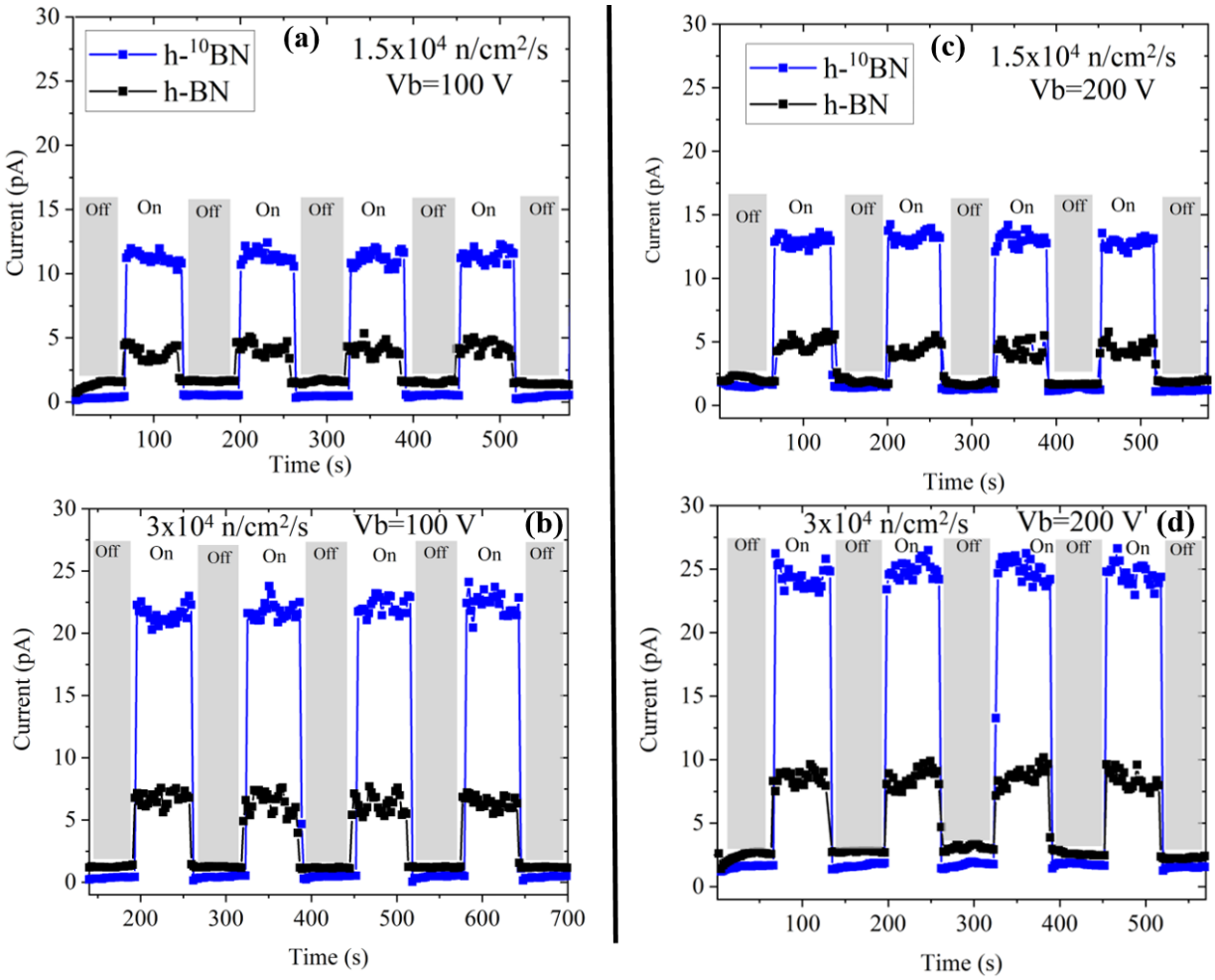

Figure 5-4: Real time neutron response of the natural h-BN and ^{10}B-enriched h-BN MSM with Ti/Au-Ti/Au contacts at 100 and 200 V. (a), (c) under flux 1 and (b), (d) under flux 2.

3. Neutron testing with MSM BGaN/GaN SLs

In the past, our group has used BGaN/GaN SLs to demonstrate various applications such as Bragg reflectors, high electron mobility transistors, and gas sensors [4-6]. In this study, we tested the BGaN/GaN SLs as neutron detectors because the BGaN layer contains the isotope ^{10}B, which can capture the thermal neutrons, and has low sensitivity to gamma rays. For the neutron tests of the MSM BGaN/GaN SLs, we applied the same conditions as for MSM BN detectors. We first performed the I-V measurements in the voltage range from -10 to 10 V in darkness and neutron flux. No signal change was detected due to the high conductivity of the devices. Then we

applied a very low voltage and measured the neutron response. Figure 5-5 shows the current-time (I-t) characteristics of the MSM BGaN/GaN SLs detector measured at a bias voltage of 0.1 V under alternating dark and thermal neutron flux of 3.x10^4 neutrons/cm2/s. Under neutron irradiation, an increase in current is observed and the neutron current is about 4 pA. The MSM BGaN/GaN SLs are very sensitive to neutron flux even at low applied voltage, which is not the case for a large number of neutron detectors such as ^{3}He gas detectors where the bias voltage is above 1 kV.

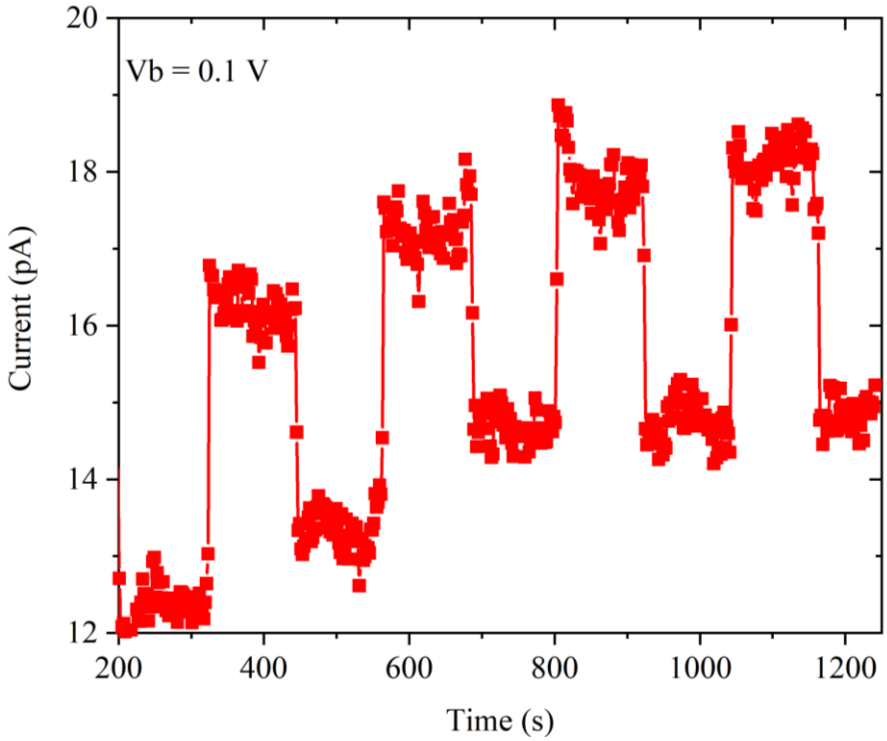

Figure 5-5: I-t characteristics of the MSM BGaN/GaN SLs neutron detector.

4. Neutron testing with PIN BGaN/GaN SLs

The PIN BGaN/GaN SLs devices were also tested under thermal neutron fluxes. As we can see in the dark I-V characteristics of the PIN structure in Figure 4-8, the measured current is in the micro-ampere range, which makes the detection of neutron signals very difficult. Therefore, we measure the neutron-induced current at low voltage (0.01 V) under a neutron flux of 3x10^4 n/cm^2/s

f. Figure 5-6 shows the measurements of the current-time variation. A consistent increase in electric current can be observed. At this applied voltage (0.01 V), the measured neutron current is 3 pA.

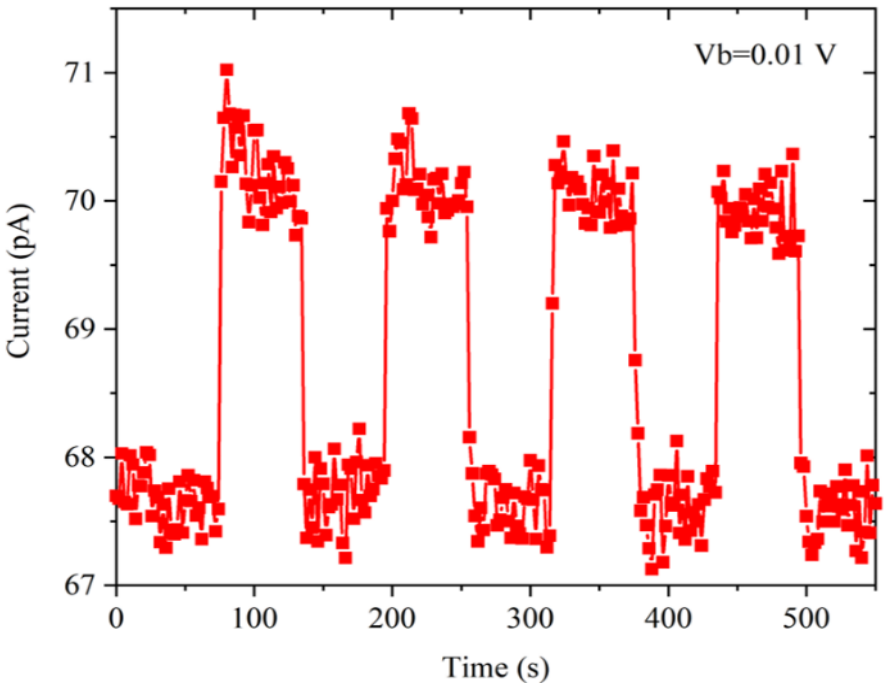

Figure 5-6: I-t characteristics of the PIN BGaN/GaN SLs detector.

At zero voltage, a neutron-induced current is expected due to the built-in electric field in the PIN BGaN/GaN SLs devices. For this reason, we have studied the response of the PIN structure at zero bias voltage under two neutron fluxes 2.3x104 n/cm2/s and 3x104 n/cm2/s. Figure 5-7 shows a clear neutron-induced current change for both neutron fluxes. These results confirm the presence of a residual electric field that swept out the generated electron holes.

PIN and MSM BGaN/GaN SLs had sufficient neutron detection capability, and successful neutron detection was realized. These results indicate that the BGaN semiconductor material can be used in neutron-detection technology. Further neutron testing are needed to confirm our results.

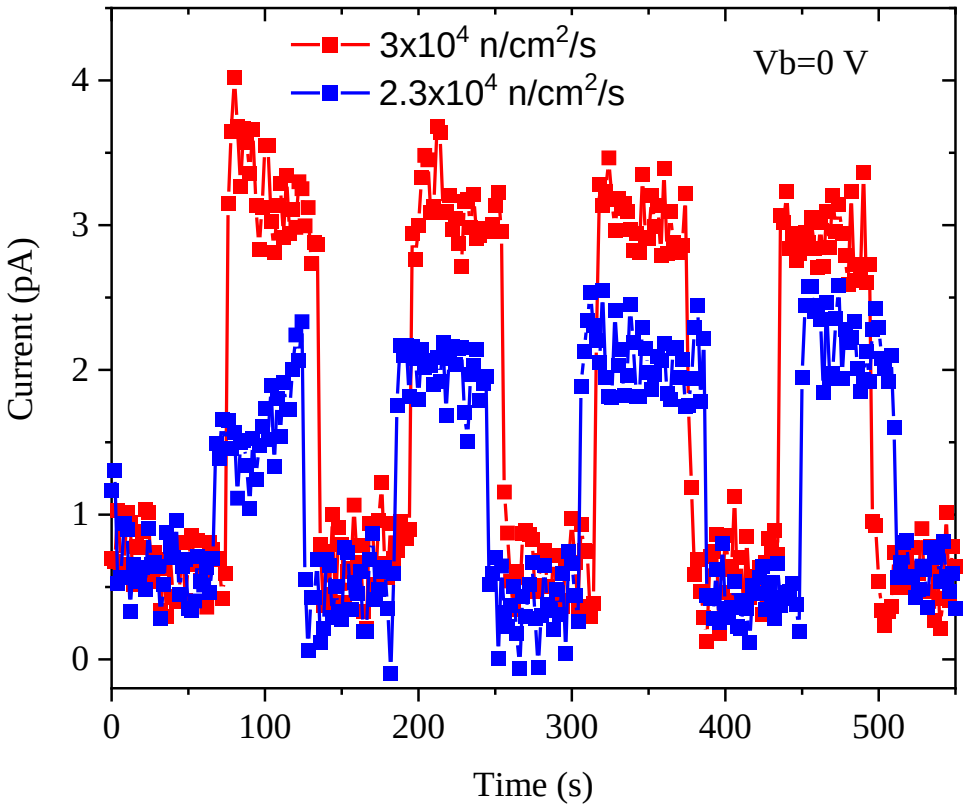

Figure 5-7: I-t characteristics of the PIN BGaN/GaN SLs detector at zero volts.

In summary, we have tested the boron-containing III-N materials under thermal neutron flux. The BN based detector (natural and ^{10}B enriched) showed a measurable neutron induced current at zero bias voltage. These MSM detectors had a sensitivity to thermal neutron as high as 233% and 376% at 0 volt natural and ^{10}B-enriched respectively. Linear neutron response of the detectors under thermal neutron flux and bias voltages was obtained. In addition, the neutron induced current of the ^{10}B enriched BN MSM detector is up to four times larger than the one with natural boron. MSM and PIN devices structure of BGaN/GaN SLs showed high sensitivity to thermal neutron.

CHAPTER 6: DOPING OF BORON NITRIDE AND B RICH BAlN ALLOYS

Efficient neutron absorption in neutron detectors based on BN requires 227µm thick layers for natural BN and 47 µm thick layers for ^{10}B enriched BN [1]. These thick BN layers lead to poor crystalline quality (disordered phase such as turbostratic), which directly affects the charge carrier collection. Improving the crystalline quality of the thick BN layer is a major challenge; an alternative solution is to use a p-n or even p-i-n structure of h-BN for neutron detectors. This will improve the carrier collection and the overall efficiency of the detector. In addition, there are conflicting experimental and theoretical studies on controlling the p-type conductivity of h-BN using Mg as a dopant, as mentioned in Chapter 1. Further research on this important topic is needed. In this chapter, we report an experimental study on the electrical behavior of Mg in h-BN. To evaluate the potential of h-BN with Mg doping for device applications, we fabricate Mg-doped h-BN /n-AlGaN heterostructures and report the electrical properties of these devices. At the end of this chapter, we presented the study of boron rich BAlN alloys which is promising for neutron detection applications.

1. Growth of Mg-doped h-BN

Materials were grown in MOVPE close-coupled showerhead 3 × 2” system on (0001) sapphire substrates using triethylboron (TEB), and ammonia (NH_3) as B, and N precursors, respectively. The h-BN layers were grown at 1280 °C in hydrogen ambient at 85 mbar. The growth of h-BN layers was initiated with a TEB preflow. Biscyclopentadienyl-magnesium (Cp2Mg) was used as the source of Mg dopants. First, we grew 50 nm thick undoped h-BN, referred to as sample A, for reference. Then, we studied the effect of Mg doping on the structural and morphological characteristics of three different sets of h-BN samples referred to as B, C and D, grown at Cp2Mg molar flow rates of 0.9, 1.8 and 2.9 µmol/min, respectively. The h-BN layer thickness of the full

set of samples was 50 nm, and all the other parameters including TEB molar flow were kept constant. The morphological and structural properties were characterized by a scanning electron microscope (SEM) and high-resolution X-ray diffraction (HRXRD), respectively. I–V and capacitance measurements were performed using a Keithly 4200A SMU and a Keysight E4990A impedance meter, respectively. I-V measurements were performed to verify the ohmic behavior of the contacts on h-BN samples A-D. Van der Pauw (VdP) and Hall Effect measurements were performed to determine the resistivity and doping of the grown samples.

1.1 Morphology characterizations of undoped and Mg doped h-BN Layers

The surface morphology of the undoped h-BN (sample A) and the Mg-doped h-BN samples (samples B–D) with three different Cp2Mg molar flows are shown in Figure 6-1. All the samples were optically transparent with a smooth surface as shown in the insets of Figure 6-1. Under SEM, the undoped h-BN sample exhibited an organized semi-hexagonal wrinkled surface (Figure 6-1a), which is comparable to our previous studies. Wrinkle formation is the result of the compressive stress during sample cooling. Similar wrinkles were observed on the B and C h-BN samples (Figures 6-1b,c). These surface morphologies confirm that the h-BN in samples A–C is layered. On the other hand, the h-BN sample D presented in Figure 6-1d shows wrinkled surface morphology decorated with a high density of particles. This morphological change can be directly correlated to the heavy Mg doping. Previous studies have shown that insufficient NH_3 flow or a parasitic reaction between the precursors may lead to grain formation, which is BN in the disordered phase (turbostratic/amorphous) [2-6]. At high Cp2Mg flow, Mg may block nitrogen atoms, leading to a low number of active N atoms in the growth front, resulting in stacking fault-induced variations in strain, which then generate a higher density of misoriented BN grains in sample D.

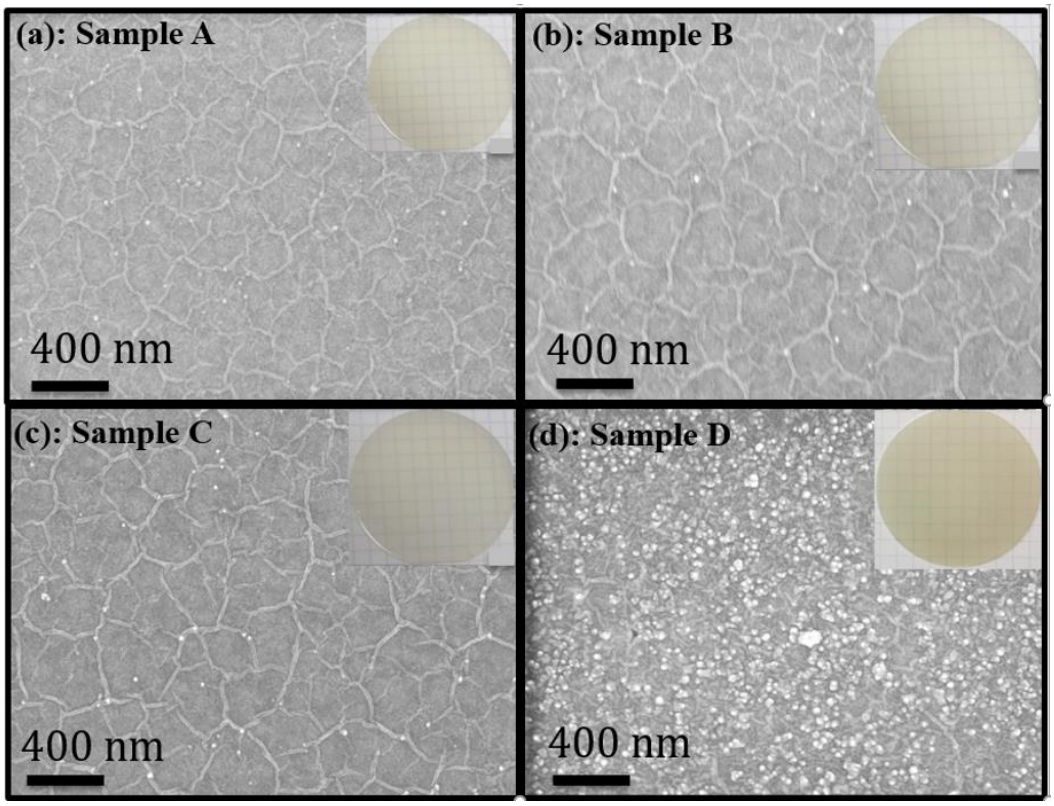

Figure 6-1: (a–d) SEM images of h-BN samples A, B, C and D, respectively. Insets show photographs of the respective samples.

1.2 Structural characterizations of undoped and Mg doped h-BN Layers

The crystalline characteristics of the as-grown samples were studied with HR-XRD 2θ-ω scan measurements as shown in Figure 6-2. All the samples exhibited a peak around 26° (Figure 6-2a) which is clearly the (002) plane reflection from the sp2-bonded h-BN. The (004) plane diffraction peak of h-BN was also observed at 53.5°. However, the increase in Mg led to lower intensity and broader peaks. Furthermore, when compared to the peak position of sample A (25.86°), a shift of the (002) peak was observed in sample B (25.72°). This may be related to the deformation of the surrounding lattice because of the difference of atom sizes between B and Mg [7]. However, the peak shift at the lower angle was not observed in samples C and D. This is related to the formation of an accumulation of disordered phases in samples C and D, which overcomes the effect of Mg

incorporation. It is assumed that all the Mg atoms are probably not in the substitutional sites of boron. Therefore, an increase in non-substitutional Mg incorporation with the increase in Mg flow may generate additional heterogeneous strain that contributes to the increase in the FWHM of (002) reflection (Figure 6-2b) [8]. This increase in FWHM suggests a degradation of the crystalline quality for samples B–D. Moreover, the asymmetric shape of the (002) peak in D is likely a result of localized variation of strain in Mg doped h-BN layers, which causes formation of a large number of disordered BN particles.

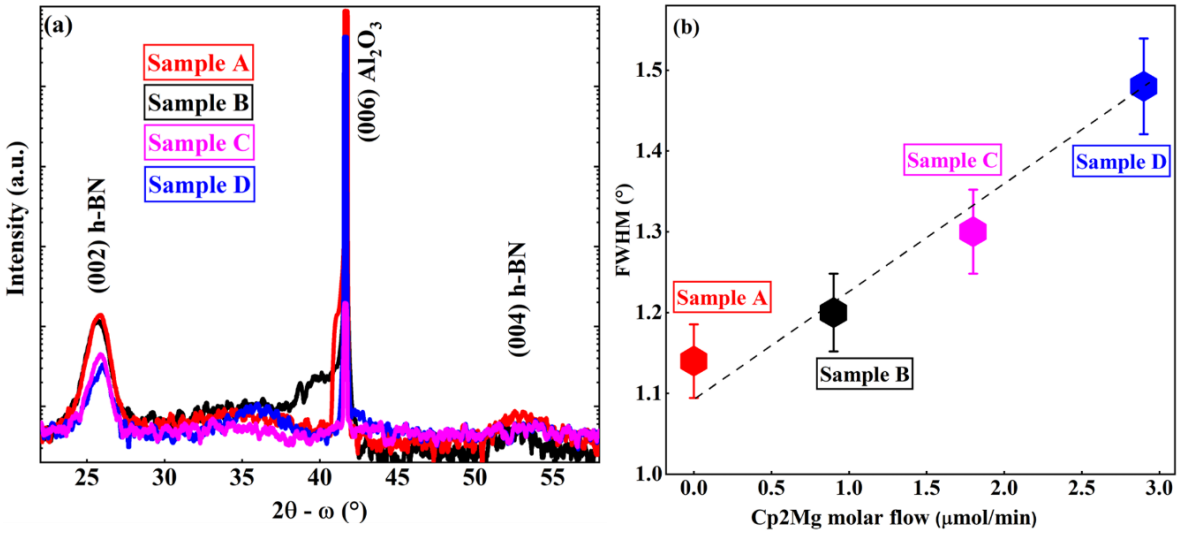

Figure 6-2: (a) HR-XRD 2θ-ω scans of the grown h-BN samples; (b) FWHM variation of (002) diffraction peak of the different h-BN samples versus Cp2Mg molar flow.

1.3 SIMS measurement of Mg doped h-BN

To estimate the Mg concentration in our h-BN films, secondary ion mass spectrometry (SIMS) measurements were performed. The Mg concentration increased super-linearly with the increase in Cp2Mg molar flows, as shown in Figure 6-3. Similar trends have been obtained in other III-V materials [9-10]. Mg incorporation reached 4×10^{18} atoms/cm3 for a Cp2Mg molar flow of 2.9

µmol/min (sample D). For the undoped sample, the value of Mg at 1×10^{15} atoms/cm3 corresponds to the limit of SIMS detection and does not correspond to a real concentration.

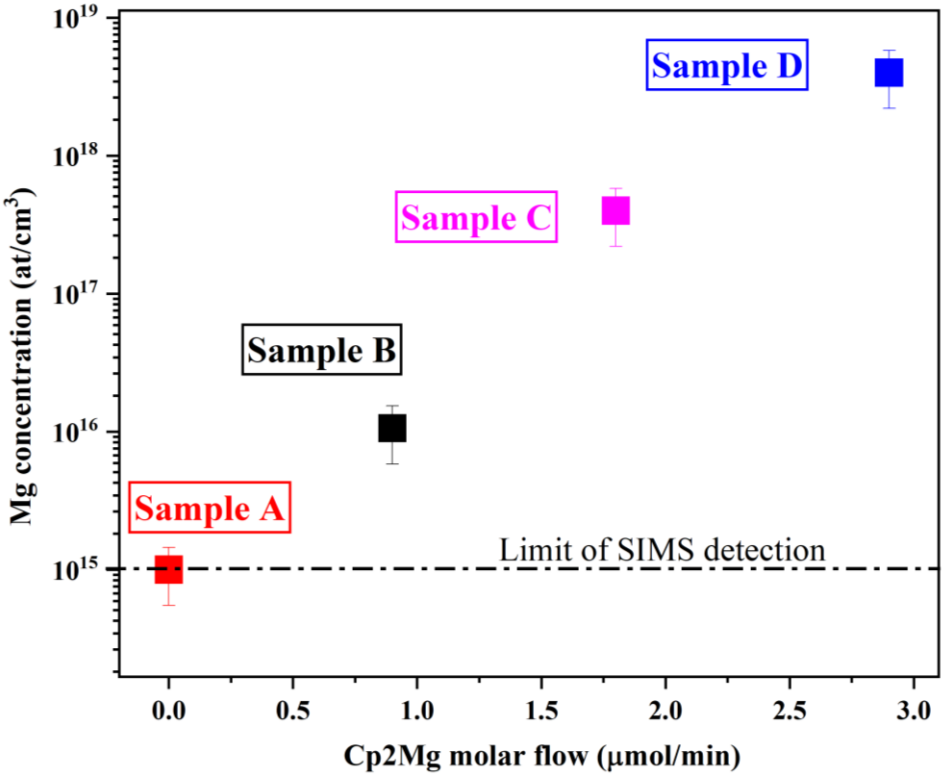

Figure 6-3: Cp2Mg molar flow dependence of the Mg concentration.

2. Electrical characterizations of the Mg-doped h-BN

2.1 I-V characteristics

I–V measurements were performed on the four A–D samples. These measurements obtained information on lateral transport (perpendicular to the c-axis) in h-BN: the strong anisotropy of h-BN may result in different resistivity and transport in the vertical direction (parallel to the c-axis). Figure 6-4 shows the current measurement versus voltage recorded in the four h-BN samples. Whatever the sample, the I–V dependence was linear, confirming that the contacts are ohmic. It is also clear that increasing the Mg concentration results in an increase in the current for a given voltage. The dependence of the I–V slopes on the Mg concentration is reported in the inset of Figure 6-4. There was a large increase in the conductivity from sample A to sample B and then

a slight increase from sample B to sample D. This behavior is probably related to the generation of point defects [11] with large Mg concentration in the layer, leading to a limitation (compensation) of the carrier diffusion length, especially for sample D.

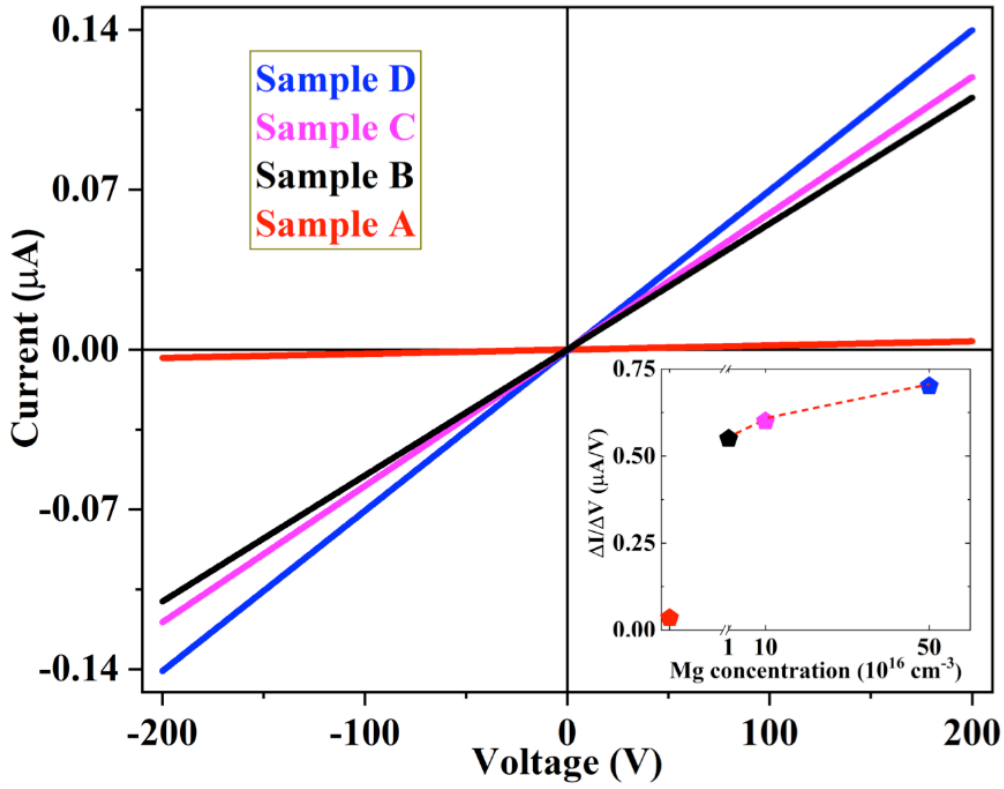

Figure 6-4: Current versus voltage measurements recorded in the undoped and Mg-doped h-BN A-D samples. The inset shows the variation of the slope of the different curves with the Mg concentration.

2.1 Resistivity measurement

The resistivity of the undoped and the highly doped samples was determined from Van der Pauw (VdP) measurements performed at different temperatures figure 6.5. The resistivity was shown to vary between 1.5×10^6 Ω.cm at 78 K and 2×10^3 Ω.cm at 430 K for highly doped h-BN, and between 2×10^6 Ω.cm at 78 K and 1×10^5 Ω.cm at 430 K for undoped h-BN. At room temperature, the resistivity of the undoped sample (A) was 2×10^5 Ω.cm. Compared to literature

reported results, this value is much smaller. Indeed, values of 7.1×10^{14} Ω.cm have been reported for 50 µm thick undoped BN layer [12] and between 4×10^{13} and 2.1×10^{15} Ω.cm for h-BN ceramics obtained by a field assisted sintering technique of h-BN powders [13]. This large difference can be attributed to the degree of disorder in sintering, the difference in layer thickness but also to some residual impurities such as carbon and oxygen, as revealed by SIMS measurements.

At room temperature, the resistivity of the sample with the highest doping (D) was 2×10^{4} Ω.cm, with a doping concentration of 5×10^{15} cm^{-3}. These values can be compared to those obtained by Sun et al. [7] who reported a resistivity and doping concentration of 1.2×10^{-5} Ω.cm and of 1.7×10^{14} $cm^{-2,}$ respectively, for an h-BN monolayer grown on Cu foil and transferred on SiO_2. For a thicker layer of h-BN (300 nm), the reported resistivity and doping concentration are 2.3 Ω.cm and $1.1 \times 10^{18} cm^{-3}$ [14,15], respectively.

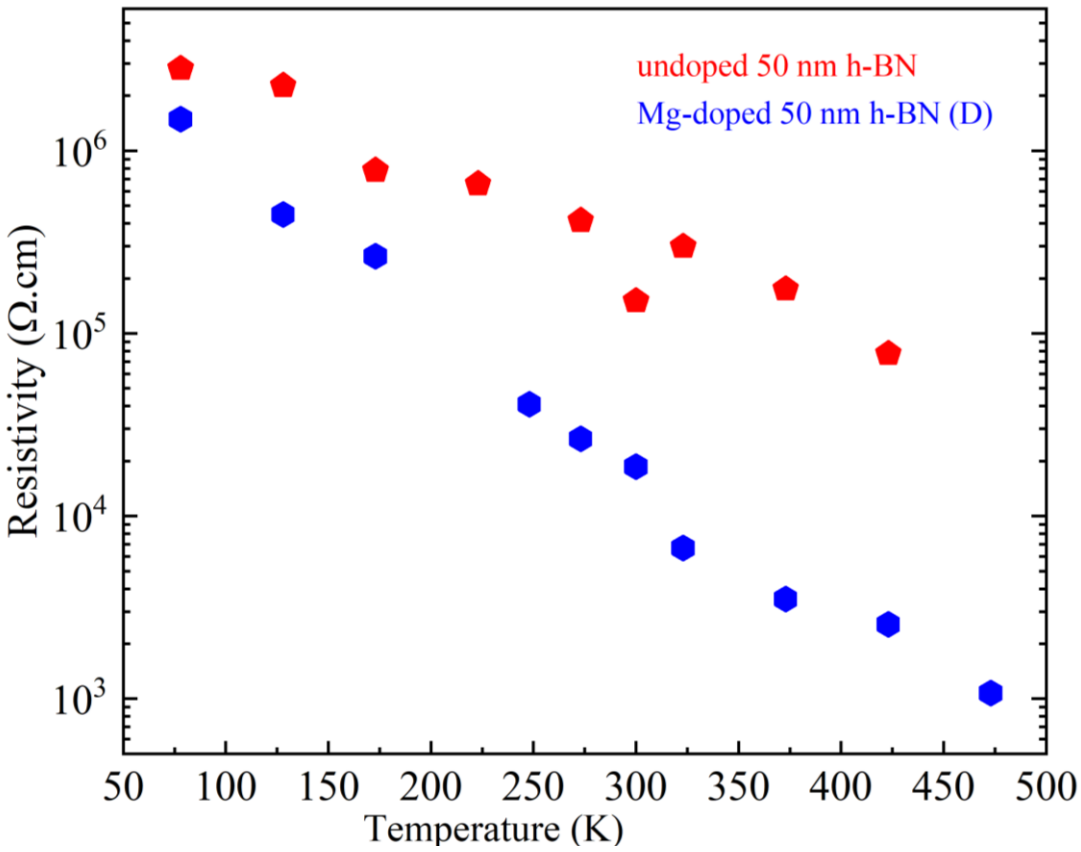

Figure 6-5: Resistivity of the 50 nm thick undoped and Mg-doped h-BN (sample D) versus temperature.

2.1 Activation energy

For the doped layer, an activation energy of 160 meV was derived from the slope of the Arrhenius plot Figure 6.6 and attributed to the Mg level in h-BN, which is in the range of the reported values (30–300meV) in the literature for Mg doped BN films [14-16]. The p-type conductivity was confirmed by the positive Hall voltage V_H derived from Hall measurement. Using this V_H value and the sheet resistance deduced from the VdP measurements, we determined in the highly doped sample D a p-type carrier concentration of 5×10^{15} cm^{-3}, which is three orders of magnitude lower than the Mg atomic concentration measured by SIMS. One can then estimate the electrical activation of Mg around 1%.

In order to further investigate the p-type conductivity, we designed and studied a p-n h-BN/n-AlGaN heterojunction as discussed below.

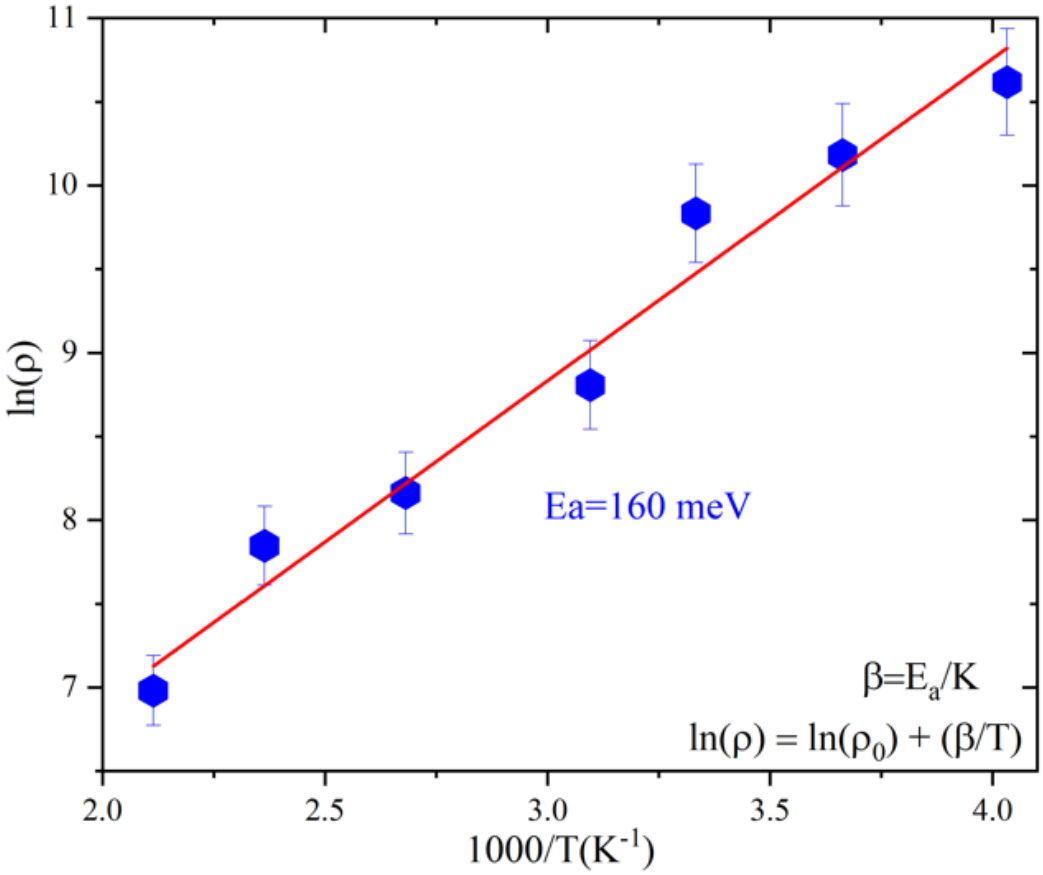

Figure 6-6: Activation energy of the 50 nm thick Mg-doped h-BN.

3. Heterojunction of Mg-doped h-BN/n-AlGaN

3.1 Growth of 50 nm h-BN on n-AlGaN (58% of Al content)

Two heterostructures made of 50 nm undoped and Mg doped h-BN grown on 500 nm thick n-AlGaN (58% Al composition, Si doped at 1.03×10^{17} cm^{-3}) on an AlN/sapphire template were grown. The first was grown with undoped h-BN on n-AlGaN to be an i-n junction (sample E), and the second was grown with Mg-doped h-BN with the purpose of forming a p-n heterojunction (sample F). The n-AlGaN layer with 58 % Al content was chosen because n-doped BN is experimentally infeasible and it is difficult to have high quality n-doped AlN. The Cp2Mg molar

flow used for sample F was the same as the one used for sample D (2.9 µmol/min). H-BN/AlGaN heterostructures were realized by growing undoped and Mg doped h-BN layer on Si doped $Al_{0.58}Ga_{0.42}N$/AlN/sapphire template wafer denoted by samples E and F, respectively. Figure 6-7 shows the measured HR-XRD 2θ-ω symmetric scan of (002) peak of the grown heterostructures. Clear diffraction peaks were identified at 25.8°, 35.3° and 36.1° which correspond to (002) reflection of h-BN, AlGaN (58% Al) and AlN, respectively. No other diffraction peak related to BN was observed by HRXRD scans indicating that the h-BN layer on AlGaN/AlN template is single phase.

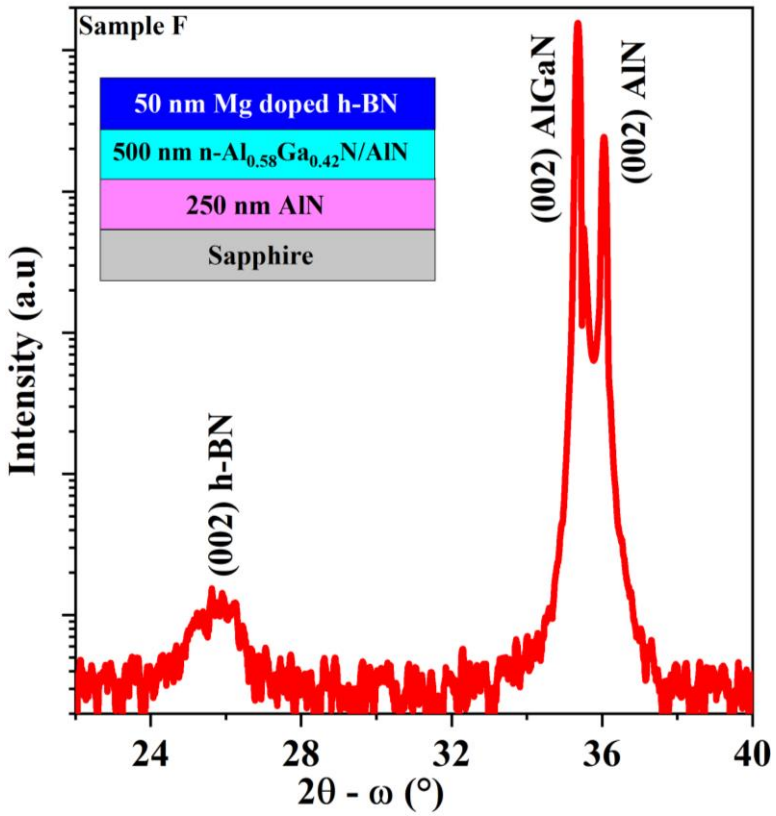

Figure 6-7: HR-XRD 2θ-ω symmetric scans of the Mg doped h-BN/n-$Al_{0.58}Ga_{0.42}$ N/AlN/sapphire heterostructures (Sample F). Inset shows the grown structure.

For the fabrication of samples E and F, a standard photolithography-based process was employed. First, mesa-etching isolation was achieved by inductively coupled plasma with

BCl_3/Cl_2/Ar chemistry. Ti/Al/Ni/Au and Ni stacks were used for the n-contact and the p-contact, respectively. Each metal layer was deposited by thermal evaporation. N-contact annealing was carried out at 1050 °C for 6 s under N_2, then the p-contact was annealed at 1020 °C for 60s under N_2 atmosphere.

3.2 Electrical characterizations of the heterojunction

a) I-V characteristics at room temperatures

Typical I–V curves of the undoped and Mg doped h-BN on n-AlGaN heterostructures recorded at room temperature are illustrated in Figure 6-8. Remarkably, at forward bias, the current of Mg doped h-BN/n-AlGaN device was 7 orders of magnitude higher than that of the undoped h-BN/n-AlGaN one. In the Mg doped h-BN/n-AlGaN device (sample F), the leakage current under reverse bias voltage was reasonably low with a value of 1 μA at −10 V, but it was not saturated as expected for an ideal p-n diode, and it continued to increase with the reverse voltage. This suggests that there are leakage current paths related to the deep defect levels in the depletion layer of h-BN [17].

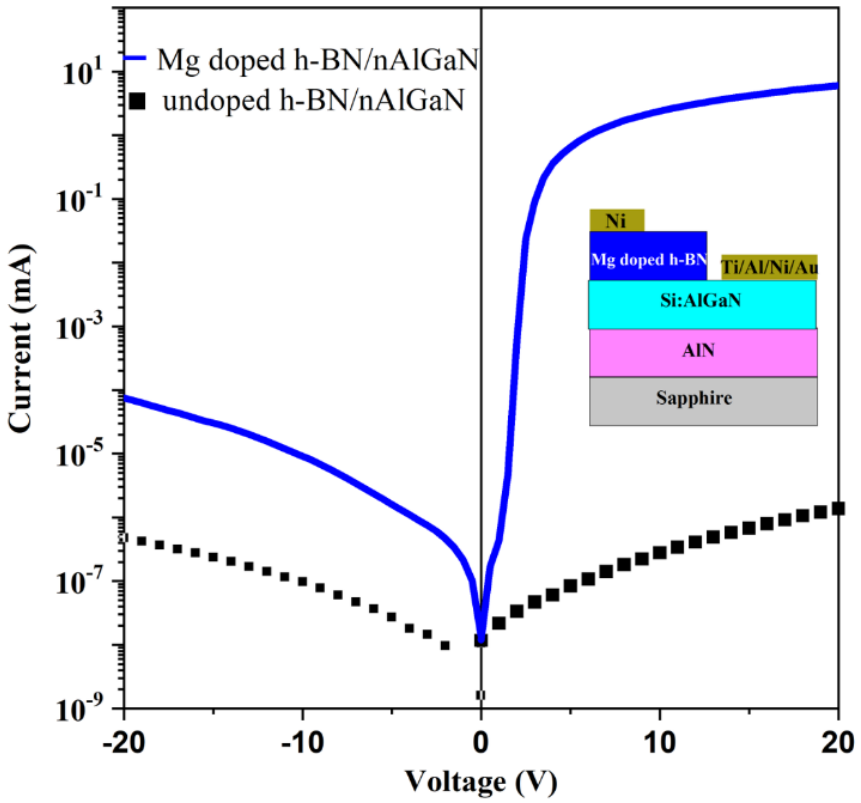

Figure 6-8: Current–voltage characteristics of undoped and Mg doped BN/n-$Al_{0.58}Ga_{0.42}N$ (Samples E and F) devices measured at room temperature.

b) I-V characteristics at different temperatures

The reverse and forward I–V characteristics of the p-hBN/n-AlGaN heterojunctions were studied at different temperature from 123 to 423 K as shown in the semilogarithmic plot of Figure 6-9. At forward bias, all the I–V curves exhibited strong saturation due to high series resistance, which likely originated from the resistance of the long lateral path in n-AlGaN, which had a measured carrier concentration of 1.03×10^{17} cm^{-3}. As seen in the inset of Figure 6-9, the 2×2 mm^2 ohmic contact pads were 3 mm away from each other, which is much larger than the 50 and 500 nm thickness of the h-BN and n-AlGaN layers, respectively, so that the resistance of the n-AlGaN layer in the lateral direction was much larger than the resistance of the heterojunction in the vertical one. As shown in Figure 6-9, the current increased significantly with the temperature in the range

300 to 373 K and then started to saturate at higher temperature. An inverse trend was observed for the threshold voltage. It varied from 3.2 V at 123 K to 1.5 V at 423 K. This might be due to the activation of some defects with the temperature increase. This assumption is consistent with the increase in the current at reverse bias with the temperature. For instance, at −5V, the leakage current increased from 30 pA at 123 K to 0.2 mA at 423 K.

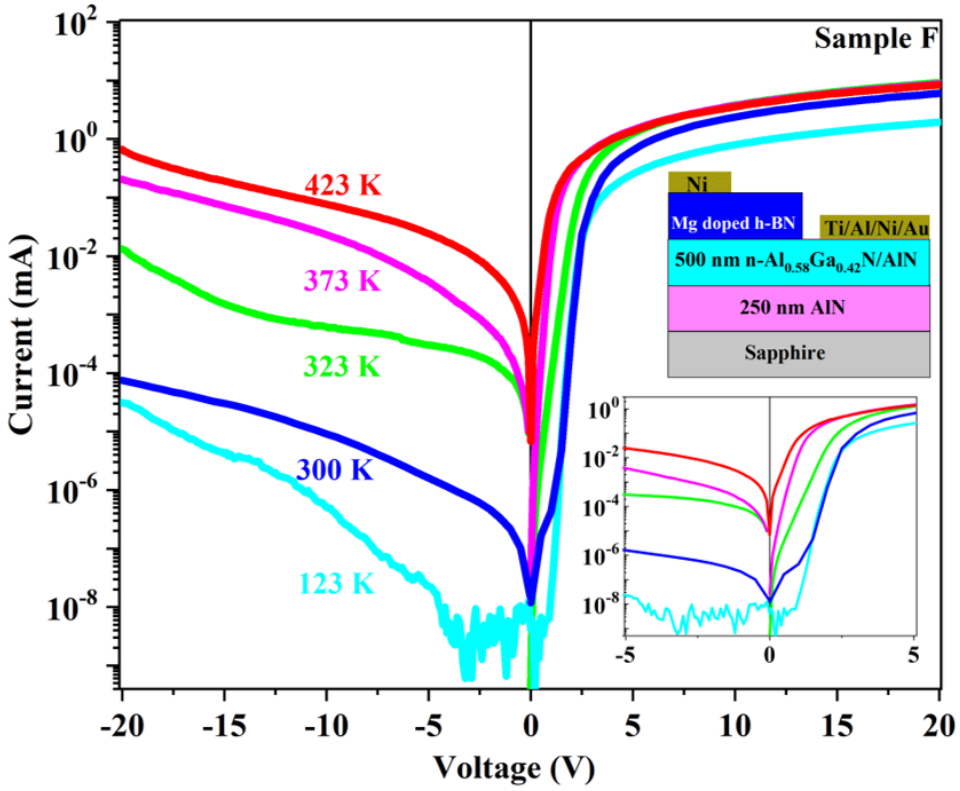

Figure 6-9: (**a**) I–V characteristics of Mg doped BN/n-$Al_{0.58}Ga_{0.42}N$ (Sample F) device recorded at different temperatures. Inset (**b**): I–V zoom-in of sample F.

c) Photocurrent generation

As the heterojunction showed better I–V characteristics at low temperature (low current leak), a set of P-N diodes were cooled to liquid nitrogen temperature and illuminated under UV laser light at 266 nm and 10 mW of optical power. Illumination occurred on the p-side of the junction through the Mg doped h-BN, next to the contact pad, as shown in the inset of Figure 6-10. As the

266 nm laser was below the bandgap of h-BN and above the bandgap of $Al_{0.58}Ga_{0.42}N$, UV absorption primarily occurred in the $Al_{0.58}Ga_{0.42}N$. Even with low output power laser of 10 mW, the partial absorption of the glass window of the cryostat, and the likely low collection efficiency hindered by the lateral transport in both h-BN and AlGaN, a significant photocurrent (120 pA at 0 bias voltage) was obtained. The generation of a photocurrent is evidence of the existence of built-in electrical field at the junction between Mg doped h-BN and n-AlGaN.

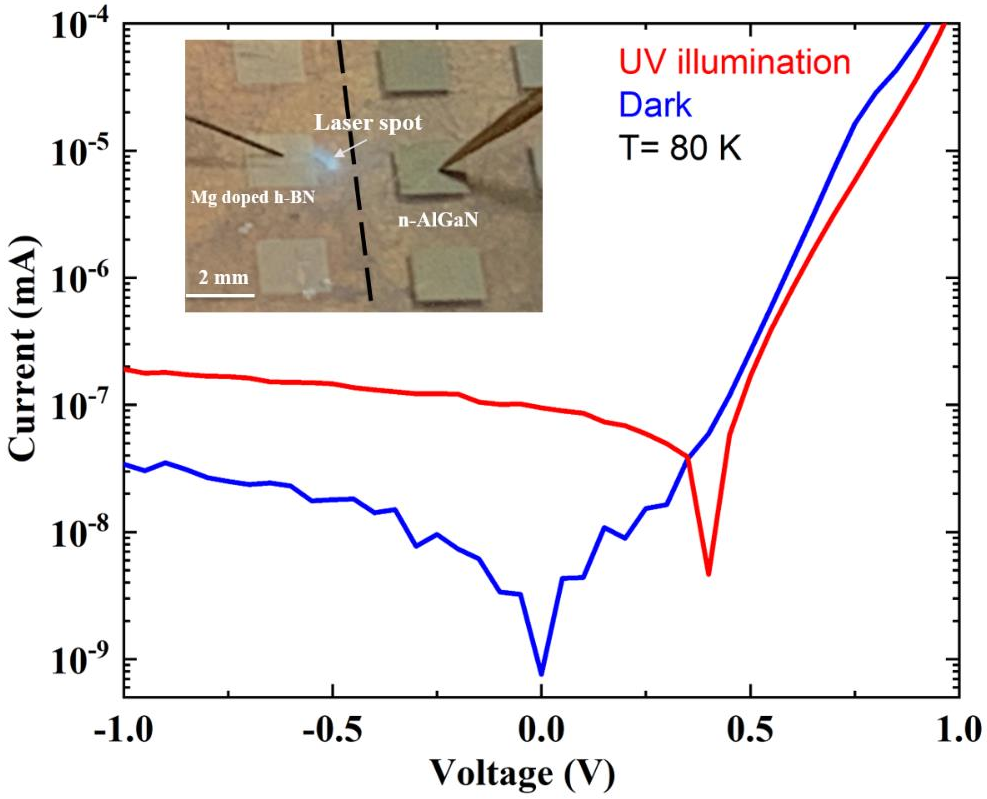

Figure 6-10: I–V curve recorded in Mg doped h-BN/n-$Al_{0.58}Ga_{0.42}N$ (Sample F) at T = 80 K with and without UV laser illumination. The inset shows a photograph of the top view of the heterojunction with the electrical contact pad and the location of the laser spot.

d) C-V measurements

CV measurements at room temperature and $1/C^2$ plot versus voltage are both shown in Figure 6-11. For forward voltage, the capacitance measurement was limited to small voltages since

the forward bias current and the diffusion capacitance affect the accuracy of the capacitance measurement. For reverse applied voltage, the capacitance decreased, as expected for a p-n diode, since the depletion region width increased accordingly. At larger negative voltage, the capacitance did not saturate, which indicates a moderate p-doping concentration (here, we assume that the n-doping concentration of the AlGaN layer is much larger than the p-doping concentration of the h-BN layer, leading to a depletion mostly located in the h-BN layer). The dotted line in the $1/C^2$ plot formed a reasonable linear fit at voltage close to zero from which one can conclude that the doping concentration was almost constant close to the Mg doped hBN/n-AlGaN interface. Extrapolation of the low voltage $1/C^2$ measurements (see Figure 6-11) resulted in a built-in voltage of 3.9 V, consistent with the bandgap of the $Al_{0.58}Ga_{0.42}N$ material, and a small discontinuity between the valence bands of h-BN and AlGaN as reported in XPS heterostructures experiments [18]. It is worth mentioning that the measured capacitance was much lower than that expected for a 2 × 2 mm^2 surface area of the device. This could be attributed to either a partial oxidation of the Ni pad (the current spread in the pad has been noticed to decrease with time) leading to a decrease in the effective surface area and/or a large resistance of the AlGaN path, which attenuates the AC capacitance signal. This makes extraction of the p doping from the C-V measurements complicated.

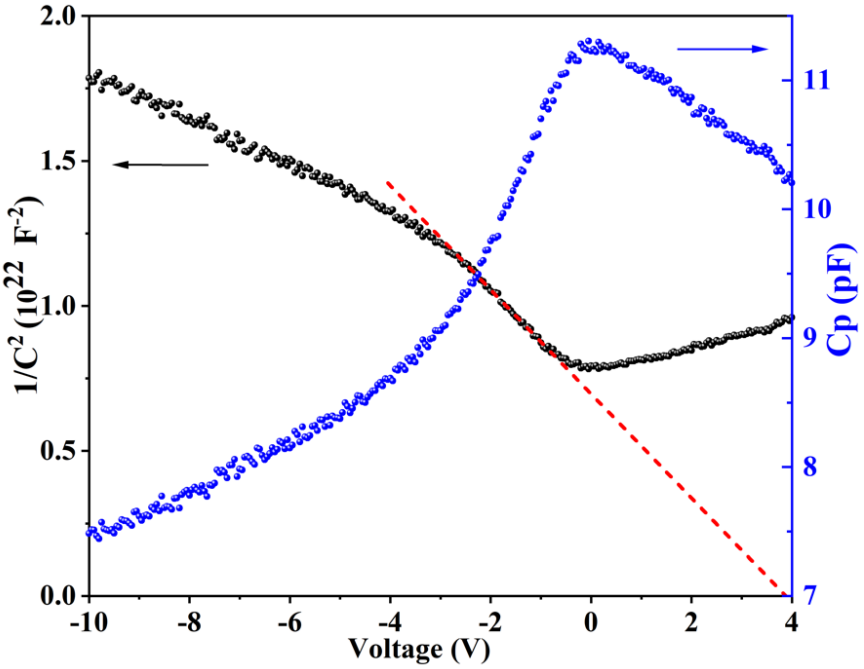

Figure 6-11. Capacitance voltage measurement in Mg doped h-BN/n-$Al_{0.58}Ga_{0.42}N$ (Sample F) measured at 1 MHz and room temperature, and corresponding $1/C^2$ plot versus voltage.

4. Boron rich BAlN alloys

Since the boron composition in the converter layer is crucial for efficient thermal neutron detection, we have studied the growth of BAlN alloys with very high boron content. The growth of boron-rich BAlN alloys has not been explored in the literature. The growth of boron-rich BAlN alloys and the understanding of their fundamental structural and optical properties are of great importance.

The BAlN alloys were grown directly on c-plane sapphire substrates without any buffer in an Aixtron MOVPE close coupled showerhead (CCS) reactor. Triethylboron (TEB), trimethylaluminum (TMAl) and ammonia (NH_3), were precursors for boron, aluminum, and nitrogen, respectively. 20 nm thick of BAlN layers were grown at 1280°C and 90 mbar pressure. The TMAl/III ratio were varied from 0 to 25, in order to increase the Al content in gas phase, all other parameters were kept constant.

The surface morphology of BAlN alloys grown on sapphire substrates with four different TMAl/III ratios is shown in figure 3-7. At a low TMAl/III ratio (figure 3-7a and b), we observe honeycomb like wrinkles on the surface which is comparable with the standard morphology of un-alloyed 2D h-BN. The formation of the wrinkles is the consequence of the compressive stress from cooling process as reported earlier by Li et al [19] This morphology confirms that these samples are completely layered. When the TMAl/III ratio is increased, these wrinkles are less pronounced and small grains were obtained as seen in figure 3-7c. Subsequently at the higher

TMAl/III ratio of 25, the morphology of the BAlN alloy consists of 3D grains with complete absence of wrinkles (figure 3-7d). The 2D - 3D transition of the morphology reveals the influence of the TMAl/III ratio on the surface of BAlN alloys. Further characterizations have been performed to understand the structural changes of these BAlN alloys.

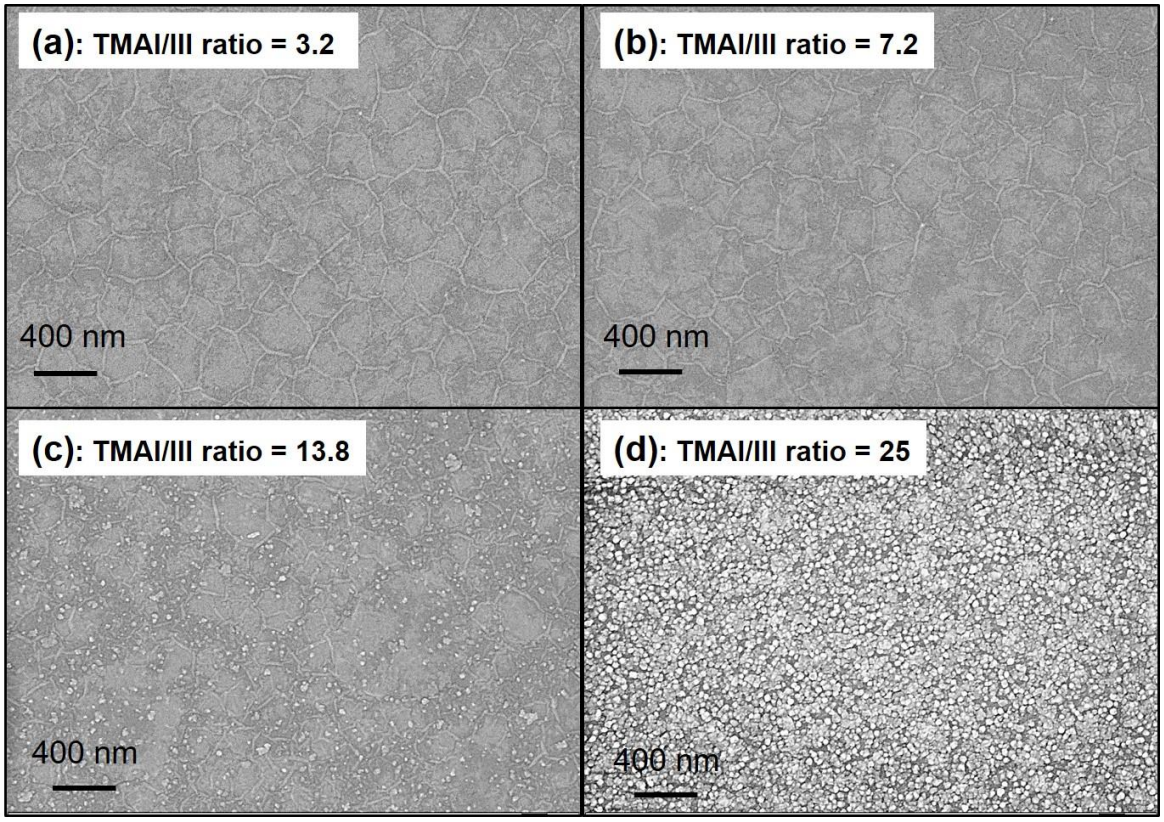

Figure 3-7: SEM images of BAlN alloys grown on sapphire with four different TMAl/III ratios. (a) 3.2, (b) 7.2, (c) 13.8, and (d) 25.

Figure 3-8a shows High-Resolution X-Ray diffraction (HR-XRD) of the 20 nm thick BAlN alloys grown with the different TMAl/III ratio. We have observed only the diffraction peak at around 26.0° for samples with TMAl/III ratio from 0 to 13.8 which confirms the formation of a layered BAlN alloys. At the TMAl/III ratio of 25, in addition to the h-BN peak, the $2\theta-\omega$ scan showed the presence of second peak at 35.9° corresponding to the (002) w-AlN. The observation of the two peaks indicates the phase separation in this sample. By increasing the TMAl/III ratio,

the position of (002) h-BN peak is found to be shifted toward higher angle (by 0.2°), except the BAlN alloy grown with the highest of TMAl/III ratio due to the phase separation (inset of figure 3-19a and 3-8b). Because the boron (B) atoms are smaller than aluminium (Al), adding the Al into h-BN layer can rise to the local tensile stress. This stress will lead to the increase of the lattice parameter *a* and the decrease of the lattice parameter *c*. According to Bragg's law, the crystal lattice *c*, in our study is calculated to decrease from 6.92 Å (for pure h-BN) to 6.86 Å (for BAlN alloy grown with TMAl/III ratio of 13.8). This decrement indicates the increase of the Al content in our BAlN alloys. In case of the phased separated sample, the h-BN (AlN) peak was found to be shifted (around 0.05°) to the higher (lower) angle, compared to the reported values [19-20]. We attribute this shift to the presence of BAlN alloy. SIMS measurements will be discussed later for more complete study of this sample. In addition to this shift, the full width half-maximum (FWHM) of the h-BN diffraction peak increases linearly with the TMAl/III ratio (figure 3-8c). This broadened FWHM relates to the incorporation of Al in the h-BN layer. These results are an evidence confirming the formation of BAlN alloys and the Al content increase with TMAl/III ratio.

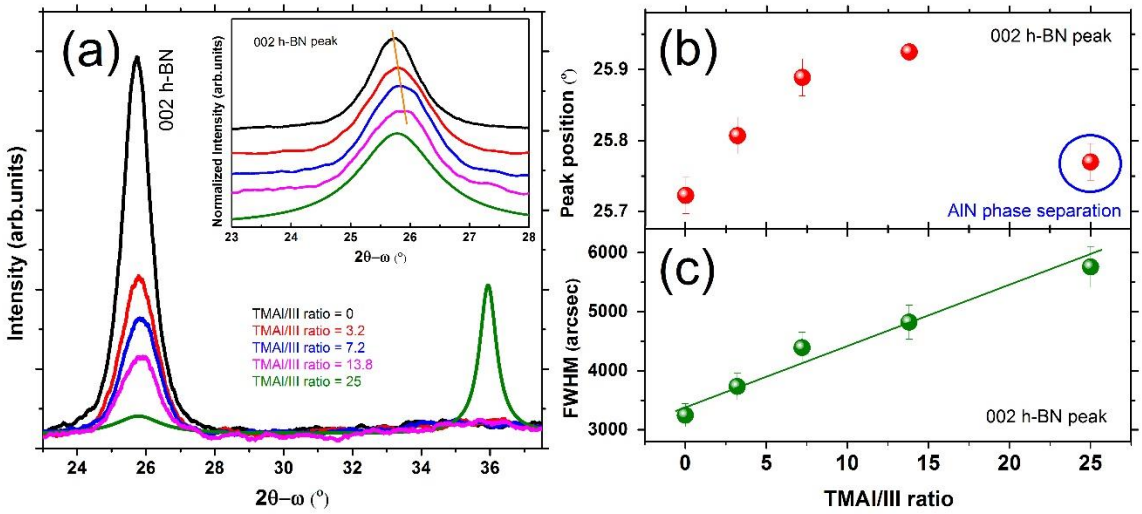

Figure 3-8: (a) High resolution X-Ray Diffraction (HR-XRD) $2\theta-\omega$ scan of the BAlN alloys grown on sapphire with five different TMAl/III ratios. The inset shows a clear shift of the 002 h-BN peak toward a higher angle. (b) and (c): the 002 peak position and FWHM as function of TMAl/III ratio, respectively.

To estimate the efficiency of Al incorporation into our BAlN alloys, secondary-ion mass spectrometry (SIMS) measurements were performed. Figure 3-9 shows SIMS elemental concentration depth profiles of aluminum atoms in BAlN alloys with five different TMAl/ III ratios. In the first 5 nm depth, there is a thin silver layer which was deposited on the top of the 20 nm thick BAlN for charge compensation purpose during the SIMS analysis, and the interface between the coated layer and BAlN alloys. The region from 20 nm to 40 nm depth is a transition zone between BAlN alloys and sapphire substrates, which give a higher value of Al concentration. Our measurements and analysis were focused in the region between 5 nm and 20 nm depth (flat part). We found that the Al concentration is increasing with the enhancement of the TMAl/III ratio from 0 to 25. At the TMAl/III ratio of 25, the Al concentration reaches the same level with the one derived from sapphire substrate (25–40 nm depth) due to the phase separation as demonstrated by HR-XRD. In this sample therefore, we may find some areas with Al rich BAlN or even pure w-AlN. We obtained the Al content of 1%, 3.5%, and 17% for the TMAl/III ratios of 3.2, 7.2, and 13.8, respectively. In the case of the TMAl/III ratio of 25, the specific value of Al content could not be evaluated accurately due to the nonhomogeneity of the layer (phase separation). Therefore, in this study the maximum composition of Al in BAlN on sapphire without phase separation is up to 17%. Compared to the theoretical value of BAlN on AlN, this experimental value is higher than 9% predicted in [21] and lower than in [22].

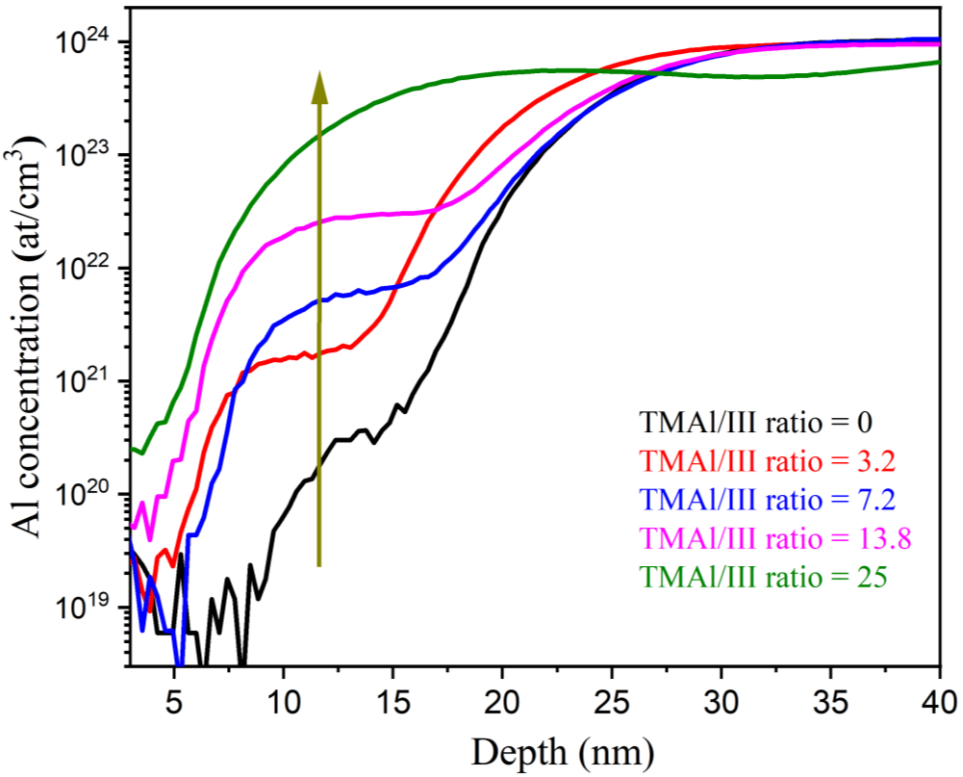

Figure 3-9: SIMS elemental concentration depth profile of Al for BAlN alloys grown on sapphire with four different TMAl/III ratios.

The growth of B rich BAlN and its fundamental properties are in its earlier stage and need still further investigation in order to growth thick and high quality BAlN layers. Therefore, the BAlN was not used for neutron detection.

In summary, we have demonstrated the incorporation of Mg into h-BN with up to $4x10^{18}$ atoms/cm^3 while maintaining the 2D nature of the layers. Conductivity of Mg-doped h-BN samples have increased with respect to Mg incorporation. An activation energy of 160 meV was obtained. Epitaxial growth of Mg-doped h-BN films on Al-rich n-AlGaN films was performed and showed diode-like I-V properties. Under UV illumination, the Mg-doped BN /n-AlGaN heterojunction produced significant photocurrent, which is very convincing evidence for the formation of a p-n junction between the Mg-doped BN and n-AlGaN films. Then, the single crystal quality of boron-rich BAlN films with Al content up to 17% was achieved, corresponding to 83% of boron atoms.

CHAPTER 7: GENERAL CONCLUSION AND PERSPECTIVES

1. Conclusion

The demand for alternative neutron detector technologies to replace helium-3 gas neutron detectors is very important due to the worldwide scarcity of helium-3, the high operating voltage and the large footprint of the device. Several solutions have already been proposed, e.g. scintillators with low neutron/gamma discrimination, silicon-based detectors coated with a neutron converter, which has limited detection efficiency. This is due to the loss of charge particles absorbed in the converter layer before reaching the Si-based p-n device. In our work, we have presented a direct neutron conversion based on boron containing III-nitride materials such as BGaN/GaN SLs, natural and ^{10}B enriched BN detectors. In this approach, neutron absorption, electron-hole pair generation and collection take place in the same layer. To further improve the charge collection, we have also investigated the p-type doping of h-BN with Mg as dopant.

BGaN/GaN SLs with a boron content of 2.8% were successfully grown and characterized. SIMS data showed an antiphase variation between boron and gallium profiles, indicating the formation of a ternary BGaN alloy. MSM and PIN devices of BGaN/GaN SLs were processed and tested under UV light and neutron flux. These devices showed high sensitivity to thermal neutrons. We have successfully grown boron-rich BAlN alloys on sapphire. The surface of BAlN alloys exhibits a morphology ranging from a fully 2-dimensional (2D) to a three-dimensional (3D) granular surface with increasing Al content. The HR -XRD study shows only a shift in the position of the reflection peak in the 002 plane to higher diffraction angles, indicating BAlN alloys with single hexagonal phase up to a TMAl/III ratio of 14. Further increase of TMAl/III ratio up to 25 resulted in phase separation. The Al composition in the BAlN layer was estimated to be up to 17%, corresponding to 83% boron atoms. We used two precursors (TEB and enriched ^{10}B TEB) to grow

2.5 µm thick natural and ^{10}B enriched BN films. SIMS analyzes confirmed the presence of 97% ^{10}B in the BN films. The enriched precursor did not affect the morphological and structural quality of the ^{10}B enriched BN films. Then, we fabricated MSM devices with 2.5 µm natural and ^{10}B-enriched h- BN films for neutron detection. The BN detectors showed high sensitivity to thermal neutrons (233% and 376% for natural and ^{10}B enriched BN). The neutron sensitivity was further improved when the detectors were biased, reaching 316 % and 1192 % at 200 V and a flux of $3x10^4$ n/cm^2/s for natural and ^{10}B enriched BN detectors, with a dark current of only 2.5 pA at 200 V bias. The neutron-induced current of the ^{10}B-enriched BN MSM detector is up to four times larger than that with natural boron. A linear neutron response of the detectors under thermal neutron flux and bias voltages was obtained. At zero bias voltage, neutron-induced current was observed on the BN MSM detectors, showing the potential for realizing self-powered thermal neutron detectors based on the highly sensitive boron material. For h-BN doping, different Cp2Mg molar flow rates were used to study the Mg incorporation in h-BN layers. HRXRD, SEM, SIMS measurements were used to characterize these h-BN layers. The van der Waals nature of the Mg-doped h-BN layers was preserved up to a certain threshold value for the Cp2Mg molar flow. The electrical conductivity of the Mg-doped h-BN layers increased with Mg concentration, demonstrating the possibility of controlling the conductivity of h- BN. We also demonstrated the epitaxial growth of Mg-doped h-BN films on Al-rich n-AlGaN films, which exhibited diode-like I-V characteristics. More importantly, illumination of the p-BN/n-AlGaN heterojunction produced significant photocurrent for the first time, which is very convincing evidence for the formation of a p-n junction between p-BN and n-AlGaN. These results are very encouraging for further research and could open potential applications in wide bandgap optoelectronic devices, such as novel neutron detectors, deep UV LEDs and deep UV lasers.

2. Perspective

The perspective of this work includes further neutron testing of MSM BGaN/GaN and PIN. For the doping of h-BN materials, further work is needed to investigate Zn doping for p-type doping, which can improve the conductivity in h-BN. Subsequently, the n-type doping of h-BN using Si dopants will be investigated in detail. Achieving good conductivity control of the n- and p-type of h-BN will enable the realization of P-N and P-I-N devices for neutron detection. These devices improve the collection of charge carriers; therefore, a high neutron current is expected compared to MSM devices based on undoped h-BN. Another important future work is the growth of thick boron-rich BAlN for neutron testing. These BAlN layers are more stable than the h-BN layers and allow a differentiated design of neutron detectors without delamination problems.

3. Publications

1. **Mballo A**., Ahaitouf A., Sundaram S., Srivastava A., Ottapilakkal V., Gujrati R., Vuong Ph., Karrakchou S., Li X., Halfaya Y., Gautier S., Voss P.L, Salvestrini J-P. and Ougazzaden A. Natural boron and 10B-enriched hexagonal Boron Nitride for high sensitivity self-biased Metal-Semiconductor-Metal neutron detectors. *ACS Omega*. 10.1021/acsomega.1c05458.
2. **Mballo, A**.; Srivastava, A.; Sundaram, S.; Vuong, P.; Karrakchou, S.; Halfaya, Y.; Gautier, S.; Voss, P. L.; Ahaitouf, A.; Salvestrini, J. P.; et al. Towards P-Type Conduction in Hexagonal Boron Nitride: Doping Study and Electrical Measurements Analysis of h-BN/AlGaN Heterojunctions. *Nanomaterials*, **2021**, *11* (1), 211.
3. Ayari, T.; Sundaram, S.; Bishop, C.; **Mballo, A**.; Vuong, P.; Halfaya, Y.; Karrakchou, S.; Gautier, S.; Voss, P. L.; Salvestrini, J. P.; et al. Novel Scalable Transfer Approach for Discrete III-Nitride Devices Using Wafer-Scale Patterned H-BN/Sapphire Substrate for Pick-and-Place Applications. *Adv. Mater. Technol.* **2019**, *1900164*, 1900164.
4. Sama, N. Y.; Hathcock, A.; He, D.; Quynh, T.; **Mballo, A.** et al. Investigation of Sc 2 O 3 Based All-Solid-State EIS Structure for AlGaN / GaN HEMT PH Sensor. *2019 Ieee Sensors* **2019**, No. 1, 1–4.
5. Vuong, P.; **Mballo, A**.; Sundaram, S.; Patriarche, G.; Halfaya, Y.; Karrakchou, S.; Srivastava, A.; Krishnan, K.; Sama, N. Y.; Ayari, T.; et al. Single Crystalline Boron Rich B(Al)N Alloys Grown by MOVPE. *Appl. Phys. Lett.* **2020**, *116* (4), 1–6.
6. Karrakchou, S.; Sundaram, S.; Ayari, T.; **Mballo, A**.; Vuong, P.; Srivastava, A.; Gujrati, R.; Ahaitouf, A.; Patriarche, G.; Leichlé, T.; et al. Effectiveness of selective area growth using van der Waals h-BN layer for crack-free transfer of large-size III-N devices onto arbitrary substrates. *Sci. Rep.* **2020**, *10*, 1–9.

7. Vuong, P.; Sundaram, **S.; Mballo**, A.; Patriarche, G.; Leone, S.; Benkhelifa, F.; Karrakchou, S.; Moudakir, T.; Gautier, S.; Voss, P.L.; et al. Control of the Mechanical Adhesion of III-V Materials Grown on Layered h-BN. *ACS Appl. Mater. Interfaces* **2020**, *12*, 55460-55466.
8. Sundaram, S.; Voss, P. L.; Vuong, P.; **Mballo, A**.; et al. MOVPE of GaN-Based Mixed Dimensional Heterostructures on Wafer-Scale Layered 2D Hexagonal Boron Nitride - A Key Enabler of III-Nitride Flexible Optoelectronics MOVPE of GaN-Based Mixed Dimensional Heterostructures on Wafer-Scale Layered 2D Hexagonal Boron Nitride-A Key Enabler of III-Nitride Flexible Optoelectronics. **2021**, *061101*.
9. Daldoul, I.; Othmani, S.; **Mballo, A.**; Vuong, P.; Salvestrini, J.P.; Chaaben, N. Growth and characterization of cubic GaN grown on GaAs (110) substrate by MOVPE. *Mater. Sci. Semicond. Process.* **2021**, *132*.
10. Karrakchou, S.; Sundaram, S.; Gujrati, R.; Vuong, P.; **Mballo, A**.; Adjmi, H.E.; Ottapilakkal, V.; El Huni, W.; Bouzid, K.; Patriarche, G.; et al. Monolithic Free-Standing Large-Area Vertical III-N Light-Emitting Diode Arrays by One-Step h-BN-Based Thermomechanical Self-Lift-Off and Transfer. *ACS Appl. Electron. Mater.* **2021**, *3*, 2614-2621.
11. Vuong , Phuong; Sundaram, Suresh; Optappilakkal, Vishnu; Patriarche, Gilles; Largeau, Ludovic; Srivastava, Ashutosh; **Mballo, Adama**; Moudakir, Tarik; Gautier, Simon; Voss, Paul; Salvestrini, Jean Paul; Ougazzaden, Abdallah "Influence of sapphire substrate orientation on van der Waals epitaxy of III-Nitrides on two-dimensional h-BN" ACS Applied Nano Materials, 2021.

Conferences

1. Adama Mballo, Ashutosh Srivastava, Suresh Sundaram, Phuong Vuong, Soufiane Karrakchou, Yacine Halfaya, Simon Gautier, Ali Ahaitouf, Paul L. Voss, Jean Paul Salvestrini and Abdallah Ougazzaden, Study of P-Type Doping of Hexagonal Boron Nitride Grown by MOCVD ICNS-13 (2019)
2. MRS Fall 2021: Investigations on p-type Doping of Layered Hexagonal Boron Nitride Grown by MOVPE, poster presentation.

REFERENCES:

References for chapter 1

1. A. Owen, Semiconductor Radiation Detectors, CRC Press, p 323-338, (2019).
2. M. B. Chadwick et al ENDF/B-VII.0: next generation evaluated nuclear data library for nuclear science and technology Nucl. Data Sheets 107, 2931–3060, (2006).
3. G. F. Knoll, "Radiation detection and measurement," 4th edition, (John Wiley & Sons), (2010).
4. https://techlinkcenter.org/news/helium-3-is-scarce-this-navy-invention-stretches-it-for-radiation-detectors
5. A. Maity, S.J. Grenadier, J. Li, J.Y. Lin, and H.X. Jiang, J. Appl. Phys. 123, (2018).
6. T.C. Doan, J. Li, J.Y. Lin, and H.X. Jiang, AIP Adv. 6, 1 (2016).
7. T. D. Cradduck. Fundamentals of scintillation counting. In: Seminars in nuclear medicine: Elsevier, 205-223, (1973)
8. M. Wielunski, R. Schütz, E. Fantuzzi, A. Pagnamenta, W. Wahl, J. Palfálvi, P. Zombori, A. Andrasi, H. Stadtmann and C.H.. Schmitzer, Nucl. Instrum. Methods Phys Res A, 517, (2004).
9. K.-C. Huang, R. Dahal, J.-Q. Lu, Y. Danon, I. B. Bhat, Transactions of the American Nuclear Society, Chicago, Illinois,106, (2012)
10. H. Kitaguchi, et al., "Silicon semiconductor detectors for various nuclear radiations," Nucl. Sci., IEEE Transactions on, 43, 1846 - 1850, (1996).
11. Y. Kubota, K. Watanabe, O. Tsuda, and T. Taniguchi, Science (932-934), **317**, 932 (2007).
12. A. Miyake, T. Nishioka, S. Singh, H. Morii, H. Mimura, T. Aoki, Nucl. Instr. and Meth., 654,1 (2011).
13. D.S. McGregor, J.T. Lindsay, R.W. Olsen, Nucl. Instr. and Meth., A381 (1996).
14. Z.W. Bell, K.R. Pohl, L. van Den Berg, "Neutron detection with mercuric iodide", IEEE Trans. Nucl. Sci., 51 (2004).

15. K. Watanabe, T. Taniguchi, and H. Kanda, Nat. Mater. 3, 404 (2004).

16. H.X. Jiang and J.Y. Lin, ECS J. Solid State Sci. Technol. **6**, Q3012 (2017).

17. D.S. McGregor, T.C.Unruh, W.J. McNeil, Nucl. Instr. Methods Res. A. A591 (2008).

18. J. Li, R. Dahal, S. Majety, J.Y. Lin, and H.X. Jiang, Nucl. Instrum. Methods Phys. Res. Sect. A. 654, 417 (2011).

19. T.C. Doan, S. Majety, S. Grenadier, J. Li, J.Y. Lin, and H.X. Jiang, Nucl. Instrum. Methods Phys. Res. Sect. A. 783, 121 (2015).

20. A. Maity, S.J. Grenadier, J. Li, J.Y. Lin, and H.X. Jiang, Appl. Phys. Lett. 114, (2019).

21. J. Li, A. Maity, S. J. Grenadier, J. Y. Lin, and H. X. Jiang, Appl. Phys. Lett. 118, 092102 (2021).

22. S. Gautier, C. Sartel, S. Ould-Saad, J. Martin, A. Sirenko, and A. Ougazzaden, J. Cryst. Growth 298, 428 (2007).

23. X. Li, S. Sundaram, Y. El Gmili, T. Moudakir, F. Genty, S. Bouchoule, G. Patriarche, R.D. Dupuis, P.L. Voss, J.P. Salvestrini, and A. Ougazzaden, Phys. Status Solidi Appl. Mater. Sci. 212, 745 (2015).

24. X. Li, S. Sundaram, Y. El Gmili, F. Genty, S. Bouchoule, G. Patriache, P. Disseix, F. R´everet, J. Leymarie, J.-P. Salvestrini, R. Dupuis, P. Voss, and A. Ougazzaden, J. Cryst. Growth, 414, (2015).

25. G. Orsal, N. Maloufi, S. Gautier, M. Alnot, A.A. Sirenko, M. Bouchaour, and A. Ougazzaden, J. Cryst. Growth 310, 5058 (2008).

26. M. Abid, T. Moudakir, G. Orsal, S. Gautier, A. E. Naciri, Z. Djebbour, J.-H. Ryou, G. Patriarche, L. Largeau, H. J. Kim, Z. Lochner, K. Pantzas, D. Alamarguy, F. Jomard, R. D. Dupuis, J.-P. Salvestrini, P. L. Voss, and A. Ougazzaden, Appl. Phys. Lett. 100, 051101 (2012).

27. S. Gautier, C. Sartel, S. O. S. Hamady, N. Maloufi, J. Martin, F. Jomard, and A. Ougazzaden, Superlattices Microstruct. 40, 233 (2006).

28. A. Ougazzaden, S. Gautier, T. Moudakir, Z. Djebbour, Z. Lochner, S. Choi, H. J. Kim, J.-H. Ryou, R. D. Dupuis, and A. A. Sirenko, Appl. Phys. Lett. 93, 083118 (2008).

29. K. Atsumi, Y. Inoue, H. Mimura, T. Aoki, and T. Nakano, APL Mater. 2, 1 (2014).

30. A. Ougazzaden, S. Gautier, C. Sartel, N. Maloufi, J. Martin, and F. Jomard, J. Cryst. Growth 298, 316 (2007).

31. S. Gautier, G. Patriarche, T. Moudakir, M. Abid, G. Orsal, K. Pantzas, D. Troadec, A. Soltani, L. Largeau, O. Mauguin, and A. Ougazzaden, J. Cryst. Growth 315, 288 (2011).

32. C. Attaccalite, M. Bockstedte, A. Marini, A. Rubio, and L. Wirtz, Phys. Rev. B - Condens. Matter Mater. Phys. 83, 1 (2011).

33. D.A. Laleyan, S. Zhao, S.Y. Woo, H.N. Tran, H.B. Le, T. Szkopek, H. Guo, G.A. Botton, and Z. Mi, Nano Lett. 17, 3738 (2017).

34. M.O. Watanabe, S. Itoh, K. Mizushima, and T. Sasaki, J. Appl. Phys. 78, 2880 (1995).

35. M.R. Uddin, J. Li, J.Y. Lin, and H.X. Jiang, Appl. Phys. Lett. 110, 2 (2017).

36. M. Lu, A. Bousetta, A. Bensaoula, K. Waters, and J.A. Schultz, Appl. Phys. Lett. 622, 622 (1995).

37. B. He, W.J. Zhang, Z.Q. Yao, Y.M. Chong, Y. Yang, Q. Ye, X.J. Pan, J.A. Zapien, I. Bello, S.T. Lee, I. Gerhards, H. Zutz, and H. Hofsäss, Appl. Phys. Lett. 95, 2 (2009).

38. F. Sun, Z. Hao, G. Liu, C. Wu, S. Lu, S. Huang, C. Liu, Q. Hong, X. Chen, D. Cai, and J. Kang, Nanoscale 10, 4361 (2018).

39. R. Dahal, J. Li, S. Majety, B.N. Pantha, X.K. Cao, J.Y. Lin, and H.X. Jiang, Appl. Phys. Lett. 98, 88 (2011).

40. L. Weston, D. Wickramaratne, and C.G. Van de Walle, Phys. Rev. B 96, 100102 (2017).

References chapter 2

1. J. Orton and C. Foxon, Reports on Progress in Physics, 61, 1, (1998).
2. M. R. Krames, O. B. Shchekin, R. Mueller-Mach, G. O. Mueller, L. Zhou, G. Harbers, M. G. Craford, J. Disp. Technol., 3, 2, (2007).
3. S. Nakamura, Solid State Commun. 102, 2-3, (1997).

4. K. Ohkawa, T. Watanabe, M. Sakamoto, A. Iiirako, and M. Deura, J. Cryst. Growth, 343, 1, (2012).
5. S. Nakamura, S. Pearton, G. Fasol, Springer, (2000).
6. E. Munoz, E. Monroy, J. Pau, F. Calle, F. Omnes, and P. Gibart, 13, 32,(2001)
7. E. Monroy, F. Omnes, and F. Calle, Semicond. Sci. Technol., 18, 4, (2003).
8. M. Khan, M. Shatalov, H. Maruska, H. Wang, and E. Kuokstis, Jpn. J. Appl. Phys. 44, 10, (2005).
9. U. Mishra, Y. Wu, B. Keller, S. Keller, and S. Denbaars, IEEE Trans. Microwave Theory Tech., 46, 6, (1997).
10. S. Sheppard, K. Doverspike, W. Pribble, S. Allen, J. Palmour, L. Kehias, and T. Jenkins, IEEE Electron Device Lett., 20, 4, (1999).
11. B. Green, K. Chu, E. Chumbes, J. Smart, J. Shealy, and L. Eastman, IEEE Electron Device Lett., 21, 6, (2000).
12. R. Vetury, N. Zhang, S. Keller, and U. Mishra, IEEE Transactions on Electron Devices, 48, 3, (2001).
13. Y. Wu, D. Kapolnek, J. Ibbetson, P. Parikh, B. Keller, and U. Mishra, IEEE Transactions on Electron Devices, 48, 3, (2001).
14. J. Kuzmik, IEEE Electron Device Lett., 22, 11,(2001).
15. R. A. Ferreyra, C. Zhu, A. Teke, and H. Morkoç, in Springer Handbook of Electronic and Photonic Materials, S. Kasap and P. Capper, Eds. Cham: Springer International Publishing, (2017)
16. M. Shatalov, J. Zhang, A. S. Chitnis, S. Member, V. Adivarahan, J. Yang, G. Simin, and M. A. Khan, IEEE Journal of Selected Topics in Quantum Electronics, 8, 2, (2002).
17. V. Srikant, J. S. Speck, D. R. Clarke, J. Appl. Phys. 82, 4286, (1997).
18. T. Metzger, R. Hopler, E. Born, O. Ambacher, M. Stutzmann, R. Stommer, M. Schuster, H. Gobel, S. Christiansen, M. Albrecht, H. P. Strunk, Philos. Mag. A 77 1013 (1998).
19. H. Heinke, V. Kirchner, S. Einfeldt, D. Hommel, X-ray diffraction analysis of the defect structure in epitaxial gan, Appl. Phys. Lett. 77 (2000) 2145.
20. Y. J. Sun, O. Brandt, T. Y. Liu, A. Trampert, K. H. Ploog, Appl. Phys. Lett. 81, 4928, (2002).
21. R. Chierchia, T. Bottcher, H. Heinke, S. Einfeldt, S. Figge, D. Hommel, J. Appl. Phys. 93, 8918, (2003).

22. A. Costales, M. A. Blanco, Á. Martín Pendás, A. K. Kandalam, and R. Pandey, J. Am. Chem. Soc., 124, 15, (2002).
23. A. R. Denton and N. W. Ashcroft, Physical Review A, 43, 6, (1991).
24. A. Ougazzaden, S. Gautier, T. Moudakir, Z. Djebbour, Z. Lochner, S. Choi, H. J. Kim, J.-H. Ryou, R. D. Dupuis, and A. A. Sirenko, Appl. Phys. Lett., 93, 083118, (2008).
25. S. Azzi, A. Zaoui, and M. Ferhat, Solid State Communications, 144, (2007).
26. I. Vurgaftman, J. R. Meyer, and L. R. Ram-Mohan, J. Appl. Phys., 89, 11, (2001).
27. J. M. Lopes, Prog. Cryst. Growth Charact. Mater. 67, 2 (2021).
28. G. Cassabois, P. Valvin, and B. Gil, Nat. Photonics 10, 262 (2016).
29. P. Vuong, G. Cassabois, P. Valvin, V. Jacques, A. V. D. Lee, A. Zobelli, K. Watanabe, T. Taniguchi, B. Gil, 2D Mater. 4, 011004, (2017).
30. Elias, C.; Valvin, P.; Pelini, T.; Summer, A.; Mellor, C. J.; Cheng, T. S.; Eaves, L.; Foxon, C. T.; Beton, P. H.; Novikov, S. V; et al. Direct Band-Gap Crossover in Epitaxial Monolayer Boron Nitride. No. 2019, 1–7.
31. C. Elias, P. Valvin, T. Pelini, A. Summer, C.J. Mellor, T.S. Cheng, L. Eaves, C.T. Foxon, P.H. Beton, S. V Novikov, B. Gil, and G. Cassabois, Nat. commun.,10, 2639, (2019).
32. X. Zhang, J. Meng, Mater. Today, 347, 419 (2019).
33. D. Pacilé, J. C. Meyer, Ç. Ö. Girit, and A. Zettl, Appl. Phys. Lett. 92, 133107 (2008).
34. L. Song, L. Ci, H. Lu, P. B. Sorokin, C. Jin, J. Ni, A. G. Kvashnin, D. G.Kvashnin, J. Lou, B. I. Yakobson, and P. M. Ajayan, Nano Lett. 10, 3209 (2010).
35. V. Siklitsky, "boron nitride," http://www.ioffe.rssi.ru/SVA/NSM/Semicond/BN/index.html.
36. K. Nakamura, Preparation and Properties of Boron Nitride Films by Metal Organic Chemical Vapor Deposition, J. Electrochem. Soc. 133, 1120, (1986).
37. M. B. Chadwick et al ENDF/B-VII.0: next generation evaluated nuclear data library for nuclear science and technology Nucl. Data Sheets 107, 2931–3060, (2006)
38. R.H. Wentorf, Cubic form of boron nitride, J. Chem. Phys. 26, 956, (1957).
39. R.H. Wentorf, J. Chem. Phys. 34, 809, (1961).
40. T. Taniguchi, S. Yamaoka, Rev. High Press. Sci. Technol. 7, 980, (1998).
41. K.K. Kim, A. Hsu, X. Jia, S.M. Kim, Y. Shi, M. Hofmann, D. Nezich, J.F. Rodriguez- Nieva, M. Dresselhaus, T. Palacios, J. Kong, Synthesis of Monolayer Hexagonal Boron Nitride on Cu Foil Using Chemical Vapor Deposition, Nano Lett. 12, 161, (2012).

42. Y. Kobayashi, T. Akasaka, T. Makimoto, Hexagonal boron nitride grown by MOVPE, J. Cryst. Growth 310, 5048, (2008).
43. Y. Kobayashi, T. Nakamura, T. Akasaka, T. Makimoto, N. Matsumoto, Hexagonal boron nitride on Ni (111) substrate grown by flow-rate modulation epitaxy, J. Cryst. Growth 298, 325, (2007).
44. Y. Kobayashi, H. Hibino, T. Nakamura, T. Akasaka, T. Makimoto, N. Matsumoto, Boron Nitride Thin Films Grown on Graphitized 6H–SiC Substrates by Metalorganic Vapor Phase Epitaxy, Jpn. J. Appl. Phys. 46, 2554, (2007).
45. Y. Kobayashi, T. Akasaka, Hexagonal BN epitaxial growth on (0001) sapphire substrate by MOVPE, J. Cryst. Growth, 310, 5044, (2008).
46. X. Li, S. Sundaram, Y. El Gmili, T. Ayari, R. Puybaret, G. Patriarche, P.L. Voss, J. P. Salvestrini, A. Ougazzaden, Cryst. Growth Des. 16, 3409, (2016).
47. H. M. Manasevit, Appl. Phys. Lett., 12, 4, (1968).
48. A. Ougazzaden, S. Gautier, C. Sartel, N. Maloufi, J. Martin, and F. Jomard, J. Cryst. Growth 298, 316 (2007).
49. M. Kurimoto, T. Takano, J. Yamamoto, Y. Ishihara, M. Horie, M. Tsubamoto, and H. Kawanishi, J. Cryst. Growth 221, 378 (2000).
50. S. Sakai, Y. Ueta, Y. Terauchi, Jpn. J. Appl. Phys. 32, 4413, (1993).
51. M. Abid, T. Moudakir, Z. Djebbour, G. Orsal, S. Gautier, A. En Naciri, A. Migan-Dubois, and A. Ougazzaden, J. Cryst. Growth 315, (2011)
52. V. Ravindran, M. Boucherit, A. Soltani, S. Gautier, T. Moudakir, J. Dickerson, P. L. Voss, M.-A. di Forte-Poisson, J.-C. De Jaeger, and A. Ougazzaden, Appl. Phys. Lett. 100, 243503 (2012)
53. C. Bishop, J. P. Salvestrini, Y. Halfaya, S. Sundaram, Y. El Gmili, L. Pradere, J. Y. Marteau, M. B. Assouar, P. L. Voss, and A. Ougazzaden, Appl. Phys. Lett. 106, 243504 (2015).
54. S. Gautier, C. Sartel, S. Ould-Saad, J. Martin, A. Sirenko, and A. Ougazzaden, J. Cryst. Growth 298, 428 (2007).
55. X. Li, S. Sundaram, Y. El Gmili, T. Moudakir, F. Genty, S. Bouchoule, G. Patriarche, R.D. Dupuis, P.L. Voss, J.P. Salvestrini, and A. Ougazzaden, Phys. Status Solidi Appl. Mater. Sci. 212, 745 (2015).

56. X. Li, S. Sundaram, Y. El Gmili, F. Genty, S. Bouchoule, G. Patriache, P. Disseix, F. R´everet, J. Leymarie, J.-P. Salvestrini, R. Dupuis, P. Voss, and A. Ougazzaden, J. Cryst. Growth, 414, (2015).
57. X. Li, M.B. Jordan, T. Ayari, S. Sundaram, Y. El Gmili, S. Alam, M. Alam, G. Patriarche, P.L. Voss, J. Paul Salvestrini, and A. Ougazzaden, Sci. Rep. 7, 1 (2017).
58. G. B. Stringfellow, Academic Press, (1999).
59. F. Scholz, Compound Semiconductors, Script for Summer Semester, Institute of Optoelectronics, University of Ulm, (2012).
60. A. Mircea, A. Ougazzaden, and R. Mellet, Prog. Cryst. Growth Charact., 19, 1, (1989).
61. ''https://myscope.training/#/SEMlevel_3_1.''
62. "http://en.wikipedia.org/wiki/Atomic force microscopy.
63. Veeco Instruments Inc., "A Practical Guide to Scanning Probe Microscopy (SPM)," tech. rep., (2005).
64. "http://en.wikipedia.org/wiki/Secondary ion mass spectrometry."
65. ''https://probion.fr/fr/les-techniques''
66. ''http://en.wikipedia.org/wiki/Scanning transmission electron microscopy.''
67. K. Pantzas, G. Patriarche, D. Troadec, S. Gautier, T. Moudakir, S. Suresh, L. Largeau, O. Mauguin, P. L. Voss, and A. Ougazzaden, Nanotech- nology, 23,455707, (2012).

References for chapter 3

1. C. Bishop, J. P. Salvestrini, Y. Halfaya, S. Sundaram, Y. El Gmili, L. Pradere, J. Y. Marteau, M. B. Assouar, P. L. Voss, and A. Ougazzaden, Appl. Phys. Lett. 106, 243504 (2015).
2. X. Li, S. Sundaram, Y. El Gmili, F. Genty, S. Bouchoule, G. Patriache, P. Disseix, F. R´everet, J. Leymarie, J.-P. Salvestrini, R. Dupuis, P. Voss, and A. Ougazzaden, J. Cryst. Growth, 414, (2015).
3. A. Ougazzaden, S. Gautier, C. Sartel, N. Maloufi, J. Martin, and F. Jomard, J. Cryst. Growth 298, 316 (2007).
4. S. Gautier, G. Patriarche, T. Moudakir, M. Abid, G. Orsal, K. Pantzas, D. Troadec, A. Soltani, L. Largeau, O. Mauguin, and A. Ougazzaden, J. Cryst. Growth 315, 288 (2011).

5. X. Li, M.B. Jordan, T. Ayari, S. Sundaram, Y. El Gmili, S. Alam, M. Alam, G. Patriarche, P.L. Voss, J. Paul Salvestrini, and A. Ougazzaden, Sci. Rep. 7, 1 (2017).
6. Y. Kobayashi, T. Makimoto, Jpn. J. Appl. Phys. 45, 4, (2006).

References for chapter 4

1. A. Maity, S.J. Grenadier, J. Li, J.Y. Lin, and H.X. Jiang, J. Appl. Phys. 123, (2018).
2. H. Wang, Y. Hong, Z. Chen, C. Lao, Y. Lu, Z. Yang, Y. Zhu and X. Liu, Nano express, 15, 176 (2020).
3. T.C. Doan, S. Majety, S. Grenadier, J. Li, J.Y. Lin, and H.X. Jiang, Nucl. Instrum. Methods Phys. Res. Sect. A. 783, 121 (2015).
4. Many, J. Phys. Chem. Solids 26, 575 (1965).
5. T.C. Doan, J. Li, J.Y. Lin, and H.X. Jiang, AIP Adv. 6, 1 (2016).
6. S. Narushima, H. Mizoguchi, K.I. Shimizu, K. Ueda, H. Ohta, M. Hirano, T. Kamiya, and H. Hosono, Adv. Mater. 15, 1409 (2003).
7. DAVID WOOD, Optoelectronic Semiconductor Devices, Prentice-Hall, 550, (1994).
8. G. Woan, the Cambridge Handbook of Physics Formulas. Cambridge University Press. ISBN 978-0-521-57507-2(2010).
9. Yaping Dan et al., ACS Photonics, 5, 4111−4116 (2018)
10. L. Wang, Z. Ju, J. Zhang, J. Zheng, D. Shen, B. Yao, D. Zhao, Z. Zhang, B. Li and C. Shan, Appl. Phys. Lett., 95,131113, (2009).
11. Q. Zheng, F. Huang, K. Ding, J. Huang, D. Chen, Z. Zhan and Z. Lin, Appl. Phys. Lett., 98, 221112, (2011).
12. M.A. Romero, L.E.M. de Barros, and P.R. Herczfeld, IEEE MTT-S Int. Microw. Symp. Dig. 3, 1505 (1994).
13. L. Su, W. Yang, J. Cai, H. Chen, and X. Fang, Small 13, 1 (2017).
14. I.K. Moon, B. Ki, S. Yoon, J. Choi, and J. Oh, Nat. Publ. Gr. 1 (2016).
15. Huang, K. Chen, and C. Chang, Ceram. Int. 1 (2020).

16. H. Chen, K. Liu, X. Chen, Z. Zhang, and M. Fan, J. Mater. Chem. C Mater. Opt. Electron. Devices 2, 9689 (2014).

17. O. Katz, V. Garber, B. Meyler, G. Bahir, and J. Salzman, Appl. Phys. Lett. 79, 1417 (2001).

References chapter 5

1. J. Li, R. Dahal, S. Majety, J.Y. Lin, and H.X. Jiang, Nucl. Instrum. Methods Phys. Res. Sect. A. 654, 417 (2011).
2. L. Sang, M. Liao, Y. Koide, and M. Sumiya, Appl. Phys. Lett. 99, 031115 (2011).
3. S. K. Zhang, W. B. Wang, I. Shtau, F. Yun, L. He, H. Morkoc, X. Zhou, M. Tamargo, and R. R. Alfano, Appl. Phys. Lett. 81, 4862 (2002).
4. M. Abid, T. Moudakir, Z. Djebbour, G. Orsal, S. Gautier, A. En Naciri, A. Migan-Dubois, and A. Ougazzaden, "Blue–violet boron-based distributed Bragg reflectors for VCSEL application," J. Cryst. Growth **315**, 283–287 (2011)
5. V. Ravindran, M. Boucherit, A. Soltani, S. Gautier, T. Moudakir, J. Dickerson, P. L. Voss, M.-A. di Forte-Poisson, J.-C. De Jaeger, and A. Ougazzaden, Appl. Phys. Lett. 100, 243503 (2012)
6. C. Bishop, J. P. Salvestrini, Y. Halfaya, S. Sundaram, Y. El Gmili, L. Pradere, J. Y. Marteau, M. B. Assouar, P. L. Voss, and A. Ougazzaden, Appl. Phys. Lett. 106, 243504 (2015).

References for chapter 6

1. H.X. Jiang and J.Y. Lin, ECS J. Solid State Sci. Technol. **6**, Q3012 (2017).
2. M. Snure, Q. Paduano, and A. Kiefer, J. Cryst. Growth 436, 16 (2016).
3. Q. Paduano, M. Snure, D. Weyburne, A. Kiefer, G. Siegel, and J. Hu, J. Cryst. Growth 449, 148 (2016).
4. X. Yang, S. Nitta, K. Nagamatsu, S.Y. Bae, H.J. Lee, Y. Liu, M. Pristovsek, Y. Honda, and H. Amano, J. Cryst. Growth 482, 1, (2018).

5. D. Chugh D, J. Wong-Leung ,L. Li, M. Lysevych, H.H Tan and C. Jagadish, 2D Mater., 5, (2018).
6. X. Li, M.B. Jordan, T. Ayari, S. Sundaram, Y. El Gmili, S. Alam, M. Alam, G. Patriarche, P.L. Voss, J. Paul Salvestrini, and A. Ougazzaden, Sci. Rep. 7, 1 (2017).
7. F. Sun, Z. Hao, G. Liu, C. Wu, S. Lu, S. Huang, C. Liu, Q. Hong, X. Chen, D. Cai, and J. Kang, Nanoscale 10, 4361 (2018).
8. C. Bayram, J.L. Pau, R. McClintock, and M. Razeghi, J. Appl. Phys. 104, 1 (2008).
9. M. Lachab, D.H. Youn, R.S. Qhalid Fareed, T. Wang, and S. Sakai, Solid. State. Electron. 44, 1669 (2000).
10. C.C. Hsu, J.S. Yuan, R.M. Cohen, and G.B. Stringfellow, J. Cryst. Growth 74, 535 (1986).
11. H. Henck, D. Pierucci, Z. Ben Aziza, M.G. Silly, B. Gil, F. Sirotti, G. Cassabois, and A. Ouerghi, Appl. Phys. Lett. 110, (2017).
12. A. Maity, S.J. Grenadier, J. Li, J.Y. Lin, and H.X. Jiang, J. Appl. Phys. 123, (2018).
13. C. Steinborn, M. Herrmann, U. Keitel, A. Schönecker, J. Räthel, D. Rafaja, and J. Eichler, J. Eur. Ceram. Soc. 33, 1225 (2013).
14. Dahal, R.; Li, J.; Majety, S.; Pantha, B.N.; Cao, X.K.; Lin, J.Y.; Jiang, H.X. Appl. Phys. Lett., 98, (2011).
15. S. Majety, J. Li, X.K. Cao, R. Dahal, B.N. Pantha, J.Y. Lin, and H.X. Jiang, Appl. Phys. Lett. 100, 0 (2012).
16. M. Lu, A. Bousetta, A. Bensaoula, K. Waters, and J.A. Schultz, Appl. Phys. Lett. 622, 622 (1995).
17. S. Narushima, H. Mizoguchi, K.I. Shimizu, K. Ueda, H. Ohta, M. Hirano, T. Kamiya, and H. Hosono, Adv. Mater. 15, 1409 (2003).
18. G.D. Hao, S. Tsuzuki, and S. ichiro Inoue, Appl. Phys. Lett. 114, 1 (2019).
19. X. Li, S. Sundaram, Y. El Gmili, T. Ayari, R. Puybaret, G. Patriarche, P.L. Voss, J.P. Salvestrini, and A. Ougazzaden, Cryst. Growth Des. 16, 3409 (2016).
20. X. Li, S. Sundaram, Y. El Gmili, T. Moudakir, F. Genty, S. Bouchoule, G. Patriarche, R.D. Dupuis, P.L. Voss, J.P. Salvestrini, and A. Ougazzaden, Phys. Status Solidi Appl. Mater. Sci. 212, 745 (2015).

21. Y. Hasegawa, T. Akiyama, A.-M. Pradipto, K. Nakamura, and T. Ito, Jpn. J. Appl. Phys., Part 1 58, SCCB21 (2019).
22. T. Akiyama, K. Nakamura, and T. Ito, Appl. Phys. Express 11, 025501 (2018).

RESUME

Introduction générale

Les détecteurs de neutrons jouent un rôle crucial dans de nombreux domaines tels que la sécurité (aux frontières et dans les aéroports) à travers le contrôle des activités illicites des matériaux nucléaires, la surveillance des rayonnements neutroniques dans les centrales nucléaires, l'instrumentation de mesures en physique des hautes énergies, et en sciences nucléaires, etc. En outre, des événements récents tels que l'explosion de Fukushima et l'empoisonnement au polonium ont stimulé l'intérêt pour le développement de petits détecteurs de neutrons à base semi-conducteurs (DNS), portables et peu coûteux. Pour atteindre une efficacité élevée dans les DNS, des facteurs tels que l'absorption des neutrons et la collecte des charges (électrons et trous) sont essentiels.

L'objectif général de ce travail est de développer des détecteurs de neutrons thermiques efficaces à partir de nitrures d'éléments III contenant du bore tels que le nitrure de bore (BN) et les alliages de BGaN. Ces matériaux sont très prometteurs pour les applications de détection des neutrons en raison de la section efficace de capture des neutrons de l'isotope 10 du bore (^{10}B) et de leur faible sensibilité aux rayons gamma. Cependant, le principal défi que pose les matériaux III-N contenant du bore pour la détection des neutrons est leur qualité de synthèse proprement dite. Par exemple, la synthèse de BGaN monocristallin épais avec une teneur importante en bore, nécessaire pour les détecteurs de neutrons, est très difficile avec la méthode MOVPE en raison des dégradations telles que la séparation de phase et la formation d'une morphologie 3D. Nous avons donc développé une approche innovante consistant en la croissance de super-réseaux (SLs) BGaN/GaN avec une teneur en bore de 3% dans la couche BGaN. Ces matériaux BGaN/GaN SLs

ont été utilisés pour fabriquer des dispositifs MSM et PIN, qui ont montré un signal significatif induit par les neutrons. Même avec cette approche, nous avons constaté la subsistance d'un certain nombre de limites relatives à la teneur en bore, la qualité du matériau et l'épaisseur globale, qui sont des facteurs importants pour la réalisation de détecteurs de neutrons à haute efficacité.

L'utilisation de couches épitaxiales de BN (100 % de bore) devrait permettre d'améliorer l'absorption des neutrons thermiques et les performances des détecteurs de neutrons. Notre groupe de recherche est le premier à développer des films de h-BN en couches 2D de grande surface et de haute qualité cristalline sur un substrat de saphir par la méthode MOVPE. Ces films de BN ont été utilisés pour réaliser des photodétecteurs UV. Dans ce travail, nous avons synthétisé des échantillons de BN naturel et enrichi en ^{10}B d'une épaisseur allant jusqu'à 2.5µm et les avons utilisés pour fabriquer des détecteurs MSM. Les avantages des structures MSM se traduisent par la possibilité de réaliser un fonctionnement autonome, similaire à celui démontré pour les photodétecteurs UV, et le gain interne permettant d'augmenter le signal neutronique.

Ce travail vise également à étudier le dopage du BN en utilisant Mg comme dopant dans l'objectif de réaliser dans le futur, des détecteurs de neutrons BN à base de jonction p-n. Comme une teneur élevée en bore est hautement souhaitable pour les détecteurs de neutrons, nous avons aussi exploré expérimentalement un nouveau matériau : les alliages BAlN riches en bore.

Le rapport de thèse est composé de 7 chapitres :

Le chapitre 1 présente les types de détecteurs de neutrons, y compris l'état de l'art et les problèmes associés aux différentes technologies (détecteurs remplis de gaz, détecteurs de neutrons à base de scintillateurs et à base de semi-conducteurs).

Le chapitre 2 présente les propriétés de base des nitrures d'éléments III. Une brève introduction des techniques et équipements utilisés pour la synthèse et la caractérisation de ces matériaux est également présentée.

Le chapitre 3 est consacré à la synthèse des matériaux BGaN/GaN SLs et de BN par la méthode MOVPE. Tout d'abord, les résultats d'analyses de la croissance de structures de super-réseaux BGaN/GaN à longue période (constituées de BGaN de 20 nm d'épaisseur et de GaN de 20 nm d'épaisseur répétées 11 fois) sont rapportés. Ensuite, la croissance de BN de 2,5 µm d'épaisseur et de BN enrichi en ^{10}B sur du saphir est présentée et les propriétés structurales et morphologiques du BN discutées en détail.

Le chapitre 4 se concentre sur la fabrication des dispositifs et la caractérisation électrique des nitrures d'éléments III. Des détecteurs métal-semiconducteur-métal (MSM) basés sur des structures interdigitées Ti/Au et Ni/Au ont été fabriqués en utilisant une couche de BN de 2,5 µm d'épaisseur avec du ^{10}B naturel et enrichi. Ensuite, des dispositifs MSM et PIN ont été fabriqués à partir de BGaN/GaN SLs. Les caractéristiques I-V des SLs MSM à base de h- BN, MSM et PIN à base de BGaN/GaN dans l'obscurité et sous éclairage UV sont présentées. Les mécanismes de transport des porteurs en excès, de photocourant et de gain interne du photodétecteurs sont discutés.

Le chapitre 5 présente les résultats de la détection des neutrons et les discussions sur la détection des neutrons thermiques à l'aide de détecteurs h- BN naturels et enrichis-en ^{10}B avec une structure métal-semiconducteur-métal (MSM). Les caractéristiques I-V et les mesures I-t sous flux neutronique sont présentées. Ce chapitre décrit également la réponse aux neutrons des dispositifs MSM et PIN BGaN/GaN SLs.

Le chapitre 6 présente d'abord les études sur l'incorporation de Mg dans le h- BN et les hétérostructures de h-BN dopé au Mg sur un modèle AlGaN dopé au Si pour le développement futur de détecteurs de neutrons efficaces. La dernière partie de ce chapitre porte sur l'étude d'un nouveau matériau, BAlN riche en bore.

Le chapitre 7 est divisé en trois parties. Premièrement, la partie conclusion résume les résultats de cette thèse. Deuxièmement, la partie perspective souligne les autres axes de recherche possibles pour les détecteurs de neutrons basés sur III -N. La troisième section liste les articles publiés pendant la période de la thèse.

RESULTATS

Dans cette partie, nous allons présenter les résultats de la croissance du BN et les tests de détection de neutron réalisés.

SYNTHESE ET CARACTERISATION DE h-BN:

Dans cette thèse, nous avons synthétisé des couches de BN d'une épaisseur de 2,5 µm sur des substrats de saphir par MOVPE dans un réacteur Aixtron 3×2″. Le triéthylboron (TEB) et l'ammoniac (NH3) ont été utilisés comme précurseurs du bore et de l'azote. La croissance a été réalisé à 1280 °C sous atmosphère hydrogène à une pression de 90 mbar. Le débit du TEB était de 60 µmol/min. Pour déposer des couches épaisses de BN, nous avons utilisé un taux de croissance de 450 nm/h. Les caractérisations structurales des couches de BN ont été faites par diffraction des rayons X à haute résolution (HR-XRD) et sont présentées sur la Figure 1a, sur laquelle le pic situé à 25,8° est lié aux plans (0002) du BN. La morphologie de surface des couches de BN est présentée sur la Figure 1b. L'image MEB révèle une morphologie granuleuse.

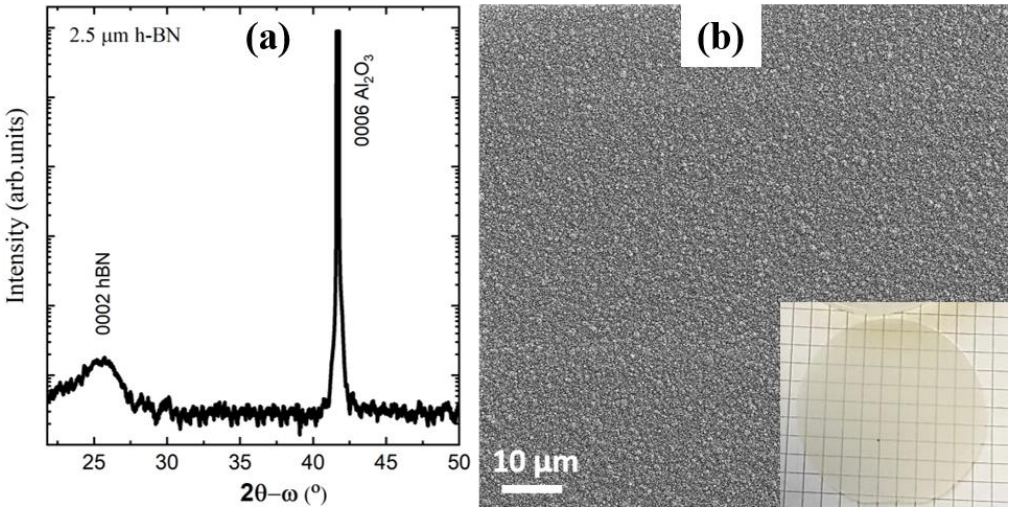

Figure 1 : (a) Diffraction des rayons X à haute résolution (HR-XRD), balayage 2θ-ω et (b) image MEB d'une couche de BN de 2,5 µm d'épaisseur.

Pour étudier les propriétés cristallographiques du h-BN, des images par microscopie électronique à transmission à haute résolution (HRTEM) en coupe transversale ont été réalisées et sont présentées à la Figure 2. Des couches de BN bidimensionnelles d'une épaisseur de 5~6 nm se sont formées à l'interface film/substrat. Dans les 10~15 nm suivants, des défauts d'empilement ont provoqué un désordre des plans cristallographiques, ce qui a entravé la croissance en couches uniformes orientées c. La Figure 2c confirme la formation d'une structure hexagonale. L'analyse des couches suivantes (partie supérieure) révèle la formation de phase turbostratique, où les feuilles en couches de h-BN sont confinées dans de courts domaines et orientées de manière irrégulière, perdant l'ordre à longue portée.

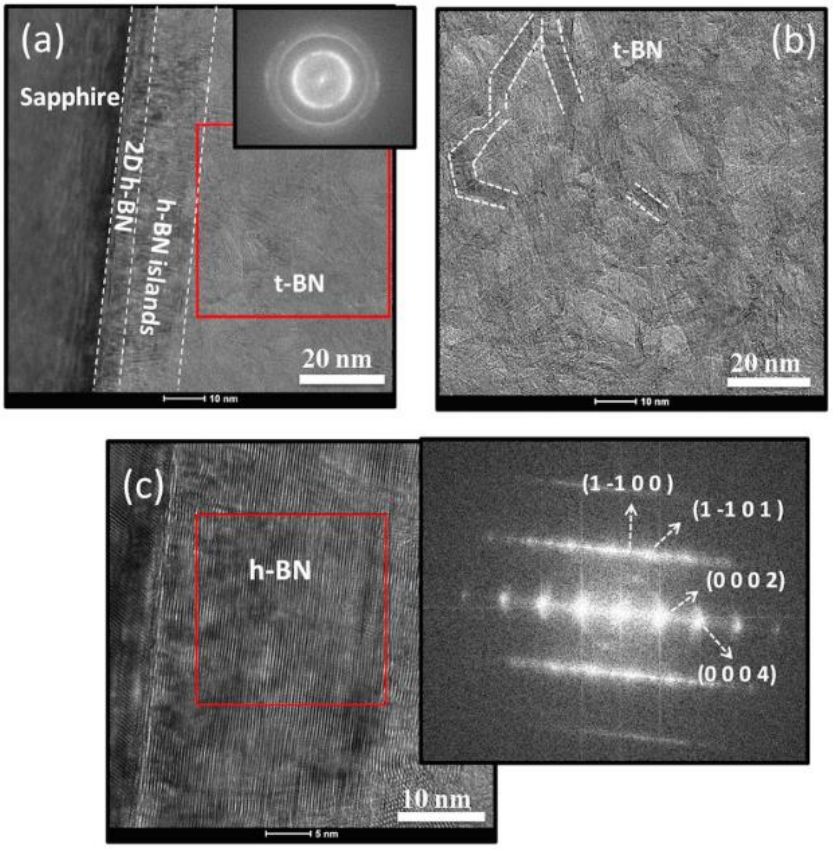

Figure 2 : (a) Image TEM du BN. L'inséré représente le motif de transformée de Fourier (FT) pour la zone sélectionnée. (b) Grossissement plus important de la partie t-BN montrant des nanofibres de BN orientées de manière aléatoire. (c) La couche 2D près de la surface du substrat confirmant la phase hexagonale [1].

Dans les mêmes conditions de croissance, nous avons synthétisé des couches de BN enrichies en ^{10}B en utilisant du TEB enrichi à 97 % en isotope ^{10}B. Cette concentration est confirmée par l'analyse SIMS. Nous avons constaté que le BN déposé avec le précurseur TEB enrichi en ^{10}B n'a aucun impact sur le taux de croissance et la qualité du matériau. Des résultats similaires ont été obtenus avec les deux précurseurs. L'épaisseur de la couche de 2,5 µm a été choisie sur la base de nos travaux précédents où des photodétecteurs UV avec la même épaisseur de BN en bore naturel

ont été rapportés [1]. L'idée est de se référer aux caractérisations s structurale et optique obtenues précédemment. Un ensemble d'échantillons de films BN naturels et enrichis-en ^{10}B de 2,5 µm ont ensuite été utilisés pour la fabrication de détecteurs MSM et ont été testés sous flux de neutrons thermiques.

DÉTECTION NEUTRONIQUE A BASE DES BN

Dans cette partie, nous présentons les résultats des tests neutroniques réalisés avec les détecteurs à base de BN. Nous avons étudié la sensibilité aux neutrons en utilisant deux contacts métalliques différents (Ti/Au et Ni/Au) et avons choisi la configuration appropriée pour la comparaison entre les MSM basés sur des détecteurs BN naturels et enrichis-en ^{10}B.

1. Source de neutrons et prototype de détection des neutrons

L'irradiation neutronique des dispositifs a été réalisée au Centre d'Etudes Nucléaires de Bordeaux-Gradignan (CENBG). La source de neutrons utilisée pour cette étude consiste en une cible LiF/Cu irradiée par un faisceau de protons produisant des neutrons d'une énergie de 500 keV. Les neutrons thermiques ont été obtenus à l'aide d'une plaque de polyéthylène haute densité (PEHD) de 5 cm d'épaisseur insérée entre le détecteur et la cible. Le flux maximal de neutrons thermiques résultant était de 3×10^4 n/cm^2/s avec une énergie neutronique inférieure à 1 eV. Les valeurs courant-tension (I-V) des différents dispositifs ont été enregistrées à température ambiante avant, pendant et après l'irradiation neutronique à l'aide d'une unité source-mesure Keithley 2636B.

2. Test neutronique avec MSM h-BN

2.1 Sensibilité (ΔI) des dispositifs MSM à base de h-BN naturel

La figure 3a montre la sensibilité (ΔI) des deux dispositifs MSM (Ni/ Au/BN/Ni /Au) et (Ti/ Au/BN/Ti /Au) pour une tension appliquée allant de 0 V à 200 V. Les deux types de détecteurs ont

ensuite été soumis à un flux de neutrons de 3×10^4 n/cm^2/s. Une augmentation du courant ΔI a été observée.

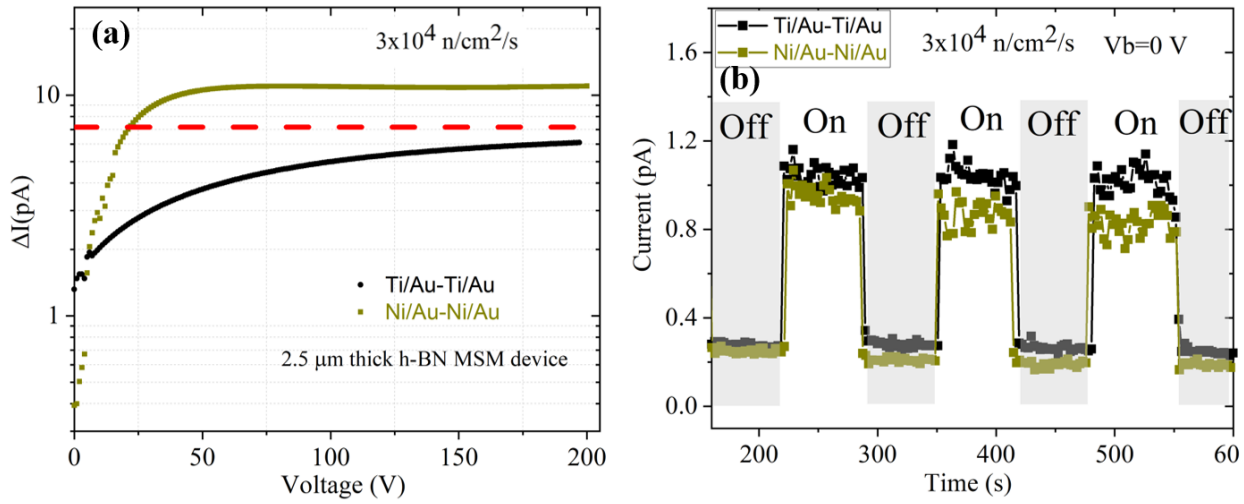

Figure 3 : (a) Courant induit par les neutrons du MSM h-BN naturel avec des contacts Ti/Au-Ti/Au et Ni/Au-Ni/Au lorsqu'il est soumis à un flux de neutrons de 3×10^4n/cm^2/s. (b) Enregistrement correspondant de la variation du courant à zéro polarisation pour les deux dispositifs.

Les deux dispositifs MSM présentant une hauteur de la barrière Schottky (SBH) asymétrique, un courant ΔI non nul est observé lorsque les dispositifs ne sont pas polarisés. Pour confirmer et affiner la valeur du courant ΔI sans polarisation, nous avons enregistré la variation du courant à zéro polarisation pour les deux dispositifs soumis à un flux périodique de neutrons de 3×10^4 n/cm^2/s, comme le montre la figure 3b. Une nette variation de courant est obtenue avec un ΔI de 0,7 pA et une sensibilité de 233%, ce qui est similaire pour les deux détecteurs.

Lorsque la tension appliquée augmente, les deux ΔI augmentent, pour atteindre la saturation à des tensions supérieures à 50 V. À une tension de polarisation de 200 V (figure 3a), ΔI du détecteur MSM avec contact Ni est environ deux fois supérieur à celui du détecteur MSM avec contact Ti. Au-delà de 25 V, ΔI des détecteurs MSM avec Ni est supérieur à la valeur théorique (gain >1). Pour les détecteurs MSM avec Ti, ΔI est très proche de cette valeur à 200 V (gain <1). Ceci pourrait s'expliquer par un mécanisme de gain dû au piégeage des porteurs de charge générés par les neutrons aux interfaces métal-semi-conducteur [2-3], ce qui diminue le SBH et permet la circulation d'un courant plus élevé. Cette augmentation du flux de courant peut être exprimée comme suit :

$$\Delta I^G = I_d \exp\left(\frac{\Delta\phi}{kT}\right) - 1 \quad (1)$$

Où I_d est le courant d'obscurité, $\Delta\phi$ est la diminution Schottky due au piégeage des porteurs générés, k est la constante de Boltzmann et T est la température absolue.

Selon l'équation 1, plus le courant d'obscurité (I_d), plus le gain interne est élevé. Si nous supposons un $\Delta\phi$ similaire pour les deux détecteurs MSM, alors le dispositif avec le plus grand courant d'obscurité devrait avoir le plus grand ΔI, ce qui est le cas. Cependant, un gain élevé s'accompagne d'un Id important, ce qui diminue la sensibilité (ΔI/Id) du détecteur. Dans notre cas, le détecteur MSM avec contact Ni présente un courant d'obscurité et donc un ΔI plus important et une sensibilité plus faible que le détecteur MSM avec contact Ti. Pour la suite de l'étude, nous avons alors considéré uniquement le détecteur MSM à haute sensibilité avec contact Ti.

2.2 Comparaison entre les MSM à base de BN naturel et enrichi en ^{10}B avec des contacts Ti/Au

Pour cette comparaison, nous avons utilisé deux dispositifs MSM avec des contacts métalliques Ti/Au pour les films BN naturels et enrichis-en ^{10}B. Les figures 4a et b montrent la variation du courant induit par les neutrons à tension nulle en fonction du temps pour les dispositifs exposés à $1{,}5\times10^4$ n/cm^2/s (flux 1) et 3×10^4 n/cm^2/s (flux 2). Nous avons observé un courant induit pour les deux dispositifs MSM BN naturels et enrichis-en ^{10}B à une tension de polarisation nulle. La valeur du courant induit par les neutrons est plus élevée dans le dispositif MSM enrichi en ^{10}B quel que soit le flux de neutrons thermiques.

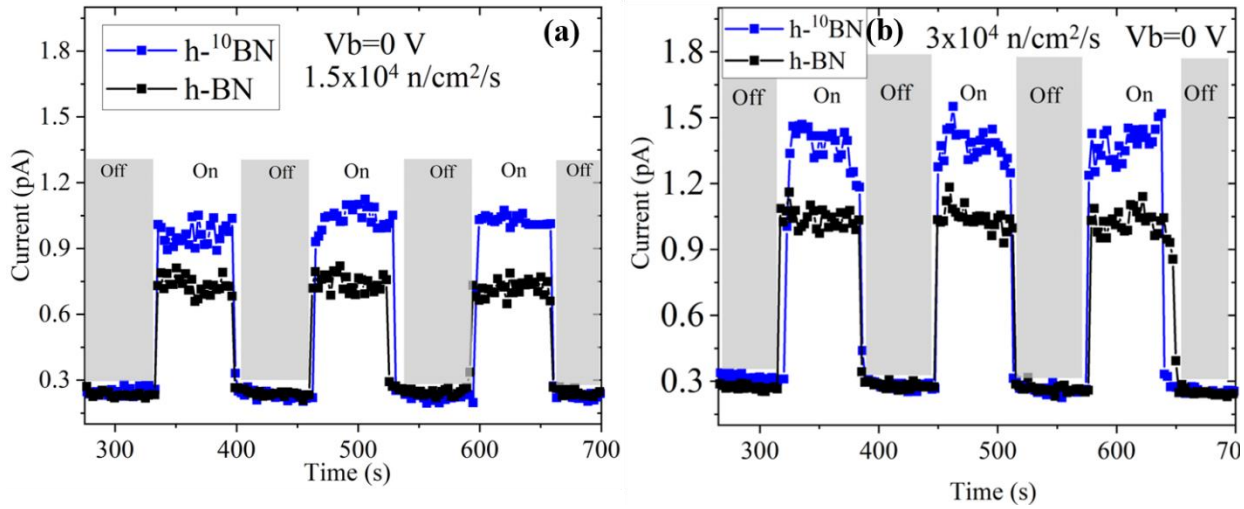

Figure 4 : réponse neutronique en temps réel du MSM h-BN naturel et du MSM h-BN enrichi en ^{10}B avec des contacts Ti/Au-Ti/Au à zéro volt avec le flux 1 (a) et le flux 2 (b).

Les sensibilités des détecteurs BN naturel et enrichi en ^{10}B à 0V sont respectivement de 233% et 367%. Ces sensibilités ne peuvent pas être comparées directement avec la littérature car il n'y a pas de valeur pour le BN à zéro volt et les sensibilités rapportées dans ce matériau ont été obtenues avec différentes épaisseurs à la tension appliquée (champs électriques différents). Par exemple, Li et al [4] ont signalé une variation de courant de 0,087 pA pour un détecteur de neutrons à BN de 1

µm d'épaisseur fonctionnant sous un champ électrique de plus de 4×10^4V/cm, ce qui correspond à une sensibilité de 170 %. Le courant induit par les neutrons du MSM de BN enrichi en ^{10}B est environ 1,4 fois plus élevé que celui du MSM de BN naturel à 0 volt (figure 4). Cette différence est due à l'augmentation du nombre d'atomes de ^{10}B dans le matériau BN enrichi, ce qui entraîne une section efficace de capture globale des neutrons thermiques plus élevée. Par conséquent, plus de neutrons sont absorbés, ce qui entraîne une augmentation de la densité de charges libres (électrons/trous) dans le matériau. Cela se traduit par un courant induit plus élever dans le dispositif MSM BN enrichi en ^{10}B.

Les mêmes détecteurs ont également été testés sous des tensions de polarisation de 100 et 200 V. Les résultats obtenus sont présentés dans la Figure 5, où le courant d'obscurité des deux dispositifs est presque le même. Cela signifie que l'effet du mécanisme de gain sous irradiation neutronique est le même. On peut observer que la réponse du détecteur MSM BN ^{10}B enrichi est systématiquement plus élevée que celle du BN naturel pour toutes les tensions appliquées et à différents flux de neutrons thermiques.

En comparant l'effet ^{10}B, nous constatons d'après la figure 5 que le rapport du courant induit par les neutrons dans les films ^{10}B et ^{11}B est compris entre 3,2 et 4,5, ce qui est très proche de la valeur théorique attendue de 5 [4]. Nous avons calculé la sensibilité des dispositifs aux neutrons à partir de la figure 5 pour le flux 2 et sous une polarisation de 200 V. Elle est de 316 % et 1192 % pour les détecteurs h-BN naturels et enrichis-en ^{10}B, respectivement. Comme le mécanisme de gain est présent dans les deux dispositifs, nous pouvons conclure que cette différence est due à l’enrichissement du BN en ^{10}B. Sur la figure 5, nous pouvons constater que le courant induit par le flux 2 est entre 1,78 et 2,38 ± 0,5 fois celui induit par le flux 1, montrant une bonne linéarité des détecteurs.

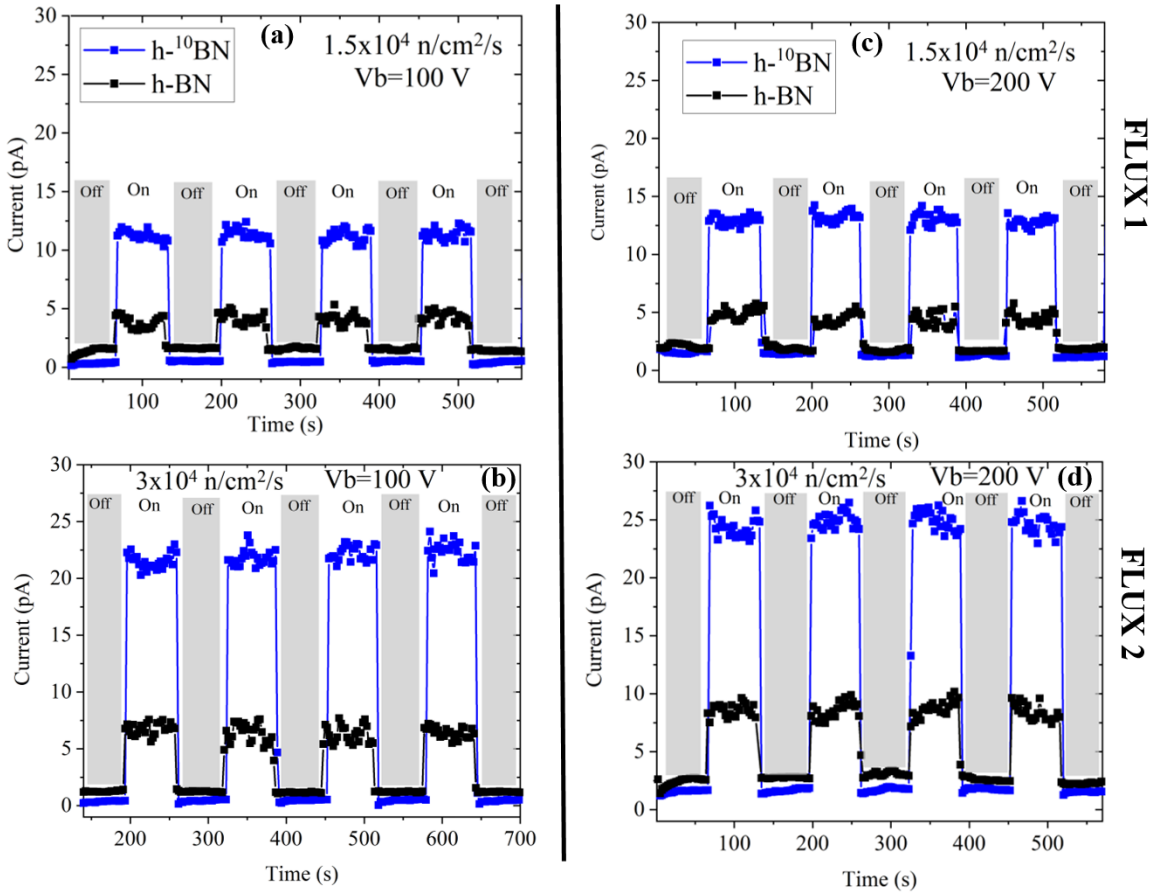

Figure 5 : Réponse neutronique en temps réel du MSM en h-BN naturel et en h-BN enrichi en ^{10}B avec des contacts Ti/Au-Ti/Au à 100 et 200 V. (a), (c) sous le flux 1 et (b), (d) sous le flux 2.

En résumé, nous avons synthétisé et caractérisé des matériaux III-N contenant du bore. Ceux-ci ont servi à développer avec succès des composants intégrés sensibles aux neutrons thermiques.

Le détecteur à base de BN (naturel et enrichi en ^{10}B) a montré un courant induit par les neutrons mesurables à zéro tension de polarisation. Ces détecteurs MSM de BN ont une sensibilité aux neutrons thermiques très élevée. En outre, le courant induit par les neutrons du détecteur MSM

h-BN enrichi en ^{10}B est jusqu'à quatre fois plus important que celui du bore naturel, mettant en évidence l'effet du boron 10.

REFERENCES

1. X. Li, M.B. Jordan, T. Ayari, S. Sundaram, Y. El Gmili, S. Alam, M. Alam, G. Patriarche, P.L. Voss, J. Paul Salvestrini, and A. Ougazzaden, Sci. Rep. 7, 1 (2017).
2. L. Sang, M. Liao, Y. Koide, and M. Sumiya, Appl. Phys. Lett. 99, 031115 (2011).
3. S. K. Zhang, W. B. Wang, I. Shtau, F. Yun, L. He, H. Morkoc, X. Zhou, M. Tamargo, and R. R. Alfano, Appl. Phys. Lett. 81, 4862 (2002).
4. J. Li, R. Dahal, S. Majety, J.Y. Lin, and H.X. Jiang, Nucl. Instruments Methods Phys. Res. Sect. A Accel. Spectrometers, Detect. Assoc. Equip. 654, 417 (2011).